UNIVERSITY OF CALIFORNIA
SANTA CRUZ

THE TIDAL EVOLUTION OF THE MOON, CALLISTO, AND TITAN

A dissertation submitted in partial satisfaction of the
requirements for the degree of

DOCTOR OF PHILOSOPHY

in

EARTH SCIENCE

by

Brynna G. Downey

June 2024

The Dissertation of Brynna G. Downey
is approved:

Professor Francis Nimmo, Chair

Professor Ian Garrick-Bethell

Professor Ruth Murray-Clay

Doctor Bruce Bills

Peter Biehl
Vice Provost and Dean of Graduate Studies

Table of Contents

List of Figures

List of Tables

Abstract

The Tidal Evolution of the Moon, Callisto, and Titan

by

Brynna G. Downey

My dissertation research uses tides to link a satellite's orbit and interior to discover what happened in its past. I have developed numerical models that include tides on the planet and satellite to see how the satellite's orbital distance, eccentricity, inclination, and obliquity vary with time. My first chapter seeks to explain how the orbit of Callisto, the fourth major moon of Jupiter, became inclined. We propose that if Callisto had passed through resonances with its inner neighbor, Ganymede, in its past, then Callisto's orbit could have received a kick that we still observe today. The second chapter focuses on the long-standing problem of how the Moon's orbit became inclined. We tested several proposed mechanisms, and the most likely scenario is that the Sun's gravitational perturbations destabilized the Moon's orbit causing it to become tilted. The third chapter takes observations of Titan's spin state and calculates the amount of tidal heating taking place in its interior at the present-day. Given how dissipative Titan is, we found that its interior needs to have a layer of low viscosity, deformable ice. Furthermore, we calculated that Titan's orbit is changing rapidly, suggesting a recent event made Titan's orbit eccentric and inclined.

To all my teachers, past, present, and future.

Acknowledgments

I'd like to thank first and foremost my advisor Francis Nimmo for guiding me through my PhD in the theme of orbital-geophysical interactions. Francis patiently let me dig myself deeper and deeper into various rabbit holes until either he gently suggested I rejoin the surface or I miraculously found something worthwhile. We had many conversations about what was weird about satellites, enough open questions to complete a PhD several times over. With great zeal Francis would do back-of-the-envelope math showing that the universe can be understood with less algebra than one might fear. Lastly, once in a time of crisis, he said that research isn't the result of something new but rather old parts glued together in new ways. This was enough to see that you don't need genius or divine intervention to have an impact and that anyone can play a part in understanding the universe that we live in.

I'd like to thank Isamu Matsuyama for being a collaborator on the Callisto inclination project and for proposing the second chapter on the Moon's inclination. The majority of our collaborations happened during the pandemic, so Zoom meetings with Francis and Isamu sustained my motivation.

My thesis committee, Bruce Bills, Ian Garrick-Bethell, and Ruth Murray-Clay provided thoughtful discussions over the years on outstanding problems in the field. During my qualifying exam in my third year, questions on how a satellite enters a Cassini state led to a final project on the same topic in my Computational Physics class, Phys 115/242 taught by Steve Ritz. This foundation in spin state dynamics

paved the way for the equations derived in my third chapter on Titan's spin state.

Planetary group meetings allowed me to interact with Myriam Telus, Xi Zhang, Misha Kreslavsky, and Don Korycansky whose planetary knowledge broadened what I was familiar with and who provided feedback on conference posters and presentations.

Other planetary scientists in the field have been influential in my success in graduate school. Jack Wisdom led a collaboration on Saturn's obliquity that I was very fortunate to have been a part of. Matija Ćuk has been encouraging of my research and participation in the dynamics community and conferences.

Over six years in graduate school, I have gotten to know and lean on many planetary grads and postdocs: Carver Bierson, Nick Zube, Jack Conrad, Szilard Gyalay, Coby Abrahams, Huazhi Ge, Wencheng Shao, Linfeng Wan, Rachel Maxwell, Megan Seritan, Secana Goudy, Nathan MacGregor, Pranvera Hyseni, Jill Kirk, Kara Jaramillo, Ryu Akiba, ZhenLiang Tian, Xinting Yu, Jasmeet Dhaliwal, Laurent Pou, Emilie Dunham, and Ben Idini. Together, we have gone on Perk runs, taken walks around campus, attended speaker lunches, proofread each other's emails and proposals, and been good friends to explore conferences with.

In my first month at UCSC, I got an email about the Graduate Student Association's (GSA) first meeting of the year with free dinner for attendees, so of course I went. There is no such thing as a free dinner, so by the end of the meeting, I was the EPS representative to the GSA. By the end of the next meeting the following month I was the graduate student representative on the faculty Committee on Information Technology (CIT). By winter, I was the GSA's liaison to GradLab, and by spring I had

become treasurer of the Graduate Student Commons (GSC). By my second year, I was on the Student Fee Advisory Committee (SFAC), and by my third year, I was the chair. SFAC was one of the highlights of my career in graduate school, allowing me to hear from every corner of campus on how different units use student fees and to stretch my brain in ways that I didn't know were possible. Lucy Rojas was SFAC's enthusiastic and insightful advisor without whom institutional knowledge would have been lost and our meetings would have had less momentum and discussion.

Lastly, I couldn't have completed my PhD without the support of my parents who have always encouraged me throughout my education and who let me test my powerpoint animations on them during the pandemic.

Previously published material

The text of this dissertation includes modified reprints of the following previously published material:

C. 2 Downey, B. G., Nimmo, F., & Matsuyama, I. (2020). Inclination damping on Callisto. Monthly Notices of the Royal Astronomical Society, 499(1), 40-51.

C. 3 Downey, B. G., Nimmo, F., & Matsuyama, I. (2023). The thermal–orbital evolution of the Earth–Moon system with a subsurface magma ocean and fossil figure. Icarus, 389, 115257.

The co-authors listed in these publications directed and supervised the research which forms the basis for the dissertation.

Chapter 1

Introduction

Our solar system is home to eight major planets that collectively host hundreds of orbiting satellites. Telescopes and spacecraft missions have observed tremendous diversity among satellites in terms of their interior structure and orbital characteristics. This diversity points to a wide range of evolutionary paths, but why paths diverge for different satellites is not well understood. Understanding satellite evolution will highlight trends in how they form, how they migrate to their current positions in the solar system, and what their interior structures are.

A major driver of a satellite's evolution is tides raised on the satellite by its central planet. Tides generate friction in the satellite's interior, which can heat the satellite, take energy out of the orbit, cause the orbit to contract, and damp the orbital eccentricity and inclination. At the same time, tides raised on the central planet by the satellite will expand the orbit, damp the inclination, and compete to increase the eccentricity. Tidal dissipation provides a timescale over which a satellite's orbit should

be become circular or planar, which helps to put an approximate age to the eccentricity and inclination.

In three chapters, I explore dynamical mysteries on Callisto, our Moon, and Titan by modelling how their orbits and rotation states change under the influence of tides. Orbits that are changing quickly point to a recent event that affected their eccentricity and inclination, and those are changing slowly can be primordial relics of the satellite's formation. In this way, the present-day dynamical state of a satellite is a window into what happened in its past.

Chapter 1 – Inclination damping on Callisto. Callisto, the fourth icy satellite of Jupiter, shows evidence for a subsurface ocean beneath a thick ice shell. Recent research suggests that obliquity tides are stronger in oceans of satellites than in solid layers. Obliquity tides on a satellite damp its orbital inclination, so ocean obliquity tides should have damped out Callisto's inclination completely. Callisto's inclination is non-zero, so to uncover what excited its orbit in the past, I tested scenarios against a tidal-orbital model that I developed. By varying Callisto's physical properties, we were able to vary the amount of tidal dissipation in Callisto, which damped its orbital eccentricity and inclination. We also varied the strength of tides in Jupiter, which controls Callisto's semi-major axis migration rate.

We found that if tides on Jupiter caused Callisto's semi-major axis to increase rapidly over time, then Callisto could have passed through resonances with its inner neighbor, Ganymede, exciting its inclination in the process (Downey et al. 2020). Our results were some of the first to consider the downstream effects of a new paradigm for

enhanced dissipation on giant planets, called resonance-locking; rapid outwards migration of satellites would lead to more resonance crossings and excited orbits.

Chapter 2 – The thermal-orbital evolution of the Moon. The Moon is one of the best studied satellites in the solar system, and yet how it acquired its orbital inclination is still unknown. The Moon is believed to have formed from a giant impact between a Mars-sized impactor and the proto-Earth. It accreted from the debris disk in Earth's equator, which was a zero-inclination orbit. Furthermore, tides on the Moon and Earth damp the inclination and never excite it, so a dynamical mechanism is needed to explain the lunar orbital tilt. We revisited theories about when and where the Moon got its inclination with an updated thermal-orbital model that coupled cooling of the magma ocean with its orbital migration. What was new was that the cooling magma ocean affected the size of the Moon's rotational and tidal bulges, which in turn affected its obliquity and tidal heating. We know the size of the Moon's rotational and tidal bulges today, so this feedback was a new, additional way to constrain our models.

We found that the most likely theory was that as the Moon migrated away from the Earth, the Sun's gravitational perturbations gradually outweighed the Earth's until a transition point destabilized the lunar orbit, causing it to become inclined (Downey et al. 2023). This scenario required the Moon to migrate slowly, meaning low tidal dissipation in the early Earth. which past work has shown could be due to an early thick atmosphere that prevented the Earth from cooling. There are no records of the Earth soon after its formation, so placing constraints on its conditions from the Moon's evolution fills in a major gap in our knowledge, which has implications for our understanding of the onset

of plate tectonics, Earth's global oceans, and life.

Chapter 3 – Titan's spin state as a constraint on internal dissipation. The Moon and Titan are the only two satellites in the solar system with observed spin axes and both are marginally offset from their expected orientations. Previous analyses of the Moon have shown that its angular offset is because of tidal dissipation and friction between the solid mantle and fluid core. While past works have studied Titan's obliquity, no one had ever studied its offset. To fill this gap, I developed an analytical relation between the offset and the amount of energy dissipation from both tides and core-mantle boundary friction.

The results in our submitted work suggest that Titan's offset is likely completely due to tides, making this work the first to place a constraint on how dissipative Titan is. To dissipate the expected amount of tidal heating, we found that its interior needs to have a layer of low viscosity, deformable ice underneath the ocean. The broader implications are that tides can be used to predict Titan's past and future orbital evolution. To this end, we calculated that tidal heating is changing Titan's orbit rapidly, suggesting that a recent event made Titan's orbit eccentric and inclined. This is important for the scientific community because it corroborates other research that suggests that Saturn's moons have recently been perturbed, shuffled, or in some instances, even lost.

Chapter 2

Inclination damping on Callisto

This chapter is a slightly modified reprint of work previously published as Downey, B. G., Nimmo, F., & Matsuyama, I. (2020). Inclination damping on Callisto. Monthly Notices of the Royal Astronomical Society, 499(1), 40-51.

Abstract

Callisto is thought to possess a subsurface ocean, which will dissipate energy due to obliquity tides. This dissipation should have damped any primordial inclination within 1 Gyr - and yet Callisto retains a present-day inclination. We argue that Callisto's inclination and eccentricity were both excited in the relatively recent past ($\sim$ 0.3 Gyr). This excitation occurred as Callisto migrated outwards according to the "resonance-locking" model and passed through a 2:1 mean-motion resonance with Ganymede. Ganymede's orbital elements were likewise excited by the same event. To explain the present-day orbital elements we deduce a solid-body tidal $k_2/Q \approx 0.05$ for

Callisto and a significantly lower value for Ganymede.

2.1 Introduction

The thermal and orbital evolution of satellites is governed by energy dissipated by tides in both the planet and the satellite (e.g., Goldreich and Soter, 1966).

Tides raised on the planet by the satellite generally lower the planet's spin rate and transfer angular momentum to the satellite, increasing its semi-major axis (the orbital distance). The exceptions to this rule are retrograde satellites, such as Triton, and satellites inside the synchronous rotation point, such as Phobos. In these cases, the satellite spirals in towards the planet. Tides raised on the planet will also raise the satellite's eccentricity (how far the elliptical orbit is from being circular) and lower its inclination (the angle between the orbital plane and the Laplace plane). The Laplace plane is the mean orbital plane, so the orbit normal precesses around the Laplace plane normal.

Tides raised on a synchronously-rotating satellite by the planet will lower either the inclination or the eccentricity depending on whether obliquity (the angle between the orbit normal and the spin pole) or eccentricity is at the root of the synchronous rotation anomaly. A satellite's obliquity and inclination are related via Cassini states (Ward, 1975a), so obliquity tides lower inclination, which lowers obliquity (e.g., Chyba et al., 1989).

The amount that the inclination and eccentricity decrease by depends on how

easily the satellite deforms due to the planet's gravitational pull and how much friction its interior experiences in trying to realign the tidal bulge to the line connecting the centres of mass. Rates of change for inclination and eccentricity and their corresponding tidal heating are most frequently computed under the assumption that satellites are completely solid, viscoelastic bodies (Ross and Schubert, 1986).

There is growing evidence, however, that many satellites in our solar system are not purely solid bodies and may have subsurface oceans (Nimmo and Pappalardo, 2016). For example, detections of an induced magnetic field by the Galileo magnetometer during Callisto flybys (Zimmer et al., 2000) and the measurement of Titan's obliquity (Bills and Nimmo, 2011; Baland et al., 2011) strongly suggest that Callisto and Titan have subsurface oceans. Although Hartkorn and Saur (2017) propose that the magnetic field signal detected at Callisto could be accounted for by induction in its ionosphere, in this work we will assume that Callisto has a subsurface ocean (Zimmer et al., 2000). Satellites without the advantage of extensive flybys, such as Oberon and other outer satellites might still have subsurface oceans according to models that emphasize the role of salts in reducing the melting temperature of ice (Hussmann et al., 2006).

As discussed in more detail below, dissipation in subsurface oceans can be substantial and, crucially, tends to damp orbital inclination as or even more rapidly than the solid body does. Thus, for a body like Callisto with a subsurface ocean, the survival of a non-zero present-day inclination presents a puzzle. The bulk of this manuscript investigates how such a non-zero inclination could be maintained.

In the remainder of this section we lay out the basics of inclination and eccen-

tricity damping. In Section 2.2, we show that Callisto's inclination damping time-scale is expected to be short compared to the age of the solar system for likely parameter values. In Section 2.3, we show that in a frequency-dependent Q of Jupiter scenario, one or more mean-motion resonance crossings could increase Callisto's inclination to current levels. In Section 2.4, we show that Callisto's eccentricity and Ganymede's orbital elements can also be explained by these resonance crossings. We conclude by suggesting further work and making predictions that can be tested with future spacecraft missions.

2.1.1 Ocean tidal dissipation and inclination damping

With an increased number of suspected subsurface oceans in our solar system comes the question of how energy is dissipated in the non-solid body. Here we review a few important contributions to this subject. Sagan and Dermott (1982) and Sohl et al. (1995) calculated the dissipation of eccentricity tides in Titan's presumed methane surface ocean to determine the lifetime of its eccentricity. Tyler (2008, 2009, 2011) emphasized the importance of obliquity tides and made the first numerical models of tidal heating in a surface ocean. Chen et al. (2014) expanded on this by numerically deriving formulas for eccentricity and obliquity tide dissipation due to bottom drag in a surface ocean.

Leading up to the model that we use in this work, Matsuyama (2014) considered the effects of self-gravity and deformation of the solid regions assuming linear drag, and Hay and Matsuyama (2017) developed a numerical model that takes these effects into account for both linear and bottom drag. Beuthe (2016) provided the first

rigorous quantification of the effect of an overlying ice shell by treating the ice shell as a massless membrane. Matsuyama et al. (2018) expanded on this by providing a theoretical treatment that is applicable to elastic shells of arbitrary thickness, and Hay and Matsuyama (2019) used this theory to consider dissipation in a subsurface ocean due to bottom drag with a numerical model.

These numerical models for calculating the tidal dissipation rate in an ocean should be compared with the standard rate of tidal dissipation in a solid synchronous satellite, given by

$$\dot{E}_{\text{solid}} = \frac{3}{2}\frac{k_2}{Q}\frac{\Omega^5 R^5}{G}(\sin^2\theta_0 + 7e^2), \tag{2.1}$$

(Peale and Cassen, 1978; Peale et al., 1979; Wisdom, 2004) where k_2/Q is a measure of how deformable the satellite is, Ω is the spin frequency, R is the radius, G is the gravitational constant, θ_0 is the satellite's obliquity, and e is its eccentricity.

A consequence of the factor of 7 in Eq. 2.1 is that solid-body dissipation damps eccentricity more rapidly than obliquity assuming that both are small and comparable in value. The simple relationship between inclination and eccentricity decay rates to their respective tidal dissipation rates can be found in Chyba et al. (1989). Conversely, ocean obliquity tides are in general much more dissipative than eccentricity tides (e.g., Tyler, 2011), so the inclination damps more rapidly than eccentricity.

The key finding is that ocean obliquity tides contribute substantially to satellite inclination damping. Just as Sagan and Dermott (1982) and Sohl et al. (1995) investigated whether tidal dissipation allowed Titan's eccentricity to have lasted the lifetime of the solar system, we seek to calculate approximately how long it would take

obliquity tides in a satellite subsurface ocean to damp inclination.To do this, we define an inclination damping time-scale, τ_i, which is a first order, small-inclination approximation of how long it would take obliquity tide dissipation in a satellite's ocean, $\dot{E}_{\rm obl}$, to damp its present-day inclination, i (Sagan and Dermott, 1982; Chyba et al., 1989; Sohl et al., 1995):

$$\tau_i \sim \frac{GMm}{a\dot{E}_{\rm obl}} i^2, \tag{2.2}$$

where M is the mass of the planet, m is the mass of the satellite, and a is the satellite's orbital semi-major axis. In Section 2.2 below we provide analytical methods for calculating $\dot{E}_{\rm obl}$ for subsurface oceans.

Fig. 2.1 plots the inclination damping time-scales for all icy satellites in our solar system using the ocean dissipation estimates tabulated in Chen et al. (2014). The approximate correlation between damping time-scale and orbital distance appears to be a consequence of the fact that the predicted obliquity relative to the inclination, and thus the dissipation rate, is itself a strong function of distance. Assuming long-lived oceans, Callisto, Oberon, and Titan all have inclination lifetimes of $\tau_i < 1$ Gyr. Any primordial inclination on Callisto, Oberon, and Titan would have been damped out quickly, whereas most other satellites' inclinations could be primordial and have lasted until today. There is no evidence indicating whether Oberon has a subsurface ocean or not, and like the other Uranian satellites, it could have had chaotic orbital evolution (Dermott et al., 1988). Titan may have had a very interesting dynamical history, migrating greatly in semi-major axis (Lainey et al., 2020) and potentially being influenced by the Jupiter-Saturn Great Inequality (Bills and Nimmo, 2005). In this

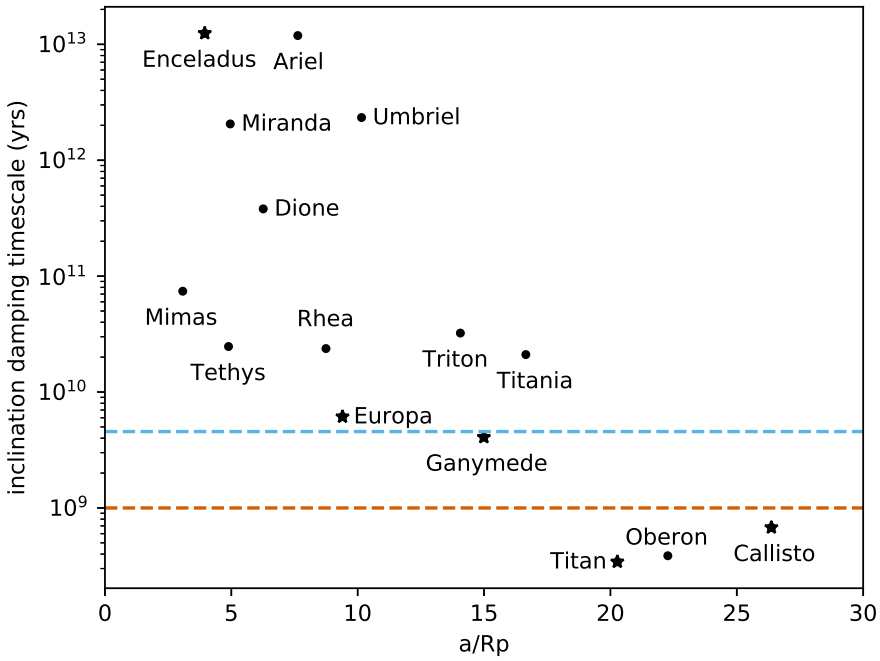

Figure 2.1: Inclination damping time-scales from ocean obliquity tide dissipation rates in Chen et al. (2014). Those icy satellites with evidence of subsurface oceans are denoted with a star (Nimmo and Pappalardo, 2016). The blue and orange dashed lines are the 4.56 Gyr and 1 Gyr marks, showing that Callisto and Titan are aberrant in having large energy dissipation yet long-lasting inclinations.

work we focus on Callisto because it presents a somewhat simpler dynamical problem than Titan.

From the above order-of-magnitude calculation, we conclude that Callisto has a non-zero inclination when it should have been damped away by obliquity tides. Either Callisto's physical properties are not well-understood or a dynamical event in the last 1 Gyr increased its inclination. In the remainder of this manuscript we explore both of these possibilities.

Table 2.1: Parameters used in Callisto's obliquity tide ocean inclination damping

Symbol	Parameter	Value
G	Gravitational constant	6.674×10^{-11} m^3 s^{-2} kg^{-1}
M	Mass of Jupiter	1.898×10^{27} kg
m	Mass of Callisto	1075.9×10^{20} kg
R	Radius	2410.3 km
Ω	Spin frequency	4.36×10^{-6} s^{-1}
θ_0	Predicted obliquity	-0.24°
g	Gravitational acceleration	1.24 m s^{-2}
a	Semi-major axis	1882.7×10^{6} m
e	Eccentricity	0.0074
i	Inclination	0.192°
ρ_b	Bulk density	1830 kg m^{-3}
ρ_o	Ocean density	1000 kg m^{-3}
ρ_i	Ice density	900 kg m^{-3}
d	Ice shell thickness	150 km
h	Ocean thickness	30 km
c_D	Bottom drag coefficient	0.002
β_2	Shell pressure forcing coefficient	0.88
υ_2	Tidal potential forcing coefficient	1.05
η	Water dynamic viscosity	10^{-3} Pa s
μ	Ice shear modulus	3×10^{9} Pa

2.2 Effect of physical properties on ocean dissipation

Callisto's inclination damping time-scale could be the age of the solar system or longer if certain physical properties resulted in reduced dissipation in its putative global ocean.

From the body of work discussed in the previous section that addresses the ocean obliquity tide dissipation rate, we choose to use the analytical expressions from (Hay and Matsuyama, 2019). They include the effects of an overlying ice shell, self-

gravity, and deformation of the solid regions:

$$\dot{E}_{\rm obl} = 12\pi\rho h\nu_{\rm obl}\Omega^2 R^2\theta_0^2\upsilon_2^2\left(\frac{R}{r_t}\right)^2\left[1+\left(\frac{20\upsilon_2\beta_2\nu_{\rm obl}gh}{\Omega^3 r_t^4}\right)^2\right]^{-1}$$
$$\nu_{\rm obl} = \frac{\Omega^3 r_t^4}{20\sqrt{2}\beta_2 gh}\left\{-1+\left[1+\left(\frac{200}{3}0.4c_D\beta_2\upsilon_2\frac{gR^2\theta_0}{\Omega^2 r_t^3}\right)^2\right]^{1/2}\right\}^{1/2}. \quad (2.3)$$

Here ρ is the subsurface ocean density, h is the thickness of the ocean, ν_{obl} is turbulent viscous diffusivity, Ω is the spin frequency, R is the radius, θ_0 is the obliquity, g is the surface gravity, r_t is the ocean top radius, and c_D is the drag coefficient at the bottom of the ocean. Shell pressure forcing is captured by the coefficient β_2, and the perturbation to the forcing tidal potential due to shell pressure forcing, self-gravity, and deformation of the solid regions is captured by the υ_2 coefficient. These dimensionless coefficients can be computed in terms of pressure and tidal Love numbers (Matsuyama et al., 2018, Eq. 22). Assuming a thin surface ocean ($r_t \sim R$) and ignoring self-gravity, deformation of the solid regions, and shell pressure forcing ($\beta_2 = \upsilon_2 = 1$), Eq. 2.3 reduces to the analytical equations in Chen and Nimmo (2016) with their factor $\xi_2 = 1$, as expected. Solutions for a thin surface ocean that take into account the effects of self-gravity and deformation of the solid region can be obtained with the substitutions $r_t \to R$, $\upsilon_2 \to 1 + k_2^T - h_2^T$, and $\beta_2 \to 1 - (1 + k_2^L - h_2^L)(3\rho)/(5\bar{\rho})$,where k_2^T and h_2^T are tidal Love numbers and k_2^L and h_2^L are load Love numbers. Nominal values assumed for all these parameters are tabulated in Table 2.1.

A key feature of the model in Hay and Matsuyama (2019) is that it uses bottom drag to account for energy dissipation. This is helpful because as discussed in more detail below and in Hay and Matsuyama (2017), the bottom drag coefficient c_D

is known, at least approximately, for terrestrial oceans. This is in contrast to some alternative parameterizations of bottom friction. What we find for obliquity tides in the bottom drag scenario is that there is a trade-off between drag and energy dissipation (Fig. 2.2a). If drag is unimportant, flow velocities will be uninhibited but the effective viscosity will be low, resulting in less energy dissipated and a linear increase in dissipation with viscosity. On the other hand, if drag is important, viscosity will be large, but the flow velocities will be reduced, and the energy dissipation will decrease again (see also Chen et al., 2014, Fig. 3). Physically, whether bottom drag affects the velocity is determined by the Reynolds number $\Omega R^2/\nu_{\rm obl}$; the other important dimensionless quantity in Equation 2.3 is the Lamb parameter $4\Omega^2 R^2/gh$ which denotes the relative speeds of surface gravity waves compared to rotation (Chen et al., 2014).

The biggest uncertainties in these analytical expressions are the bottom drag coefficient c_D, the ocean thickness h, and the factors that encapsulate the effect of the rigid ice shell, β_2 and υ_2. Below, we will explore the sensitivity of Callisto's inclination damping time-scale to the uncertainties in our knowledge of these parameters.

2.2.1 Drag coefficient at the bottom of the ice shell

In Hay and Matsuyama (2019), all of the dissipation in the ocean is modelled as friction at the ocean floor. The bottom drag coefficient estimate, c_D, is 0.002, the commonly-assumed value for oceans on Earth that is often deemed applicable to other bodies as well (e.g., Jeffreys, 1925; Sagan and Dermott, 1982; Sohl et al., 1995; Hay and Matsuyama, 2017). Fig. 2.2a plots the inclination damping time-scale as a function of

c_D, showing that this value would have to be two orders of magnitude larger or smaller than on Earth for the inclination lifetime to become comparable to the age of the solar system.

To investigate the value of c_D further, we use the empirically-derived expression for bottom drag from Turcotte and Schubert (1982) that depends on the Reynolds number to see whether Callisto's c_D could be two orders of magnitude larger or smaller than on the Earth:

$$c_D = 0.3164 \left(\frac{\rho v h}{\eta} \right)^{-1/4}, \tag{2.4}$$

where ρ is the subsurface ocean density, v is the flow speed, h is the ocean thickness, and η is the molecular viscosity (Turcotte and Schubert, 1982). We adopt values consistent with liquid water, $\rho = 1000$ kg m^{-3} and $\eta = 10^{-3}$ Pa s (Sohl et al., 1995). In Chen et al. (2014), the flow speed is a function of effective viscosity, which itself depends on the bottom drag coefficient, so we can simultaneously solve for v and c_D given a specific ocean thickness.

Fig. 2.2b combines the obliquity tide ocean dissipation equations from Eq. 2.3 with the drag coefficient relation from Eq. 2.4 to plot Callisto's inclination damping time-scale as a function of ocean thickness. Flow speed varies with every calculated point and is determined by the expressions in Table 4 of Chen et al. (2014). For a nominal ocean thickness of 30 km, $c_D = 0.0018$, which is almost exactly the standard value used of $c_D = 0.002$. When $h = 10$ m, $c_D = 0.017$, and when $h = 200$ km, $c_D = 0.001$. The velocity always stays around a few cm s^{-1}, and c_D stays within an order of magnitude of the nominal value. Callisto's ocean would have to be less than

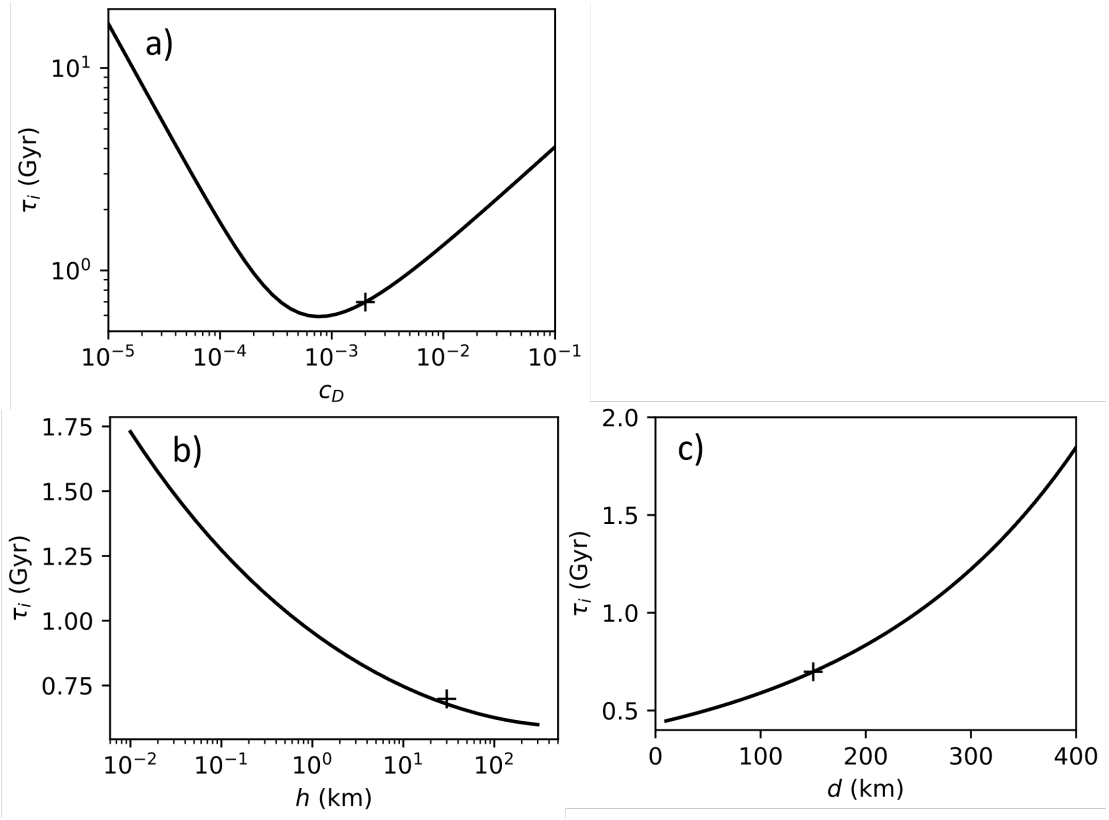

Figure 2.2: How Callisto's inclination lifetime varies with a) bottom drag coefficient b) ocean thickness c) ice shell thickness using Eq. 2.3. Values used in the rest of the paper are marked with a "+" and are $c_D = 0.002$, $h = 30$ km, and $d = 150$ km. For these values β_2=0.88 and υ_2=1.05.

10 m thick for drag to be weak enough to lengthen the inclination lifetime to 1.6 Gyr (still too short). Even then, for such a thin ocean, resonances (not captured by 2.3) can arise, increasing dissipation and decreasing the inclination lifetime.

2.2.2 Effect of a thick ice shell

The amount of energy dissipated in Callisto's putative subsurface ocean depends on how rigid and thick the overlying ice shell lid is. If the lid is sufficiently weak,

then the ocean would be free to flow and dissipate energy as if there were no lid. If the lid deforms not at all, then there would be nowhere for the ocean to flow and no energy dissipation. The ice shell thickness factors into the quantities β_2, υ_2, and r_t in Eq. 2.3, which capture shell pressure, self-gravity, and solid deformation and are related to the pressure and tidal Love numbers.

There are different estimates for Callisto's surface ice thickness, ranging from 100-300 km. Zimmer et al. (2000) conclude that the ocean starts at less than 200-300 km depth. Moore and Schubert (2003) calculate that the ocean should be centred at 166 km. McKinnon (2006) takes the overlying ice thickness to be 180 km, and finally, Kuskov and Kronrod (2005) take it to be 135-150 km. We assume that Callisto's ice thickness is 150 km, satisfying all of these estimates.

To quantify the effect of the ice shell, we compute β_2 and υ_2 as a function of ice shell thickness in the case of a 30 km thick ocean, and we use the obliquity tide ocean dissipation equations from Eq. 2.3 to plot the inclination lifetime in Fig. 2.2c. The inclination damping time-scale remains under a few billion years for ice shell thicknesses smaller than the 300 km maximum determined by Callisto flybys (Zimmer et al., 2000). In reality, the rigid shell thickness may be significantly less than the total shell thickness since the base of the shell is likely warm enough to lack rigidity at tidal frequencies. The result is that it is even less likely for the ice shell to restrict ocean dissipation enough to preserve Callisto's inclination over the lifetime of the solar system.

2.2.3 Summary

Callisto's inclination damping time-scale is much shorter than the age of the solar system for nominal parameter values. Although in principle a sufficiently rigid lid or a very low drag coefficient could mitigate this problem, in neither case do the parameter values required appear to be realistic.

2.3 Increasing Callisto's inclination

Without an internal tidal solution to Callisto's non-zero inclination, we are left to find explanations external to Callisto. To do so, we need to look at Callisto's dynamical history. Recent astrometry observations suggest that the satellites of the outer planets could be migrating away from their planets faster than previously expected (Lainey et al., 2017, 2020). Semi-major axis migration is mostly driven by tidal dissipation in the planet, which is described by the tidal quality factor, Q. Dissipation in the satellite con also change the semi-major axis but this effect is generally much smaller. Standard tidal theory assumes that Q is constant for a planet, whereas the new observations suggest a different and time-variable Q for each modal frequency of the planet's internal structure excited by a different satellite. To provide a physical explanation for this phenomenon, Fuller et al. (2016) proposed that giant planet tides are satellite dependent and their interiors evolve just as those of stars do. In the rest of this work, we examine the implications of applying this new tidal theory to tides raised on Jupiter by Callisto using a simple proof-of-concept approach. Given the large

Table 2.2: Dynamical parameters used in resonance-locking scenario.

Body	a ($\times 10^6$ m)	e	i (°)	θ_0 (°)	Ω (rad s^{-1})	p'	t_α (Gyr)	t_{tide} (Gyr)
Jupiter	7.79×10^5	-	-	-	1.76×10^{-4}	-	-	-
Io	421.8	-	-	-	4.11×10^{-5}	-	44	20
Europa	671.1	-	-	-	2.05×10^{-5}	-	101	20
Ganymede	1070.4	0.0094	0.177	-0.05	1.02×10^{-5}	-6972	217	20
Callisto	1882.7	0.0074	0.192	-0.3	4.36×10^{-6}	-11423	63	2.7

Table 2.3: Physical parameters used in resonance-locking scenario

Body	M ($\times 10^{20}$kg)	R (km)	J_2	$C_{2,2}$	c
Jupiter	1.898×10^7	71398	1.474×10^{-2}	-	-
Io	893.2	-	-	-	-
Europa	480.0	-	-	-	-
Ganymede	1481.9	2631.2	$10/3C_{2,2}$	3.83×10^{-5}	0.311
Callisto	1075.9	2410.3	$10/3C_{2,2}$	1.02×10^{-5}	0.353

uncertainties involved, we leave more detailed treatments for future work.

2.3.1 Fuller Model

A satellite orbiting a planet will raise a tidal bulge on the planet just as the planet will raise a tidal bulge on the satellite. As the planet rotates faster than the satellite orbits, the planet's bulge will be ahead of the line connecting the planet to the satellite. The satellite will have a net torque on the planet in an effort to slow down the planet's spin to realign the bulge with the direction vector to the satellite. Angular momentum gets transferred from the spin of the planet to the orbit of the satellite, and the lost spin rotational kinetic energy of the planet is dissipated in its interior.

The model proposed in Fuller et al. (2016) connects the phase lag between the planet's tidal bulge and the direction vector to the satellite, which is governed

by the difference between the planet's spin rate and the satellite's orbit rate, to the eventual dissipation in the planet. The dissipation could also be thought of as internal friction between the bulge and the rest of the planet as it tries to reposition itself. Fuller et al. (2016) presume that there are certain resonant frequencies arising from the planet's structure at which dissipation is greatly increased. If the orbital frequency of the satellite in the planet's spin rotational reference frame is the same as one of these resonant modes, then there will be enhanced dissipation and a greater transfer of angular momentum to the satellite's orbit, forcing it to migrate outwards faster. The final step in Fuller et al. (2016) is to suggest that the frequencies of these resonant modes evolve at a time-scale set by the evolution time-scale of the planet; this same time-scale then sets the rate of outwards evolution of the satellite. In this scenario, the satellite's orbital frequency is in resonance with the mode of the structure and gets locked into that resonance hence the name of the phenomenon, resonance locking.

For a mode in Jupiter's interior that evolves over a time-scale t_α, to which Callisto's orbital frequency is resonantly-locked, Callisto's orbital frequency or mean-motion, n, as a function of time from Nimmo et al. (2018) is

$$n(t) = \Omega_p + (n_{\rm now} - \Omega_p) \exp\left(\frac{t - t_{\rm now}}{t_\alpha}\right), \tag{2.5}$$

where Ω_p is the spin frequency of the planet and is assumed constant, $n_{\rm now}$ is the present-day mean-motion, and $t_{\rm now}$ is time at present. t_α could be different for each satellite orbiting a planet because each satellite would be resonantly-locked to different interior structures. Astrometry of a satellite's migration rate da/dt can tell us the hypothetical

values of t_α by the following approximate relation (Fuller et al., 2016, Eq. 12) in the limit where the planet's spin decays more slowly than its interior evolves

$$\frac{1}{t_{\rm tide}} \equiv \frac{1}{a}\frac{da}{dt} = \frac{2}{3}\frac{1}{t_\alpha}\left(\frac{\Omega_p}{n} - 1\right). \tag{2.6}$$

The quantity $t_{\rm tide}$ represents the time it would take the orbital energy stored in the orbital distance to change by a factor of itself. By definition of $t_{\rm tide}$ in Eq. 2.6, satellites in a mean-motion resonance (MMR), where the orbital periods of two or more satellites are integer multiples of each other, have the same value of $t_{\rm tide}$. Io, Europa, and Ganymede are in the Laplace resonance, i.e., the 4:2:1 three-body MMR. Fuller et al. (2016) and Lainey et al. (2009) estimate their $t_{\rm tide}$ at the present-day to be 20 Gyr with error bars of a few Gyr. There are as yet no astrometry measurements for Callisto, and it is not part of the Laplace resonoance. Fuller et al. (2016) predict for Callisto that $t_{\rm tide} \sim 2$ Gyr. Although recently, Dbouk and Wisdom (2023) calculated that for Callisto's migration to have affected a secular spin-orbit resonance that increased Jupiter's obliquity, $t_{\rm tide} \geq$ 12 Gyr. The present-day $t_{\rm tide}$ values are used to derive the satellites' long-term t_α values using Eq. 2.6.

Fig. 2.3 plots an example of what the resonance locking semi-major axis evolution would look like for the Galilean satellites over the past 1.5 Gyr where at the present-day, $\rm t_{tide}$ = 2.7 Gyr for Callisto and 20 Gyr for the inner satellites. Callisto's $\rm t_{tide}$ is an order of magnitude smaller because Callisto has the smallest mean-motion (see Eq. 2.6). There is a characteristic concave-up shape associated with semi-major axis evolution in the resonance locking scenario compared to the concave-down shape

in a constant Q one. The k_2/Q of Jupiter at Callisto's orbital frequency varies from 0.007 at 3 Gyr to 0.2 at present-day, using Eq. 2 from Fuller et al. (2016). [Note that this equation allows us to determine k_2/Q from dynamical parameters and t_α without having to specify k_2 and Q individually.] The semi-major axis evolution in Fig. 2.3 considers only planet tides. For Callisto, the effect of satellite tides on semi-major axis gets within an order of magnitude of that of planet tides when the element values peak (see below), and for Ganymede, satellite tides get within a factor of two at the peak. These peaks are so short-lived, however, that we can neglect their effects on the long-term outwards motion of the satellites.

The Fuller model suggests that over the past 1.5 Gyr, Callisto has migrated more than 30 per cent of its current orbital distance. The most dynamically relevant consequence of this is that it would have passed through several locations of MMRs, which are marked. Note that the distance ratio between Io, Europa, and Ganymede never changes by virtue of the Laplace resonance. All of them though are on diverging orbits with Callisto because Callisto is pushed away faster. Diverging orbits mean that Callisto could never get caught in an MMR with the other moons since the planet torques pushing Callisto outwards would be stronger than the resonance torques from the other satellites trying to keep Callisto in an MMR (e.g., Dermott et al., 1988).

Of course there are uncertainties associated with the migration scenario shown in Fig. 2.3. With regards to Io, Europa, and Ganymede, there are uncertainties in the astrometry data used to get $t_{\rm tide}$ and from there t_α, and we do not know when the Laplace resonance was established. For the purposes of providing an example, Fig.

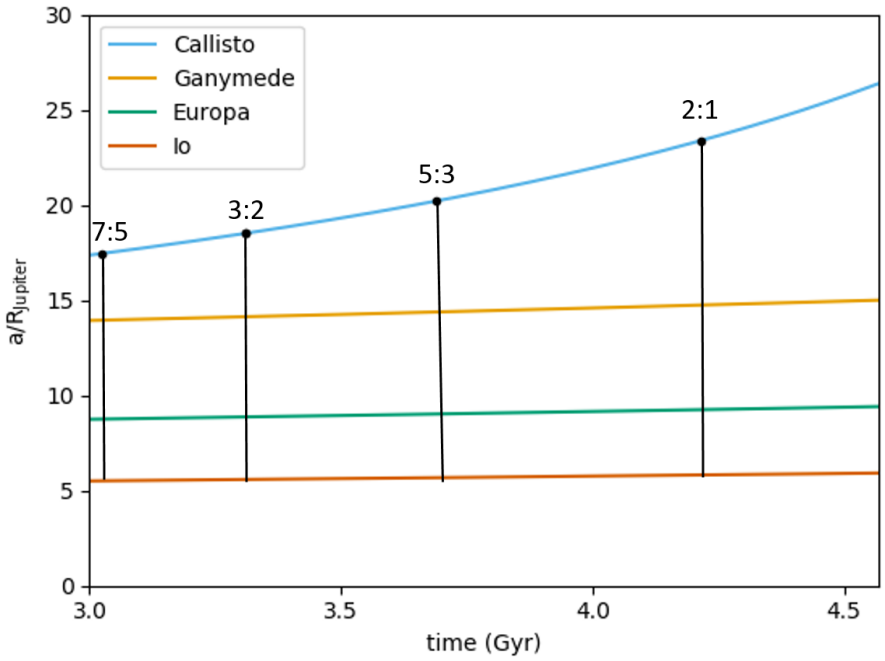

Figure 2.3: Semi-major axis evolution for the Galilean satellites over the past 1.5 Gyr assuming a resonance locking scenario as in Fuller et al. (2016). The t_α values for Io, Europa, Ganymede, and Callisto are 44, 101, 217, and 70 Gyr. The corresponding present-day $t_{\rm tide}$ values are 20 Gyr for the Laplace resonance and 2.7 Gyr for Callisto. To justify the time span shown, it is assumed that the Laplace resonance began before 3 Gyr. Nominal locations of low-order resonances between Callisto and Ganymede are indicated.

2.3 shows the Laplace resonance as being intact for the last 1.5 Gyr. With regards to Callisto, the value of $t_{\rm tide} \approx 2$ Gyr suggested by Fuller et al. (2016) has not yet been confirmed by astrometry, though the example of Titan suggests that rapid motion is possible (Lainey et al., 2020). For all moons, we do not know if all are in a resonance lock, if some are, or when it started.

2.3.2 Mean-motion resonances

If Callisto has passed through MMRs with the inner Galilean moons, then it is important to understand how these transient resonant torques would have affected Callisto's orbit. To begin, being in an MMR is able to increase the eccentricity, e, or inclination, i, of a body in either an eccentricity-type or inclination-type resonance. At low order, resonances can be stabilizing, so once entered, a body would have a hard time exiting the resonance without the help of an external force or chaos driven by resonance overlapping (Dermott et al., 1988). Bodies can only enter an MMR if they are on converging orbits otherwise the stronger tidal planetary torque on the outer body causing the orbits to diverge would be enough to disrupt the MMR. Since Callisto is on a diverging orbit with the inner Galilean moons in the Fuller Model, it would have passed through MMRs without getting caught.

Crossing through resonances would have excited Callisto's eccentricity or inclination (Peale, 1986). Dermott et al. (1988) give equations for the amount that the orbital elements increase by upon passage through first- and second-order resonances. The details are worked through in Peale (1986) and Murray and Dermott (1999) to

arrive at the third-order resonance as well. The equations are derived by calculating the Hamiltonian of the system before and after entering a resonance. These theoretical expressions are then tested numerically in Dermott et al. (1988) to understand if and when the theory holds up. They find that in systems where all second-order resonances are well-separated, the theory is valid. Two resonances are well-separated if the distance between them is greater than the sum of half their resonance widths. If there is overlap, Dermott et al. (1988) find that satellites can hop between resonances and experience chaos, but they still sometimes obey the resonance crossing theory. The latter is true in particular for the less massive satellite and for eccentricity resonances more than inclination ones. The authors argue that the theory applies when the rate of semi-major axis oscillation in a resonance (i.e., librating within the resonance width in one period) is faster than the tidal semi-major axis migration rate. Callisto satisfies this latter criterion, even though some of its resonances are not well-separated; we discuss this issue further in Section 3.3 below.

The equations for the final eccentricity or inclination of the inner body after passing through a q-order resonance, x_q, are below and assume that the element value before the resonance crossing is zero:

$$\begin{aligned} x_1 &= \left[\frac{2\sqrt{6} f(\alpha) \left(m'/M\right) \alpha}{p^2 + (p+1)^2 \left(m/m'\right) \alpha^2} \right]^{1/3} \\ x_2 &= \left[\frac{(32/3) f(\alpha) \left(m'/M\right) \alpha}{p^2 + (p+2)^2 \left(m/m'\right) \alpha^2} \right]^{1/2} \\ x_3 &= \frac{9\sqrt{2} f(\alpha) \left(m'/M\right) \alpha}{p^2 + (p+3)^2 \left(m/m'\right) \alpha^2}. \end{aligned} \tag{2.7}$$

Each equation is for a $p : p + q$ resonance. The unprimed m's and a's are the mass

and semi-major axis for the inner body, and the primed ones are for the outer body. M is the central body's mass. $\alpha = a/a'$ is the ratio of the inner body's semi-major axis to the outer body's. $f(\alpha)$ is a function of Laplace coefficients commonly used in Hamiltonian mechanics (Murray and Dermott, 1999) and is different depending on the order of the resonance and the type (i.e., eccentricity vs. inclination and inner body vs. outer body). For $q > 1$, we make the same assumption that Dermott et al. (1988) do that the final element values hold true for mixed resonances (e.g., ii') as well as pure ones (e.g., i^2, i'^2) so long as the correct $f(\alpha)$ is used.

The final element values for the outer body after passing through a $p : p + q$ resonance have the same form except every factor of α outside of the Laplace coefficients becomes α^3, every factor of α^2 becomes α^4, and each m and m' is swapped for the other.

We note that in Dermott et al. (1988) it is stated that $e_q = 2i_q$. However, Murray and Dermott (1999) claim that $e_q = i_q$ because the derivations of both values are the same whether one starts with eccentricity or inclination angular momentum. Here we follow the convention of Murray and Dermott (1999) and use the same equations to calculate both e_q and i_q.

Applying these equations to Callisto's inclination, we ask: do there exist resonances with the inner Jovian satellites, Io, Europa, and Ganymede that could have excited Callisto's inclination? Note that inclination-type resonances are only possible in even-ordered resonances or mixed resonances that have pairs of inclination terms, so we will only consider $p : p+2$ resonances, i^2, ii', i'^2 (Murray and Dermott, 1999, Section 8.4). A conceptual reason for this is that there is no standard reference frame that appears in

the physics, so only the mutual inclination matters. There are two types of inclination-type resonances that affect the inclination of Callisto, $i-$Ganymede-$i-$Callisto and i^2-Callisto, denoted ii', i'^2.

For each of Io, Europa, and Ganymede, we calculate x_2 from Eq. 2.7 for $1 \leq p \leq 11$, plotted in Fig. 2.4a. All resonances but one increase Callisto's inclination to at or above its current value by a factor of 2-3. Theoretically, therefore, a resonance crossing could be responsible for Callisto's inclination.

Callisto's eccentricity has not been mentioned thus far because solid-body eccentricity tidal damping depends on its value of k_2/Q, which is unknown. However, if Callisto had passed through a second-order inclination-type resonance with Ganymede, then it would have soon thereafter passed through eccentricity-type resonances as well. Fig. 2.4b shows first, second, and third-order eccentricity boosts, of which the first and second-order ones could account for Callisto's present-day eccentricity. The next section will provide a more detailed investigation of whether the present-day eccentricity and inclination can be explained by passage through a resonance.

2.3.3 Inclination evolution

Assuming the semi-major axis migration model for the Galilean satellites from Fuller et al. (2016) (Section 3.1), we can track Callisto's inclination as it crosses MMRs with Ganymede and subsequently decays due to obliquity tides.

We will assume that inclination and obliquity are connected through the Cassini state relation (Ward, 1975a), generally appropriate for dissipative systems. For a syn-

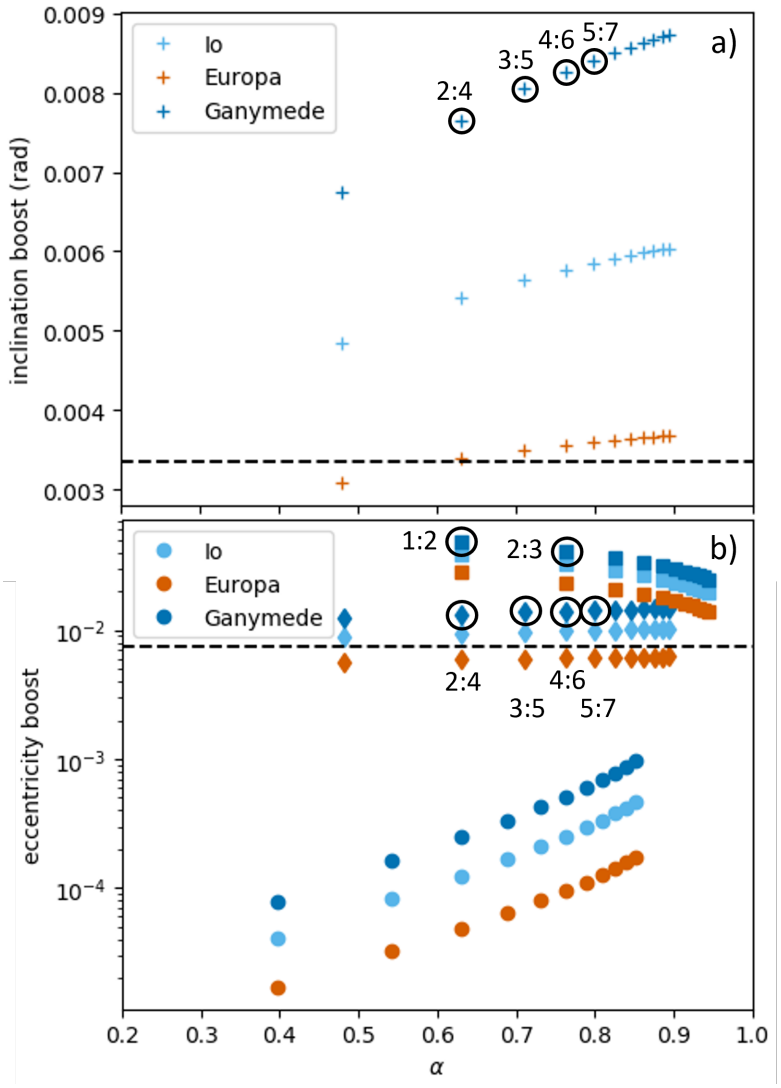

Figure 2.4: Callisto's element boosts after passing through $p : p + q$, $1 \leq p \leq 11$ resonances with Io (light blue), Europa (dark orange), and Ganymede (dark blue). a) Inclination boosts for second-order resonances since inclination-type resonances only occur for even-orders and b) Eccentricity boosts for first-order (square), second-order (diamond), and third order (circle) resonances. In exact resonance, $\alpha = [p/(p+q)]^{2/3}$, so α approaches 1 with increasing p. The second- and third-order resonances here are mixed x^{q-1}-Moon-$x-$Callisto resonances because they produce higher element boosts. The resonances that Callisto passes through in Fig. 2.3 with Ganymede are circled and labelled. The dashed lines are Callisto's current i and e.

chronously rotating satellite, this says that the spin pole, orbit normal, and Laplace plane normal vectors all lie in the same plane. The Cassini state relation is

$$\frac{3}{2}\left[\left(J_2 + C_{2,2}\right)\cos\theta_0 + C_{2,2}\right] p' \sin\theta_0 = c' \sin\left(i - \theta_0\right), \tag{2.8}$$

where J_2 and $C_{2,2}$ are the degree-2 gravity coefficients, θ_0 is obliquity, c' is an effective normalised moment of inertia, i is inclination, $p' = \Omega/\dot{\Omega}_{\rm orb}$, Ω is spin frequency, and $\dot{\Omega}_{\rm orb}$ is the precession rate of the longitude of the ascending node (e.g., Chen et al., 2014).

Titan is the only icy satellite whose obliquity has been directly measured (Stiles et al., 2008), and for the Cassini State relation to hold in Titan's case, $c' = 1.9c$, where c is the usual normalised moment of inertia, as derived from gravity moments and the hydrostatic assumption (Bills and Nimmo, 2011). The result, a normalised moment of inertia above 0.4, suggests that Titan's ice shell and interior are decoupled due to a subsurface ocean (Bills and Nimmo, 2011; Baland et al., 2011). Since Callisto, like Titan, is believed to have a subsurface ocean, it is reasonable to assume that $c' > c$. For specificity, below we will assume $c' = 1.6c$ (implying a present-day obliquity of $-0.3°$ instead of $-0.12°$ for $c' = c$), though of course the actual relationship is currently unknown. We note that Baland et al. (2012) predict an obliquity as large as $-0.25°$ for a decoupled shell, while for a solid Callisto, Bills (2005) and Noyelles (2009) obtain values as large as -1.7 and $-0.27°$ respectively. As the numerical factor in front of c increases, obliquity will be larger and generate stronger obliquity tides for a given inclination. Stronger obliquity tides would then damp out inclination faster.

Using the measured value of $C_{2,2}$ from Anderson et al. (2001a), we derive $c = 0.353$ from the Darwin-Radau relation, which assumes hydrostatic equilibrium:

$$C_{2,2} = \frac{1}{4}\left(\frac{\Omega^2}{\frac{4}{3}\pi\rho_{\rm sat}G}\right)\left(\frac{5}{1+\left(\frac{5}{2}-\frac{15}{4}c\right)^2}-1\right), \tag{2.9}$$

where Ω is spin frequency, $\rho_{\rm sat}$ is the satellite's bulk density, and G is the gravitational constant.

Callisto is in a synchronous rotation state, so the spin frequency is the same as the orbital frequency and decreases as it migrates outwards. Making the hydrostatic assumption means that as Callisto's spin frequency changes, the amount of spherical flattening will change as well. J_2 and $C_{2,2}$ must therefore be calculated at every time step in Callisto's outwards migration. Note that J_2 and $C_{2,2}$ have not been independently measured for Callisto, so we do not know that the hydrostatic assumption is correct, but they can be determined assuming that Callisto is hydrostatic via $J_2 = 10C_{2,2}/3$.

The $\Omega_{\rm orb}$ circulates due to the additional gravitational force arising from Jupiter's oblateness, the inner Galilean moons, and the Sun, which is treated as an external perturber. The way we calculated Callisto's $\Omega_{\rm orb}$ precession is as follows. The terms are either from internal or external perturbers as per the Lagrange equations for planetary motion (e.g., Champenois and Vienne, 1999; Noyelles, 2009).

$$\begin{aligned}\frac{d\Omega_{\rm orb}}{dt} = -\frac{3}{2}n_4 J_{2p}\left(\frac{R_p}{a_4}\right)^2 &- \sum_{i=1}^{3}\frac{1}{4}n_4\alpha_{i,4}\frac{m_i}{M}b^{(1)}_{3/2}(\alpha_{i,4}) \\ &- \frac{1}{4}n_4\alpha^2_{4,s}\frac{m_s}{M}b^{(1)}_{3/2}(\alpha_{4,s})\end{aligned} \tag{2.10}$$

The subscripts 1-3 refer to Io, Europa, and Ganymede respectively, p refers to the planet,

namely Jupiter, and s refers to the Sun. J_{2p}, R_p, and M are Jupiter's degree-2 gravity coefficient, radius, and mass. n_4 and a_4 are Callisto's mean-motion and semi-major axis. m_i is the i^{th} object's mass. $\alpha_{i,j} = a_i/a_j$ is the ratio of the i$^{\text{th}}$ object's semi-major axis to the j$^{\text{th}}$ object's. $b_s^{(j)}(\alpha)$ are Laplace coefficients as a function of α (Murray and Dermott, 1999). With Jupiter at the centre of the system, the semi-major axis of the Sun is just the heliocentric semi-major axis of Jupiter. In the case of Callisto, precession due to Jupiter's oblateness is smaller than precession due to Ganymede, unlike all other Galilean moons whose precessions are dominated by Jupiter's oblateness.

Regarding the effects of tidal dissipation, we take into account the fact that dissipation in the primary decreases a satellite's inclination as well as dissipation in the satellite (Chyba et al., 1989). The Mignard equations for how the Moon's orbital elements evolve due to dissipation in the primary and secondary consider only solid-body satellite tides (Mignard, 1981). We use the adaptation in Chen and Nimmo (2016) to include the effect of ocean satellite tides in addition to solid-body tides:

$$\begin{aligned}
\left(\frac{di}{dt}\right)_{\text{p}} &= -\frac{3}{4}\frac{k_{2,p}}{Q_p}\left(\frac{R_p}{a}\right)^5 \frac{m}{M} n \sin i \frac{\Omega_p}{\Omega_p - n}\sqrt{1+\frac{m}{M}}\cos\theta_{0,p} \\
\left(\frac{di}{dt}\right)_{\text{s}} &= -\frac{a\dot{E}_{\text{obl}}}{GMm\tan i}\sqrt{1+\frac{m}{M}} \\
\frac{di}{dt} &= \left(\frac{di}{dt}\right)_{\text{s}} + \left(\frac{di}{dt}\right)_{\text{p}},
\end{aligned} \tag{2.11}$$

where the subscript p denotes quantities for the planet and the subscript s for the satellite. $\dot{E}_{\text{obl}}$ includes both ocean (Eq. 2.3) and solid-body (Eq. 2.1) dissipation in the satellite.

Note that in the limit where $n \ll \Omega_p$, $m \ll M$, and $\cos\theta_{0,p} = 1$, $(di/dt)_p$ sim-

plifies to the expression in Chyba et al. (1989) and $(di/dt)_s$ simplifies to the expression in Chen and Nimmo (2016).

Eq. 2 of Fuller et al. (2016) calculates $k_{2,p}/Q_p$ at Callisto's orbital frequency and is a measure of how deformable Jupiter is :

$$\frac{k_{2,p}}{Q_p} = \frac{1}{3n}\frac{M}{m}\left(\frac{a}{R_p}\right)^5 \frac{1}{t_{\rm tide}}. \tag{2.12}$$

The four most recent resonances with Ganymede going backwards in time are 2:1, 5:3, 3:2, and 7:5 (the same resonances with Europa are 4:1, 10:3, 3:1, and 14:5) as shown in Fig. 2.3. Second-order inclination resonances can either excite just the inner body's inclination (i^2), just the outer body's inclination (i'^2), or both (ii'). We consider the sum of the second-order inclination resonances that excite Callisto's inclination (i'^2 and ii'). Even though the second-order resonances are not well-separated, at least for the most recent 2:1 crossing, Dermott et al. (1988) note that there are times when the resonance crossing theory still holds even for poorly-separated resonances (see the discussion in section 2.3.2). They speculate that the theory could still hold for the less massive satellite in a pair and if the semi-major axes of the satellite are expanding adiabatically (i.e., the tidal semi-major axis migration rate is slower than the resonant semi-major axis libration rate). Callisto and Ganymede are roughly the same mass, and the tidal expansion rate is much slower than the resonant libration rate as calculated from Eq. 15 of Dermott et al. (1988). These are not guarantees, of course; understanding in detail which second-order resonances would excite Callisto's inclination would only be possible with N-body simulations that take into account all of the necessary resonant

physics. That is outside the scope of this work.

We assume that Callisto acquires the inclination boost over a finite amount of time and not instantaneously. We approximate that the inclination increases exponentially as Callisto approaches the exact value of the resonance (this assumption has not been tested numerically, but correctly reproduces the total orbital element boost - see below). The resonance crossing time-scale, $\tau_{\rm res}$, is the time it takes Callisto's and Ganymede's motions to cross the full resonance width:

$$\tau_{\rm res} = \frac{\Delta a}{\dot{a}} = \frac{2a}{\dot{a}} \left[\frac{16}{3} \left(\alpha \frac{m'}{M} + \frac{m}{M} \right) f(\alpha) z^q \right]^{1/2}, \tag{2.13}$$

where Δa is the full resonance width, $\dot{a}$ is the migration rate from Eq. 2.6, and z^q is either e^q or $\sin(i/2)^q$ (Dermott et al., 1988). The rate of eccentricity and inclination increase as Callisto approaches the resonance is taken to be

$$\frac{dx}{dt} = \frac{x_q}{2} \frac{1}{\tau_{\rm res}} \exp(-|t - t_{\rm res}|/\tau_{\rm res}), \tag{2.14}$$

where $t_{\rm res}$ is the time where the exact $p : p + q$ resonance occurs, and x_q is given by (2.7). When integrated over time, this expression delivers the correct total increase in orbital element (x_q).

To generate Fig. 2.5, we let Callisto's inclination increase as it approaches the resonance (Eq. 2.14) and decay due to tides raised on the planet and satellite obliquity tides in both a subsurface ocean and in the solid body (Eq. 2.11). All of the physical and dynamical parameters used can be found in Tables 2.2 and 2.3. The inclination evolution has three free parameters since the drag coefficient is taken to be 0.002: t_α, the resonance locking migration time-scale, d, the thickness of the ice shell overlying

Callisto's ocean (which controls the dissipation rate), and the solid-body k_2/Q, which controls the solid-body obliquity tide dissipation rate. k_2/Q can be solved for, however, using Callisto's eccentricity evolution, which we analyse in the next section. This means for every t_α, there is one k_2/Q which allows us to recover Callisto's eccentricity, and that is the k_2/Q that we use for Callisto's solid-body obliquity tides as well. In the example shown in Fig. 2.5, where $t_\alpha = 70$ Gyr, $d = 150$ km, and $k_2/Q = 0.045$, the inclination evolution that includes the sum of both resonance excitations matches Callisto's present-day inclination. The predicted final obliquity from the Cassini state relation is $-0.3°$.

We explored other t_α and d values to determine parameter pairs that could match Callisto's present-day inclination. For different pairs of values, we carried out the full inclination evolution calculation and determined the relative error between the model's final inclination and the actual present-day value. Fig. 2.6a plots the error contours showing the trade-off between d and t_α. There is a different solid-body k_2/Q for every t_α, and it is constrained by fitting the eccentricity evolution in the next section. Longer migration time-scales require a thicker lid to reproduce Callisto's inclination whereas shorter migration time-scales require a thinner or even absent lid. This is because longer migration time-scales mean that the most recent resonance crossing happened earlier in time, and so thicker lids are needed to hamper ocean dissipation and preserve the inclination for longer.

The accuracy of our results depends on the choice of Callisto's current orbital elements. We have used JPL HORIZONS, which provides Callisto's mean inclination

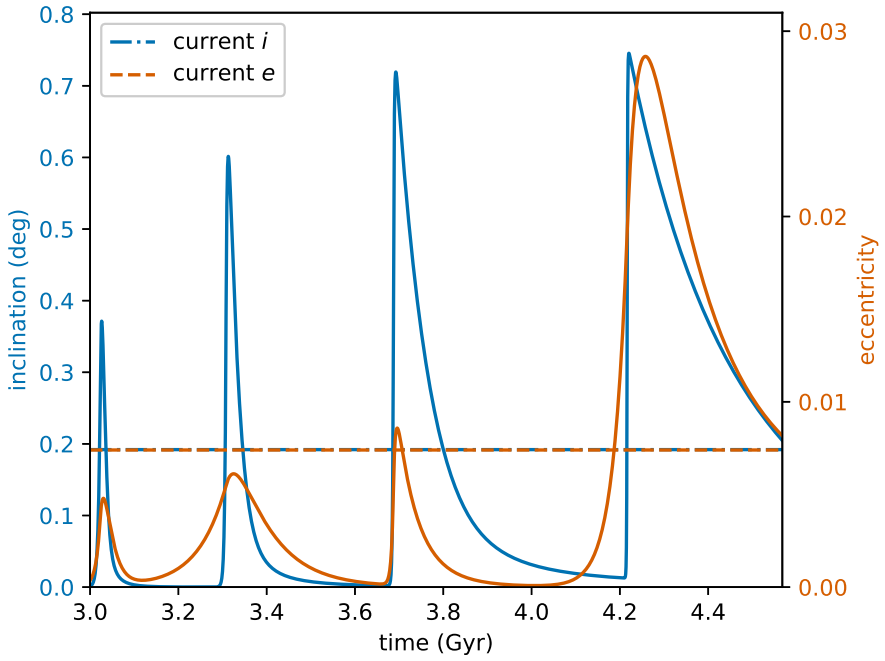

Figure 2.5: Callisto's inclination (left, blue) and eccentricity (right, orange) evolution for $t_\alpha = 70$ Gyr, $d = 150$ km, and solid-body $k_2/Q = 0.045$. The inclination boosts are sums of the $i-$Ganymede-$i-$Callisto and i^2-Callisto resonances, and the eccentricity boosts are the $e-$Callisto (e^2-Callisto for second-order) resonances. This model is able to reproduce Callisto's present-day orbital elements.

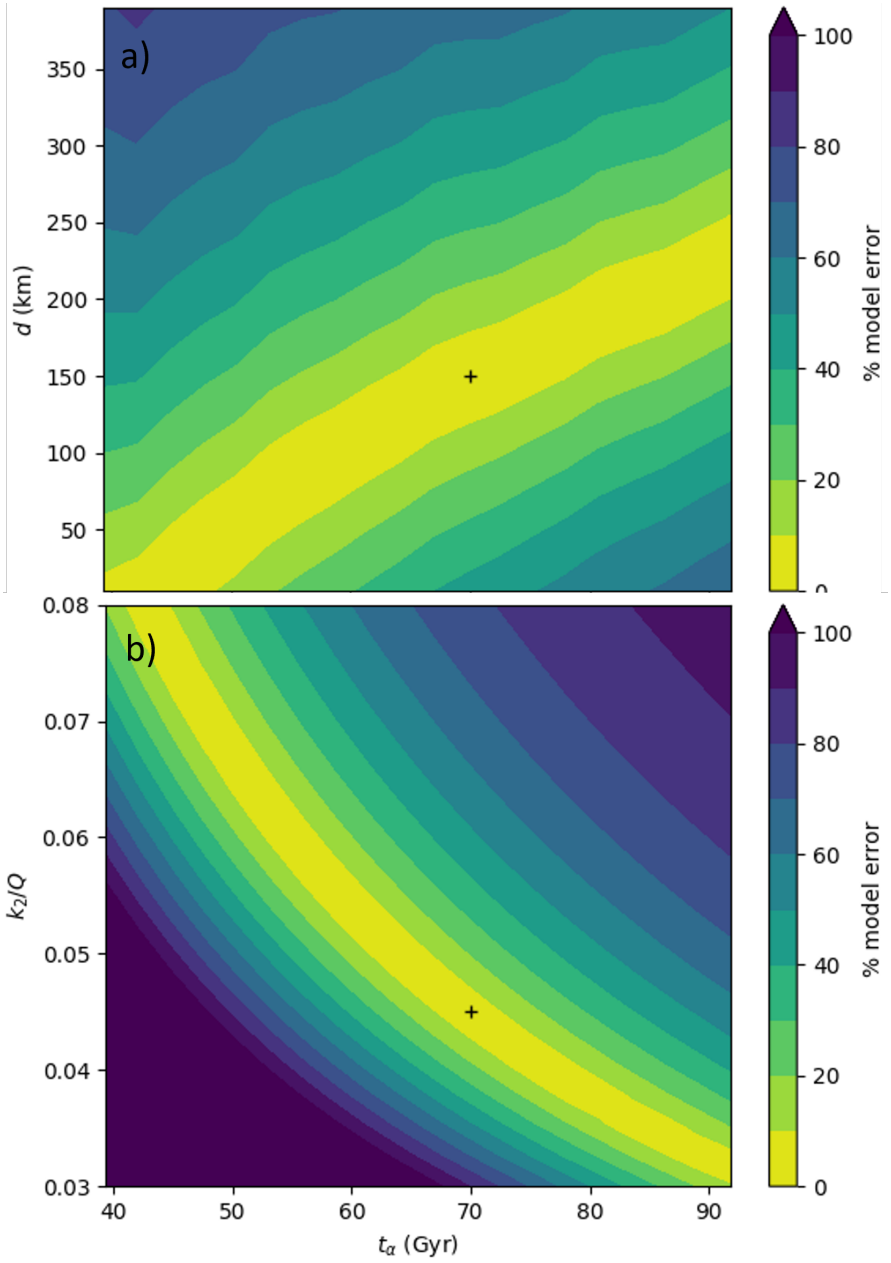

Figure 2.6: The error between the a) inclination and b) eccentricity evolution models and Callisto's present-day values assuming different t_α, d, and k_2/Q. k_2/Q for the solid-body obliquity tide component in the inclination contour plot is fixed for every t_α and is the value used to minimize the eccentricity error in the right plot for a given t_α (i.e., the yellow band). The "+" marks the parameters used in Fig. 2.5.

with respect to the local Laplace plane. However, other ways of determining Callisto's exact inclination yield different results, e.g., a frequency analysis approach yields 0.257° (Noyelles, 2009). Using as a baseline 0.257° instead of 0.192° would change our results by about 30 per cent. Given the order-of-magnitude uncertainties in other parameters of interest we are not too concerned by this particular source of uncertainty, though it would obviously be desirable to resolve it in future work.

We also save for future work the task of keeping track of how the Laplace plane of Callisto changes as it migrates away from Jupiter. This would affect the reference plane from which the inclination is measured and thereby change the true value of both the inclination and the obliquity.

2.3.4 Eccentricity evolution

If Callisto is passing through values of semi-major axis that correspond to inclination-type resonances, then if the eccentricity-type resonances are well-separated, we would expect eccentricity boosts as well. We track Callisto's eccentricity evolution to see if Callisto's full orbital history can be made self-consistent. The Mignard equations for eccentricity evolution due to dissipation in the primary and satellite are

$$
\begin{aligned}
\left(\frac{de}{dt}\right)_{\rm p} &= \frac{3}{2}\frac{k_{2,p}}{Q_p}\left(\frac{R_p}{a}\right)^5 \frac{m}{M}\left(1+\frac{m}{M}\right)\frac{n^2}{\Omega_p - n}\left(\frac{\Omega_p}{n}\cos\theta_{0,p}\cos i\frac{f_4}{\beta^{10}} - \frac{f_3}{\beta^{13}}\right) \\
\left(\frac{de}{dt}\right)_{\rm s} &= 3\frac{k_{2,s}}{Q_s}\left(\frac{R_s}{a}\right)^5 \left(1+\frac{M}{m}\right) n\left(\cos\theta_{0,s}\frac{f_4}{\beta^{10}} - \frac{f_3}{\beta^{13}}\right) \\
\beta &= \sqrt{1-e^2}, \\
f_3 &= 9e + \frac{135}{4}e^3 + \frac{135}{8}e^5 + \frac{45}{64}e^7, \quad f_4 = \frac{11}{2}e + \frac{33}{4}e^3 + \frac{11}{16}e^5 \\
\frac{de}{dt} &= \left(\frac{de}{dt}\right)_{\rm s} + \left(\frac{de}{dt}\right)_{\rm p},
\end{aligned}
\tag{2.15}
$$

where, as above, the subscript p is for planet quantities and s is for satellite quantities. Note that for eccentricity tides, dissipation in the primary increases the eccentricity, which is opposite to its effect on inclination.

In the limit where $n \ll \Omega_p$, $m \ll M$, $\cos\theta_{0,p} = 1$, and $e \ll 1$, $(de/dt)_p$ simplifies to the expression in Peale et al. (1980) adapted from Goldreich and Gold (1963) with a difference in coefficents of about 15 per cent. $(de/dt)_s$ simplifies to the standard solid-body eccentricity decay rate (e.g., Peale et al., 1980). We ignore ocean eccentricity tides because they produce negligible dissipation. To convert the Peale et al. (1980) expressions, which assume a constant tidal phase lag, to the Mignard equivalent, which assumes a constant tidal time lag, requires setting $\Delta t_s = 1/(nQ)$ where Q is the tidal quality factor. We also took $\Delta t_p = 1/(2\Omega_p Q)$. Planets have the factor of two in the denominator because they go through two cycles of tidal flexure in one rotation period, whereas satellites undergo just one cycle of flexure every time they complete a rotation (Kaula, 1964). Expressions that assume a constant time lag can be made equivalent to expressions that assume a constant phase lag only at one particular frequency. In reality,

both Δt and Q are expected to be frequency-dependent, but there is little agreement on the nature of this frequency-dependence.

Solid-body eccentricity tides require a k_2/Q for Callisto that is unknown because its internal structure is not well-constrained (Moore and Schubert, 2003). That means that for Callisto's eccentricity evolution, the two free parameters are k_2/Q and t_α. Since the inclination evolution depends on t_α, d, and k_2/Q, we have three unknowns and two constraints. Thus, the coupled inclination-eccentricity problem allows us to determine both d and k_2/Q for a given t_α. Because of its uncertainty, we here treat the solid-body k_2/Q as a constant (see below).

Fig. 2.5 shows Callisto's eccentricity evolution as the eccentricity increases with resonance crossings and decays with solid body eccentricity tides. For $t_\alpha = 70$ Gyr, $k_2/Q = 0.045$ to make Callisto's eccentricity evolution match the present-day eccentricity. Eccentricity resonances are first-order where possible, and the rest, including all inclination resonances, are second-order. First-order resonances have a wider resonance width (Eq. 2.13), which explains why for the first and third resonances, eccentricity has a broader peak than inclination. Just as for the inclination evolution, we varied t_α and k_2/Q to find the error between Callisto's present-day eccentricity and the value obtained from our models (Fig. 2.6). There is an inverse relationship between t_α and k_2/Q, so longer migration time-scales require a less dissipative solid-body to reproduce Callisto's eccentricity whereas shorter migration time-scales require the solid-body to be more dissipative.

2.3.5 Summary

It is possible that Callisto's current inclination and eccentricity are remnants of recent resonance crossings between Callisto and Ganymede while both migrated away from Jupiter in a frequency-dependent Q model. We have found combinations of t_α, d, and k_2/Q that reproduce Callisto's orbital elements within 10 per cent; our nominal values are $t_\alpha = 70$ Gyr, $d = 150$ km, and $k_2/Q = 0.045$ based on likely physical models of Callisto's interior.

It should be noted that tidal dissipation is more efficient the closer Callisto is to the inner satellites and Jupiter, so the only resonance needed to converge on Callisto's current inclination and eccentricity is the most recent one, a 2:1 resonance with Ganymede. Passing through a resonance with Ganymede means passing through a resonance with Europa and Io as well, but even a first-order resonance with Ganymede becomes a third-order resonance with Europa and a fifth-order resonance with Io. Fig. 2.4b shows that third-order eccentricity boosts are an order of magnitude below second-order eccentricity boosts, so it can be extrapolated that fourth-order inclination boosts must be several orders of magnitude lower than second-order inclination boosts and therefore can be neglected. As such, we need only to consider Ganymede's perturbation in our model. Since our uncertainty of how long Callisto or the other Galilean moons have been resonantly-locked to Jupiter for and what these migration time-scales are exactly, needing only one resonance in the last ~ 400 Myr is an advantage as it means Callisto's uncertain earlier history is not vital to this scenario.

2.4 Discussion

Even though our focus is on recovering Callisto's orbital elements, different aspects of the system are sure to be affected by Callisto and Ganymede crossing resonances with each other. These aspects need to be consistent with or provide evidence for the story in order for it to hold up. We first analyse the enhanced tidal heating that Callisto experiences as its orbital elements are excited since its surface shows no evidence of reheating. Secondly, we check that Ganymede's orbital elements are consistent with resonance crossings with Callisto. Thirdly, we discuss potential future work and make some testable predictions.

2.4.1 Heat flux

Callisto's surface is old, cratered, and shows no evidence of resurfacing (Greeley et al., 2000). Any orbital evolution we propose should satisfy these surface constraints. Too much surface heat flux from tidal dissipation would have potentially relaxed craters, created fractured features, or caused resurfacing.

Fig. 2.7 shows the heat flux for ocean obliquity tides, solid body obliquity tides, and solid body eccentricity tides as Callisto migrates with $t_\alpha = 70$ Gyr. Whether obliquity tides were stronger than eccentricity tides depended on the order of the resonance and how fast Callisto and Ganymede were crossing the resonance. First-order resonances have a wider resonance width, lowering the peak eccentricity heat flux. In the frequency-dependent Q model, resonantly-locked satellites migrate faster at greater

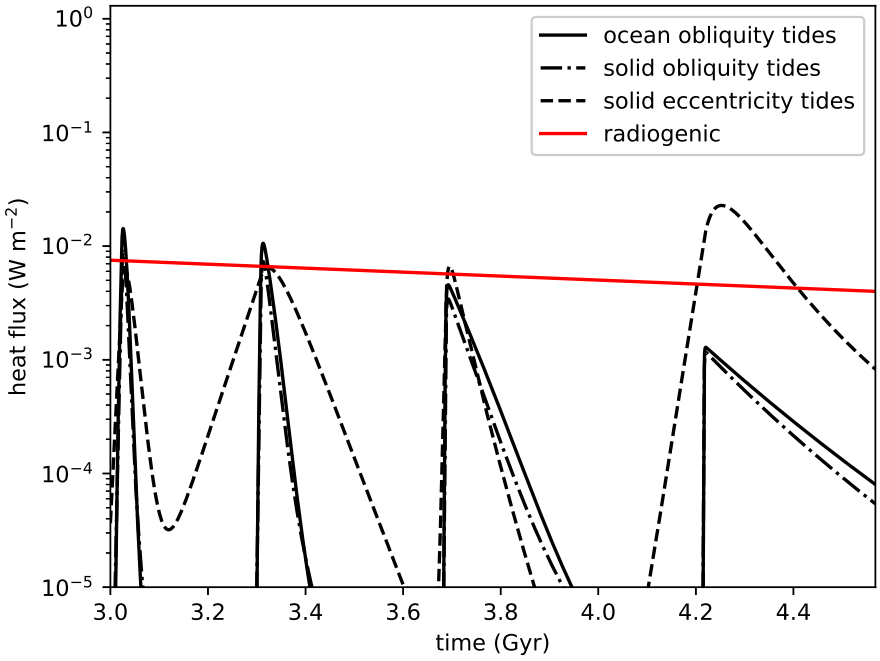

Figure 2.7: Callisto heat flux due to ocean obliquity tides, solid body obliquity tides, and solid body eccentricity tides. Ocean eccentricity tides are negligible. The periodic additions of heat could have prevented Callisto's ocean from freezing out completely in its history. The steady-state radiogenic heat flux estimates are from McKinnon (2006)

semi-major axis, so the resonance crossing time-scale decreases the farther out the resonance is.

The largest heat flux peak is due to eccentricity tides and reaches 30 mW m^{-2}. It is short-lived, dropping down to radiogenic heat levels within ≈200 Myr. An obvious question is whether a heat pulse of this kind is inconsistent with Callisto's observed lack of geological activity. Perhaps the most important consideration is that the time-scale for a conductive shell to respond to a change in bottom boundary conditions is d^2/κ ≈700 Myr for d=150 km. For a sluggishly-convecting shell as is conceivable with a 30 mW m^{-2} heat flux (McKinnon, 2006), this time-scale would be smaller by roughly an order of magnitude. Since the response time-scale is likely comparable to or greater than the heat pulse duration, a heating event at the base of the shell would only be weakly expressed near the surface.

Callisto's large craters in general appear unrelaxed (Schenk, 2002) and it does not possess small (<30 km) relaxed craters, unlike Ganymede (Singer et al., 2018). Unfortunately, placing an upper limit on heat flux based on unrelaxed craters is difficult given uncertainties in the relevant ice rheology and basal temperature (Bland et al., 2017).

Given the large uncertainties, a heat pulse peaking at 30 mW m^{-2} is not obviously inconsistent with the available constraints. Conversely, convection of Callisto's ice shell would tend to make long-term survival of an ocean more challenging (Reynolds and Cassen, 1979; McKinnon, 2006) and the addition of intermittent tidal heating might help to explain its present existence. Further investigations of these issues would be of

potential interest.

2.4.2 Ganymede

A further reality check is to see whether Ganymede's inclination and eccentricity evolution fit with its having passed through inclination and eccentricity-type resonances with Callisto. This is because if Callisto passed through resonances with Ganymede, then Ganymede would have passed through these resonances as well.

What we find is that Ganymede's inclination and eccentricity evolution lines up within a factor of two with the Fuller model when for Callisto $t_\alpha = 70$ Gyr and for Ganymede $t_\alpha = 217$ Gyr, $d = 150$ km,$\beta_2 = 0.85$, $\upsilon_2 = 1.04$, and $k_2/Q = 0.0025$ (Fig. 2.8). In contrast with Callisto, Ganymede's ocean obliquity tide dissipation is almost independent of ice shell thickness, because of how much faster it spins. Ganymede's periodic heat flux from tidal dissipation peaks at 45 mW m^{-2} in Fig. 2.9, which is higher than Callisto's peak heat flux despite having a k_2/Q an order of magnitude lower, because of its smaller semi-major axis. The inference that Ganymede's solid-body k_2/Q is so much lower than that of Callisto is somewhat surprising. One possible, although speculative, explanation is that a partially-differentiated Callisto could result in a large volume of mixed ice and rock having a viscosity dominated by the weaker phase. Because ice-like viscosities are much more readily subject to tidal heating than rock-like viscosities, the overall result would be enhanced dissipation in Callisto.

A complication is that Ganymede experienced a partial resurfacing event midway through its history Bland et al. (2009). The most likely explanation for this event

is that it spent time in a Laplace-like resonance (Showman and Malhotra, 1997) prior to entering the current Laplace resonance; this might also explain Ganymede's current eccentricity, but would require a k_2/Q at least an order of magnitude lower than we propose to avoid subsequent damping. Ganymede's eccentricity is not forced in the Laplace resonance like Io's and Europa's are, so its value will only decay because of tidal heating. In our model Ganymede could have experienced a heat-pulse as recently as 0.3 Ga (Fig. 2.9), but it is not clear that this heat pulse is sufficient to explain the inferred peak flux in excess of 100 mW m^{-2} (Bland et al., 2009).

Recovering Ganymede's orbital elements is more complicated than for Callisto because of the Laplace resonance with Io and Europa. At the present-day, its longitude of pericentre and longitude of the ascending node are not included in the Laplace resonance angles (e.g., Showman and Malhotra, 1997), but if its inclination and eccentricity had gotten large enough in the past, the resonance angles may have been different. In such a case, Ganymede's elements may have been forced to non-zero values for a period of time. Because of the Laplace resonance, the orbital dynamics of Ganymede are a more difficult problem than Callisto, and a full treatment is outside the scope of this work. At present, all we can say is that resonance crossings with Callisto are able to explain Ganymede's elements to within a factor of two.

2.4.3 Predictions and Future Work

In this work we have made predictions for the five free parameters of our orbital evolution model: Callisto's t_α, d, and k_2/Q and Ganymede's d and k_2/Q. A

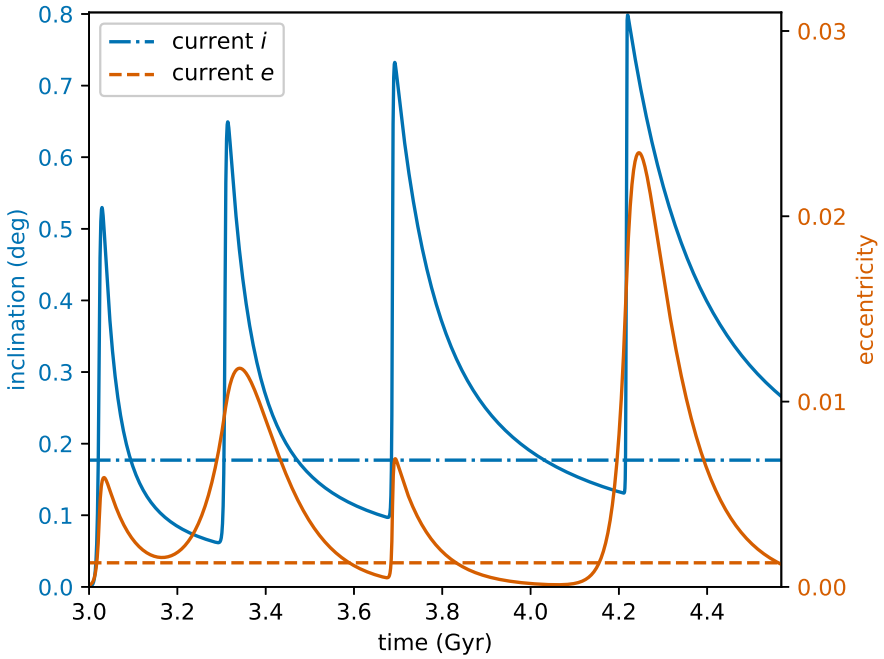

Figure 2.8: Ganymede's inclination (left, blue) and eccentricity (right, orange) evolution for $t_\alpha = 70$ Gyr for Callisto. $t_\alpha = 217$ Gyr, $d = 150$ km, $\beta_2 = 0.85$, $\upsilon_2 = 1.04$, and $k_2/Q = 0.0025$ for Ganymede. The inclination boosts are the sum of the i^2-Ganymede and $i-$Ganymede-$i-$Callisto resonances, and the eccentricity boosts are the $e-$Ganymede (e^2- Ganymede for second-order) resonances. Unlike for Callisto, Ganymede's inclination does not always zero out in between resonance crossings. Ganymede's inclination and eccentricity can also be accounted for by resonance crossings with Callisto.

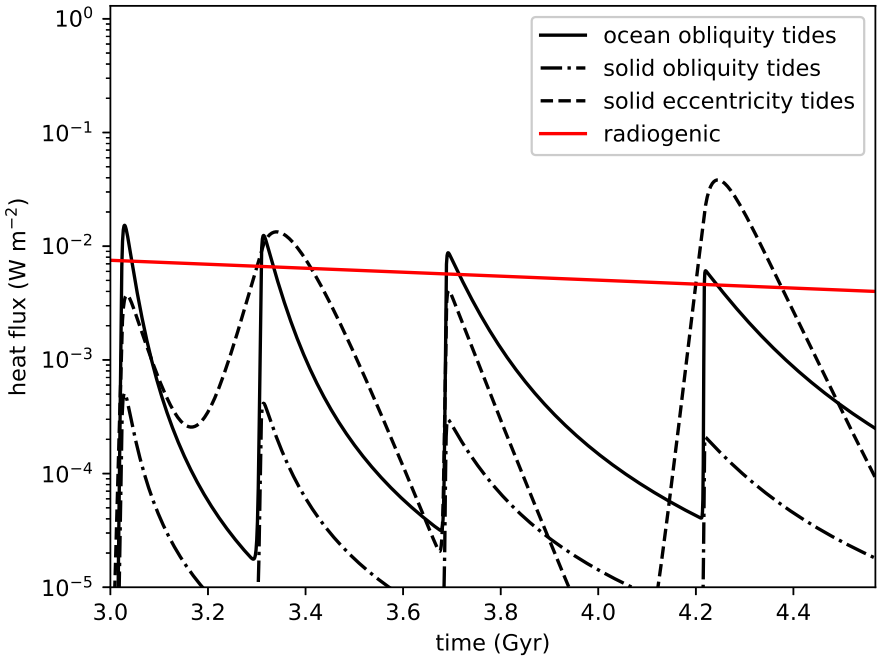

Figure 2.9: Ganymede's heat flux evolution for ocean obliquity tides and solid-body eccentricity tides as it passes through resonances with Callisto. Radiogenic heat flux estimates are from Bland et al. (2009).

benefit of this work is that we have isolated key, measurable parameters that can be observed by future space missions such as JUICE to test these predictions. Astrometry measurements would be able to track Callisto's and Ganymede's migration rate, $\dot{a}$, and give us t_α. This would also serve to validate or reject the possibility that Callisto's and Ganymede's migration affected a secular spin-orbit resonance that may be the cause of Jupiter's non-zero obliquity (Dbouk and Wisdom, 2023). Geodetic measurements can in principle provide the obliquities and tidal responses (k_2 and k_2/Q) of both satellites, and a combination of induction sounding and tidal measurements place constraints on d.

As our discussion in Sections 5.1 and 5.2 illustrates, the thermal evolution and consequences for surface geology are more complicated than we can address here. A particular drawback of our approach is that we assume a constant solid-body k_2/Q, while in reality this quantity is expected to change as the thermal state of the satellite changes. It would be of great interest to investigate coupled thermal-orbital evolution scenarios in the context of the resonance locking model.

A drawback of our model is that we use analytical solutions rather than N-body simulations in tracking the orbital dynamics. While this is appropriate for a first look, it may lead to important physics being missed. A recent study has shown that the 2:1 resonance between Ganymede and Callisto could have chaotic effects and pump the eccentricities up as high as 0.1 (Lari et al., 2020). Future work should include N-body simulations to capture details in the orbital dynamics such as these.

Two aspects of such scenarios are of particular interest. One is that Callisto,

like Iapetus, could conceivably have frozen in a shape acquired at an earlier time (faster spin rate): a "fossil bulge", like the Earth's Moon. This would have important consequences for interpretation of its shape and gravity. The second is that Callisto might have passed through a so-called Cassini State transition around 2.5 Gyr, which again could have had interesting consequences for its thermal evolution.

2.5 Conclusion

In this work we have followed two avenues to reconcile Callisto's present-day inclination with an expected short inclination damping time-scale: (1) its physical properties reduced dissipation; or (2) a recent dynamical event increased its inclination. We have shown that despite the uncertainties in Callisto's bottom drag coefficient, ocean thickness, and ice shell thickness, ocean obliquity tides are still strong enough to damp Callisto's inclination within a few billion years, which is incompatible with a primordial inclination. Incorporating a new tidal theory for dissipation in the giant planets, we have found scenarios in which Callisto's inclination and eccentricity are excited by crossing resonances with Ganymede and decay to their present-day values. Future measurements of Callisto's semi-major axis migration rate, obliquity, tidal response, and gravity moments will provide stringent tests of this proposed evolution model.

Acknowledgements

We thank Benoit Noyelles for the insightful and helpful review. Bruce Bills provided additional comments and suggestions. IM was financially supported by NASA under grant no. 80NSSC20K0570 issued through the NASA Solar System Workings program. This material is based upon work supported by the National Science Foundation Graduate Research Fellowship under Grant No. DGE-1842400.

Chapter 3

The thermal–orbital evolution of the Earth–Moon system with a subsurface magma ocean and fossil figure

This chapter is a slightly modified reprint of work previously published as Downey, B. G., Nimmo, F., & Matsuyama, I. (2023). The thermal–orbital evolution of the Earth–Moon system with a subsurface magma ocean and fossil figure. Icarus, 389, 115257.

Abstract

Various theories have been proposed to explain the Moon's current inclined orbit. We test the viability of these theories by reconstructing the thermal-orbital history of the Moon. We build on past thermal-orbital models and incorporate the

evolution of the lunar figure including a fossil figure component. Obliquity tidal heating in the lunar magma ocean would have produced rapid inclination damping, making it difficult for an early inclination to survive to the present-day. An early inclination is preserved only if the solid-body of the early Moon were less dissipative than at present. If instabilities at the Laplace plane transition were the source of the inclination, then the Moon had to recede slowly, which is consistent with previous findings of a weakly dissipative early Earth. If collisionless encounters with planetesimals up to 140 Myr after Moon formation excited the inclination, then the Moon had to migrate quickly to pass through the Cassini state transition at 33 Earth radii and reach a period of limited inclination damping. The fossil figure was likely established before 16 Earth radii to match the present-day degree-2 gravity field observations.

3.1 Introduction

The origins of the Moon's present-day orbital inclination have long been a mystery (e.g., MacDonald, 1964; Goldreich, 1966; Mignard, 1981; Touma and Wisdom, 1994). In the canonical Moon-forming giant impact theory (e.g., Canup and Asphaug, 2001), the Moon formed in the Earth's equatorial plane, i.e., a zero-inclination orbit, so the inclination had to arise during the Moon's outwards migration from Earth. In this work, we reconstruct the thermal-orbital history of the Moon to improve our understanding of how the Moon's orbit became inclined.

Various theories have been developed to explain excitations of the lunar incli-

nation, which we categorize into early and late scenarios. Two early possibilities are that soon after the Moon-forming giant impact, resonances between the proto-Moon and the debris-disk excited the inclination to 15° (Ward and Canup, 2000), and passage through the evection and eviction resonances at 4.6-6 Earth radii excited the inclination up to 9-13° (Touma and Wisdom, 1998). A late possibility posits a high obliquity (60-80°), high angular momentum early Earth that excited the inclination to $> 30°$ during the Moon's Laplace plane transition (LPT) at 16-22 Earth radii around 1-100 Myr after Moon formation (Ćuk et al., 2016b, 2021). One last possibility is that during the period $10 - 100$ Myr after Moon formation, collisionless encounters with planetesimals gravitationally excited the inclination to its present value (Pahlevan and Morbidelli, 2015).

Any viable inclination excitation has to contend with inclination damping due to tidal heating in the Earth and Moon (e.g., Chyba et al., 1989). In particular, Chen and Nimmo (2016) found that obliquity tidal heating in the ancient lunar magma ocean (Tyler, 2008) would have accelerated the inclination decay while the obliquity grew to large values during the Cassini state transition (CST) at ~ 30 Earth radii. Chen and Nimmo (2016) concluded that an early event can only be the source of the present-day inclination if the Moon's initial recession rate from the Earth were slow, the case for a weakly dissipative early Earth. This assumes that the magma ocean solidified in 100-200 Myr as supported by the lunar chronology data (e.g., Elkins-Tanton et al., 2011; Maurice et al., 2020, and references therin). If the early Earth was in fact dissipative, the inclination has to be from a late excitation mechanism. Our thermal-orbital model

is based on Chen and Nimmo (2016), but to provide an additional constraint, we include the evolution of the lunar figure using the model in Matsuyama et al. (2021).

The lunar figure plays an important role in constraining the Moon's orbital evolution. Not only does it have a putative fossil figure, recording the orbital state at an earlier point in time (e.g., Jeffreys, 1915; Lambeck and Pullan, 1980), but it affects the obliquity through Cassini states. Matsuyama et al. (2021) developed a lunar figure model which includes a fossil figure component and incorporates the effects of obliquity and eccentricity on the shape. Their fossil figure estimates are consistent with establishing a fossil figure at $\sim$ 13 Earth radii with obliquity -0.16° and eccentricity < 0.3. This is in contrast with other works that tried to determine the state of the orbit when the fossil figure froze in, with most of them requiring either large eccentricities of $0.15 - 0.6$ (Garrick-Bethell et al., 2006; Matsuyama, 2013; Keane and Matsuyama, 2014) or large semi-major axes of > 30 Earth radii (Garrick-Bethell et al., 2014; Qin et al., 2018). The range of results stems from different methods for estimating the size of the fossil figure from the present degree-2 gravity field. For example, Keane and Matsuyama (2014) subtract contributions from mass anomalies, Garrick-Bethell et al. (2014) subtract contributions from compensated topography, and Matsuyama et al. (2021) subtract the South Pole-Aitken basin contribution. Finally, Qin et al. (2018) differ because they freeze the fossil figure in gradually over 500 Myr, but they use the fossil figure estimates in Keane and Matsuyama (2014).

Other works besides Chen and Nimmo (2016) have tried to constrain aspects of the Moon's thermal-orbital history, but they did not focus on the origins of the

lunar inclination. First, Meyer et al. (2010) focused on whether the orbital parameters proposed in Garrick-Bethell et al. (2006) to explain the fossil figure were plausible. Second, Tian et al. (2017) focused on whether the evection resonance could extract excess angular momentum from an early fast-spinning Earth. Third, Daher et al. (2021) developed a sophisticated framework for tides in Earth's oceans to evolve the lunar orbit, but they do not include the effects of the lunar magma ocean or a fossil figure on the evolution of the Earth-Moon system.

In this paper, we use our coupled thermal-orbital model to match the present-day inclination and degree-2 gravity observations to answer the questions of how the Moon got its inclination and where the Moon's fossil figure froze in. We build on the thermal-orbital model in Chen and Nimmo (2016) and include a fossil figure component in the evolution of the lunar figure as in Matsuyama et al. (2021). We also include (1) crustal tidal heating using a combination of a constant k_2/Q and the model from Garrick-Bethell et al. (2010) (2) the effect of an overlying solid shell on magma ocean dissipation and (3) the eccentricity evolution. In Section 3.2, we describe the components of our thermal-orbital model. In Section 3.3 we find that a lasting early inclination requires that the Moon be more dissipative at present than in its past, and we present the necessary conditions to have a late inclination excitation as in Pahlevan and Morbidelli (2015) or Ćuk et al. (2016b). In Section 3.4 we discuss the importance of solid-body tides and the connection between the lunar fossil figure and the CST, and in Section 3.5 we summarize our results and discuss plans for future work.

3.2 Thermal-orbital evolution

We build a coupled thermal-orbital model based on Chen and Nimmo (2016) and Matsuyama et al. (2021) that evolves the lunar orbit and lunar figure with time while tracking the solidification of the magma ocean. The goal is to find the conditions consistent with an early compared to late inclination excitation all while reproducing the observations of the present-day lunar figure.

3.2.1 Orbital evolution

The Moon's orbital evolution is governed by tidal dissipation in the Earth and Moon. Tidal dissipation in the Earth causes the Moon's semi-major axis and eccentricity to increase and the inclination to decrease whereas tidal dissipation in the Moon causes the semi-major axis, eccentricity, and inclination to all decrease. We use the Mignard equations to evolve the Earth-Moon system under the influence of tidal effects from the Earth, Moon, and Sun (Mignard, 1979, 1980, 1981). The Mignard equations track the Moon's semi-major axis, inclination, and eccentricity, and the Earth's obliquity and spin rate. See Meyer et al. (2010) and Chen and Nimmo (2016) (includes corrected typos in Meyer et al. (2010)) for the Mignard equations and relevant terms. Their underlying principle is that there is a time lag, Δt, between when the perturbing body is directly overhead and when high tide on the body of interest occurs (Mignard, 1979). A larger Δt means greater tidal dissipation and therefore greater rates of change of the orbital elements.

The Δt of the early Earth is important for constraining the lunar evolution, but the past dissipative properties of the Earth are unknown and impossible to infer because dissipation in the Earth is currently dominated by ocean tides. Currently, $\Delta t \approx 600$ s (Munk and MacDonald, 1960), which if constant, implies the Moon formed $\sim$1 Ga. Therefore, Δt had to be much smaller earlier on. Adding to our uncertainty is the fact that dissipation in the Earth also depends on the Earth's k_2 Love number at the tidal forcing frequency, $k_{2,E}$, which would have been larger in the past for a warmer, molten Earth. Because of this, we fold any uncertainty in $k_{2,E}$ into that for Δt and treat $k_{2,E}\Delta t$ as a combined quantity. For $k_{2,E} = 0.3$ at the present, $k_{2,E}\Delta t \approx 180$ s, while according to our model, the average $k_{2,E}\Delta t$ over the past $\sim$4.5 Gyr is $\sim$50 s. Dissipation in the early Earth could have been weak because at the higher frequencies associated with the Earth's faster rotation, the ocean normal modes are less well-matched with the degree-2 tidal forcing (Bills and Ray, 1999). Weak dissipation and thus a small $k_{2,E}\Delta t$ of the early Earth is further supported by Zahnle et al. (2015) who suggest that the thermal blanketing effect of the Earth's early atmosphere would have limited tidal heating. Two recent studies on the ocean dynamics of the Earth seem promising, but we do not incorporate their findings yet because both are incompatible with the Moon-forming giant impact theory; Tyler (2021) and Daher et al. (2021) predict that the Moon formed at $44R_E$ $\sim$4.5 Ga. Daher et al. (2021) acknowledge this with the intention of focusing on early sources of tidal dissipation in future works.

We create a step function for $k_{2,E}\Delta t$, which, given the uncertainties discussed above, is a simple parameterization that allows us to start the Earth with weaker dissi-

pation then at a specific point in time switch to the enhanced tidal dissipation observed in the oceans today. To impose different orbital migration rates for the early Moon, we vary $(k_{2,E}\Delta t)_0$, and to keep the final semi-major axis accurate to within 10 per cent, we set $(k_{2,E}\Delta t)_f = 180$ s at 1.25 Ga. Tidally-laminated sediment data and Earth ocean tide modelling are consistent with the high rate of Earth dissipation beginning $\sim$1 Ga (Bills and Ray, 1999). We have also experimented with smoothly-varying (exponential) descriptions of $k_{2,E}\Delta t$ and find very similar results to those presented below.

One critique of a constant Δt formulation is that it is not consistent with the Moon's tidal response as observed in the GRAIL data (Williams and Boggs, 2015). However, despite the GRAIL data, it is still inconclusive which tidal model is most accurate and whether the lunar tidal response can be extrapolated to other planetary bodies (Williams and Boggs, 2015). Whatever the case, Touma and Wisdom (1994) found that various tidal formulations, including the Mignard equations, yield approximately the same evolution for the Moon over billion year timescales because what matters most is accounting for all tidal effects. In light of this, we prioritize evolving the lunar orbit to the present-day with a step function $k_{2,E}\Delta t$ model for the Earth's tidal dissipation. For the Moon, we calculate Q based on models for dissipation in the magma ocean and solid crust as described in Secs 3.2.3.1 and 3.2.3.2.

3.2.2 Cassini states and lunar figure

We assume that the Moon is always in a Cassini state, namely that the spin pole precesses about the orbit normal at the same rate as the orbit normal precesses

about the normal to the Laplace plane (e.g., Colombo, 1966; Peale, 1969; Ward, 1975a). The Laplace plane is the average precessional plane, which for the Moon is currently the ecliptic, the Earth's orbit plane. Torques on the lunar figure cause the spin pole to precess, and torques from the Earth's oblateness and the Sun cause the orbit pole to precess. These two rates of precession are equal only when the spin axis is tilted by the Cassini state obliquity. We expect all satellites damped to synchronous rotation to also be in a damped Cassini state (Ward, 1975a). In general there are four possible Cassini states. Close to the Earth, the Moon is in state 1, where the spin axis lies close to the orbit normal, and at around $34R_E$, it transitions to state 2, where the spin axis lies close to the ecliptic (e.g., Ward, 1975a). During the transition from state 1 to state 2, the magnitude of the obliquity increases rapidly which could lead to strong obliquity tidal heating and inclination damping. The lunar figure affects the spin pole precession and therefore the Cassini state obliquity, so it is important to have an accurate model of the size of the Moon's fossil and tidal-rotational bulges. The formulation in Matsuyama et al. (2021) includes the effects of obliquity and eccentricity on the Moon's deformation, quantified by the degree-2 gravity coefficients, J_2 and C_{22} (Kaula, 1964), and allows for both a fossil and a tidal-rotational component.

Equating the precessional torques on the lunar orbit to those on the lunar figure gives the Cassini state relation provided in Eq. 3.1 (Peale, 1969; Bills and Nimmo, 2008, 2011). A satellite's obliquity, θ_0, can be numerically solved for given various gravitational and orbital parameters. The Cassini state relation and the orbit precession

rate (e.g., Goldreich, 1966) are as follows:

$$\frac{3}{2}\left[(J_2 + C_{22})\cos\theta_0 + C_{22}\right] p \sin\theta_0 = c\sin\left(i - \theta_0\right) \tag{3.1}$$

$$\dot{\Omega}_{\rm orb} = -\frac{3}{2} n J_{2,E} \left(\frac{R_E}{a}\right)^2 - \frac{3}{4} n \frac{M_S}{M} \left(\frac{a}{a_E}\right)^3 \tag{3.2}$$

$$J_{2,E} = \frac{1}{3} k_{2,E} \left(\frac{\omega}{n_G}\right)^2 . \tag{3.3}$$

Here, a, n, i, and c are the lunar semi-major axis, mean motion, inclination, and normalized polar moment of inertia, $p = n/\dot{\Omega}_{\rm orb}$, where $\dot{\Omega}_{\rm orb}$ is the rate of nodal regression, M, R_E, $J_{2,E}$, $k_{2,E}$, a_E, and ω are the Earth's mass, radius, J_2, long-term Love number, heliocentric semi-major axis, and spin rate, $n_G = (GM/R_E^3)^{1/2}$ is the grazing mean motion about the Earth, and M_S is the Sun's mass. The first term in Eq. 3.2 is the torque from the Earth's oblateness on the lunar orbit, and the second term is the solar torque in the limit that $a \ll a_E$. The LPT happens when the solar torque becomes stronger than the Earth's, so when the second term in Eq. 3.2 is larger in magnitude than the first. The CST happens when the Moon's spin pole becomes closer to the Laplace plane pole than to the orbit normal, so when the numerically-solved for obliquity from Eq. 3.1 first flips from being negative (state 1) to positive (state 2).

The degree-2 gravity coefficients associated with the rotational and tidal potentials of the Moon averaged over the orbital and precession periods are given by

(Matsuyama et al., 2021)

$$< J_2 > = q^T \left[\frac{1}{3} + \frac{1}{32} \left(2 - 3\sin^2\theta_0\right) \left(8 + 12e^2 + 15e^4\right) \right] \tag{3.4}$$

$$< C_{22} > = q^T \frac{1}{256} \left(16 - 40e^2 + 13e^4\right) \left(1 + \cos\theta_0\right)^2 \tag{3.5}$$

$$q^T = \left(\frac{M}{m}\right) \left(\frac{R}{a}\right)^3, \tag{3.6}$$

where m, R, and e are the Moon's mass, radius, and orbital eccentricity. Using these equations and assuming that a fossil figure is established as an elastic lithosphere forms over a timescale much shorter than the orbital evolution timescale, the degree-2 gravity coefficients of the Moon including the fossil figure contribution can be written as

$$J_2 = (k_2^{\infty *} - k_2^{\infty}) < J_2^* > + k_2^{\infty} < J_2 > \tag{3.7}$$

$$C_{22} = (k_2^{\infty *} - k_2^{\infty}) < C_{22}^* > + k_2^{\infty} < C_{22} >; \tag{3.8}$$

asterisks denote the values when the fossil figure freezes in, and k_2^{∞} is the degree-2 long-term tidal Love number, which is a function of the lunar elastic lithosphere thickness. In this work we approximate the elastic lithosphere thickness by the crustal thickness, whose growth due to magma ocean solidification we describe in more detail below in Section 3.2.4. For greater elastic thicknesses, k_2^{∞} will be smaller indicating a more rigid body. Instantaneously establishing a fossil figure is simplistic compared to the long-term visco-elastic process in Qin et al. (2018), but out results differ by $\lesssim 25$ per cent.

We compute the long-term tidal Love number k_2^{∞} using the classical propagator matrix method (e.g., Sabadini et al. (2016)) and assuming a 4-layer interior structure consisting of a liquid core, mantle, magma ocean, and shell with the interior structure

parameters summarized in Table 3.1. As the magma ocean solidifies as described below, the core density is computed self-consistently so as to satisfy the mean density constraint assuming a 380 km core radius. We assume a fossil figure preserved by an elastic lithosphere because this is the first region to develop long-term elastic strength as the Moon cools. Therefore, the rigidity of all layers is set to zero except for the elastic lithosphere.

The term $(k_2^{\infty *} - k_2^{\infty})$ in equations 3.7 and 3.8 measures the relative rigidity of the Moon when the fossil figure freezes in $(k_2^{\infty *})$ to that from the instantaneous crustal thickness throughout the rest of the simulation (k_2^{∞}) in order to determine how well the lithosphere supports the stresses of the fossil figure at any point in time. The more rigid the Moon becomes from a growing elastic thickness (smaller k_2^{∞}), the less it will deform in the new rotational and tidal potential, and the more it will revert back to the fossil figure (larger $k_2^{\infty *} - k_2^{\infty}$). The fossil figure is the shape that without any external forces the body would adopt. We do not account for any long-term relaxation of the fossil stresses.

Where the fossil figure froze in is a variable in our model. Comparing the model results to the degree-2 gravity observations in Matsuyama et al. (2021) allows us to provide an estimate of the orbital state when the fossil figure froze in.

3.2.3 Tidal heating

Tidal heating in the Moon damps the inclination, eccentricity, and semi-major axis and is the key obstacle to the survival of an early inclination. The mechanisms for

tidal dissipation in the solid-body and magma ocean are different, so we provide details on each below.

3.2.3.1 Solid-body tidal heating

For solid-body tidal heating in the lunar crust, we use a combination of a visco-elastic model that depends on the Moon's Love numbers, viscosity, and rigidity and a constant k_2/Q model, where k_2 is the Moon's degree-2 potential Love number at the tidal forcing frequency and Q is the Moon's tidal quality factor. The visco-elastic model is used while the magma ocean is still present since Q could vary by several orders of magnitude as the crust and mantle are cooling. After magma ocean solidification, using just the visco-elastic model and a crustal viscosity of $\eta = 10^{19}$ Pa s produces values for Q on the order of 10^6-10^8, which would underestimate solid-body tidal heating at the present. Because of this, once the magma ocean is solidified, we switch to calculating solid-body tidal dissipation from a constant $k_2/Q = 6 \times 10^{-4}$, which is the value at the present-day (Williams and Boggs, 2015). A constant k_2/Q balances the competing effects of the Moon behaving more elastically at the higher tidal frequencies associated with smaller semi-major axes with the Moon becoming less dissipative as it cools after the solidification of the magma ocean.

For the visco-elastic model, we calculate the heating rate from Garrick-Bethell et al. (2010) and apply it in a thin layer above the magma ocean to crudely approximate tidal heating in a temperature-dependent medium. Note that we neglect dissipation in the deep interior beneath the magma ocean, which if present, would further increase

eccentricity and inclination damping. Eccentricity and obliquity tides create a tidal strain rate in the lunar crust, $\dot{\epsilon}$, which results in a volumetric tidal dissipation rate, W, whose equations are reproduced below from (Garrick-Bethell et al., 2010):

$$\dot{\epsilon}_e = f\left(\frac{h_2}{2.5}\right)\frac{n^3R^3}{Gm}e \tag{3.9}$$

$$W_e = \frac{2\dot{\epsilon}_e^2\eta}{1+(n\eta/\mu)^2} \tag{3.10}$$

$$W = W_e\left(1+\frac{\sin^2\theta_0}{7e^2}\right). \tag{3.11}$$

The constant f quantifies spatial variations in the strain rate and is of order unity, h_2 is the degree-2 displacement Love number at the tidal frequency, G is the gravitational constant, and η and μ are the viscosity and rigidity of the lunar crust. The eccentricity tidal strain rate, $\dot{\epsilon}_e$, has a corresponding heating rate, W_e (Ojakangas and Stevenson, 1989; Garrick-Bethell et al., 2010). To account for obliquity tides in the full heating rate, W, we approximate the ratio of eccentricity tidal dissipation to that of obliquity tides to be $\sin^2\theta_0/7e^2$. This is based on the standard tidal dissipation expressions in Peale and Cassen (1978) and Peale et al. (1980).

We compute h_2 and k_2 at the tidal forcing frequency using the propagator matrix method and the correspondence principle (e.g., Tobie et al., 2005a). For this computation, we assume the 4-layer interior structure described above, a Maxwell rheology, a mantle with a rigidity of 70 GPa and a viscosity of 10^{21} Pa s, a magma ocean, and a shell with a rigidity of 30 GPa and a viscosity of 10^{21} Pa s. The visco-elastic Love numbers are not sensitive to the assumed viscosities because the Maxwell time of the solid layers is significantly larger than the tidal forcing period, corresponding to

a nearly purely elastic response that is independent of the assumed viscosity and the forcing frequency.

Most of the crust is likely to be too cold and rigid to dissipate much energy, so we concentrate the dissipation in a layer of thickness δ at the bottom of the crust of total thickness d overlying the magma ocean. The thickness of this dissipative layer depends on the temperature profile and heat production of the crust and the conductive cooling of the magma ocean. Because all the layers considered are thin compared to the Moon's radius, a Cartesian geometry is appropriate.

For an unheated region, $(z < d - \delta)$, where z is depth into the crust, the temperature structure increases linearly with depth due to conductive cooling from the interior to the surface:

$$T(z) = T_0 + \frac{T_a - T_0}{d - \delta} z, \tag{3.12}$$

where T_0, T_m, and T_a are the temperatures of the surface, magma ocean (i.e., the base of the crust), and top of the dissipative layer. The interface temperature T_a at $z = d - \delta$ is determined by the sensitivity of the viscosity to temperature via the activation energy. For silicates, this e-folding temperature drop is roughly 50 K.

For an internally heated region, $(z > d - \delta)$, the solution to the temperature structure has a similar linear component to conduct heat from the magma ocean to the surface but includes terms to account for heat generation and diffusion in this layer:

$$T(z) = T_m - \frac{1}{\delta} (T_m - T_a) (d - z) + \frac{W}{2k} \left[\delta (d - z) - (d - z)^2 \right], \tag{3.13}$$

where k is the thermal conductivity and W is the internal volumetric heating rate from

Eq. 3.11. For simplicity, we assume that W is constant within the heated layer because the viscosity variation within this layer is small. It can be verified that this temperature profile gives the correct limits of T_m at $z = d$ and T_a at $z = d - \delta$.

If we specify the basal heat flux H_b, then the heat flux balance at the surface is

$$W\delta + H_b = k\frac{T_a - T_0}{d - \delta}, \tag{3.14}$$

and the heat flux balance in the heated region is

$$\frac{W\delta}{2} + H_b = k\frac{T_m - T_a}{\delta}. \tag{3.15}$$

Since we know the crustal thickness, d, from solidification of the magma ocean and the internal volumetric heating rate, W, from tides, we can solve for the basal heat flux H_b and δ simultaneously. Combining equations 3.14 and 3.15 gives rise to a cubic relation that can be solved numerically:

$$\frac{1}{2}W\delta^3 - \frac{1}{2}Wd\delta^2 + k\delta\left(T_m - T_0\right) - kd\left(T_m - T_a\right) = 0. \tag{3.16}$$

In the limit that the heat flux from cooling of the magma ocean is much greater than the internally generated tidal heating ($H_b \gg W\delta$), the thickness of the heated layer is proportional to the temperature contrast, $\delta \approx d(T_m - T_a)/(T_m - T_0)$ as expected.

The heat production rate in the crust is then $H_{\rm crust} = W\delta$, and the total solid-body energy dissipation in the shell is $\dot{E}_{\rm sol} = 4\pi R^2 H_{\rm crust}$. This can be broken down into an eccentricity tide component, $\dot{E}_{e,\rm sol}$ and obliquity tide component, $\dot{E}_{\theta,\rm sol}$ in the following way:

$$\dot{E}_{e,\mathrm{sol}} = \frac{7e^2}{7e^2 + \sin^2\theta_0}\dot{E}_{\mathrm{sol}} \tag{3.17}$$

$$\dot{E}_{\theta,\mathrm{sol}} = \frac{\sin^2\theta_0}{7e^2 + \sin^2\theta_0}\dot{E}_{\mathrm{sol}} \tag{3.18}$$

$$Q_{\mathrm{eff}} = \frac{3}{2}k_2\frac{n^5R^5}{G}\frac{\left(7e^2 + \sin^2\theta_0\right)}{\dot{E}_{\mathrm{sol}}}, \tag{3.19}$$

where Q_{eff} is the effective tidal quality factor to compare these tidal heating rates to the standard dissipation expressions in Peale et al. (1980). Once the magma ocean is solidified, we use Eq. 3.19 and a constant k_2/Q to calculate solid-body tidal heating. This equation assumes small eccentricity and obliquity (c.f., Wisdom, 2008) and so during the CST underestimates solid-body obliquity heating by a factor of 1.5-3 at the peak obliquity, which does not qualitatively change our results.

3.2.3.2 Magma ocean tidal heating

Tidal heating in the lunar magma ocean was a novel addition to the thermal-orbital model in Chen and Nimmo (2016) and was found to play one of the most important roles in the lunar evolution. A resonance in the ocean flow of synchronous satellites between the obliquity tide and a Rossby-Hauritz wave leads to enhanced dissipation (Tyler, 2008). Chen et al. (2014) showed that obliquity tidal heating in oceans on synchronous satellites can often be stronger than that in the solid-body, so neglecting ocean tides risks drastically underestimating inclination damping.

We use the analytical expressions in Hay and Matsuyama (2019) to calculate obliquity and eccentricity tidal heating in the lunar magma ocean due to bottom drag.

These expressions include the effect of a rigid lid overlying the ocean, which is important as the magma ocean crystallizes and the crust thickens. The effect of pressure forcing on the ocean from the lid is included using pressure Love numbers (Matsuyama et al., 2018). We compute the pressure Love numbers using the propagator matrix method with the appropriate boundary conditions for pressure forcing (Matsuyama et al., 2018) and under the same assumptions described above for the tidal Love numbers at the tidal forcing frequency. In our baseline models, the bottom drag coefficient has the same value as for Earth's oceans, $c_D = 0.002$.

3.2.4 Magma ocean solidification

After the Moon-forming giant impact, the Moon would have had a global magma ocean 100–1000 km deep. We track the solidification of the magma ocean and growth of an overlying crust due to conductive cooling and allow for remelting due to tidal dissipation. The magma ocean lifetime depends chiefly on the thermal diffusivity, $\kappa = k/\rho_o C_p$, where C_p is the specific heat capacity of the magma ocean.

The lifetime of the lunar magma ocean is estimated from the span of ages inferred for crustal formation, 100-200 Myr (e.g., Elkins-Tanton et al., 2011; Maurice et al., 2020, and references therein), although there are surface ages with high uncertainties (Borg et al., 2015). Maurice et al. (2020) found that the last dregs of the lunar magma ocean solidified 100-180 Myr after the most reliably dated sample from the earliest flotation crust (Borg et al., 2011). A magma ocean lifetime of 100-200 Myr can be attained by using the thermal conductivity of anorthosite, $k = 1.5$ W m^{-1} K^{-1}

(Maurice et al., 2020).

Of a layer that solidifies in the magma ocean, approximately 80 per cent solidifies at the bottom of the ocean and 20 per cent floats to the crust (Snyder et al., 1992; Warren, 1986). Therefore, 20 per cent of the change in the ocean thickness goes to or comes from the Moon's crust. The rate of change for the magma ocean and crustal thicknesses, h and d, are as follows:

$$\rho_o L \frac{dh}{dt} = -\frac{k\,(T_a - T_0)}{d - \delta} + H_{\text{crust}} + H_{\text{ocean}} \tag{3.20}$$

$$\dot{d} = -\frac{1}{5}\frac{dh}{dt}, \tag{3.21}$$

where ρ_o is the magma ocean density, and L is the latent heat of fusion. The ocean heat flux is $H_{\text{ocean}} = \dot{E}_{\text{ocean}}/4\pi R^2$, where $\dot{E}_{\text{ocean}}$ is tidal dissipation in the subsurface lunar magma ocean calculated from Hay and Matsuyama (2019).

The depth of the magma ocean affects eccentricity tidal heating, but for small c_D, obliquity tidal heating is independent of ocean thickness (Hay and Matsuyama, 2019). The thickness of the crust affects solid-body tidal dissipation, and since we approximate the elastic lithosphere thickness by the crustal thickness, it also affects how well the Moon can maintain the lithospheric stresses of a fossil figure.

3.2.5 Summary

In summary, the thermal-orbital model evolves the lunar orbit in response to tidal dissipation in the Earth and in the lunar magma ocean and lower crust. The biggest unknowns are the early migration rate of the Moon away from the Earth and

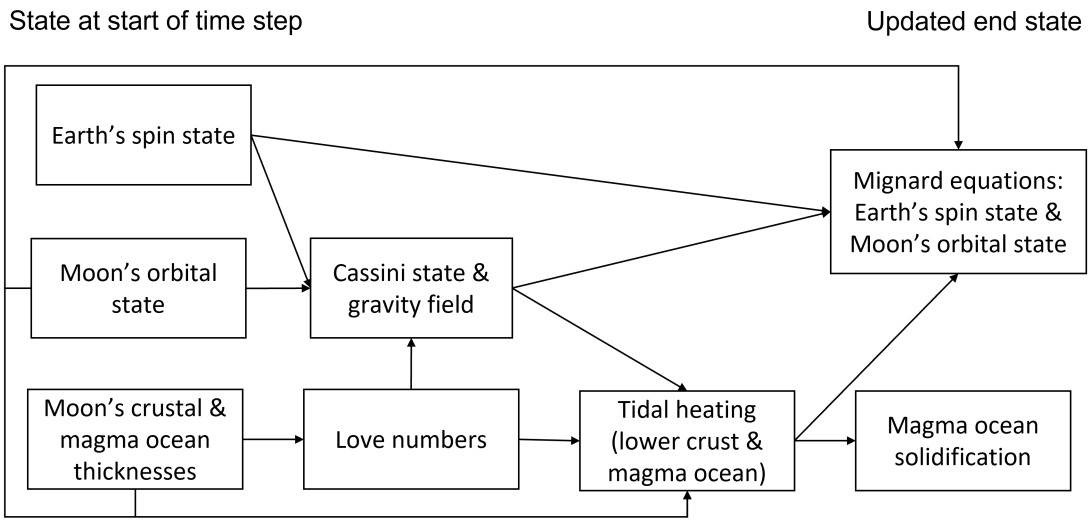

Figure 3.1: Block diagram of how the thermal and orbital processes relevant to the lunar inclination interact and depend on each other in each time step. The Earth's spin state, the Moon's orbital state, and the properties of the lunar crust all affect the Moon's Cassini state obliquity. Obliquity tidal heating in the solid-body and magma ocean then damp the inclination.

where the Moon's fossil figure freezes in. These quantities affect whether the magma ocean solidifies before the LPT and whether the CST occurs before the planetesimal population dies out. A block diagram of how all of the relevant processes affect each other is included in Figure 3.1.

We start the Moon at $a = 6.5R_E$, outside the evection and eviction resonances with a variable initial inclination to the Laplace plane, i_0. To test an early inclination, $i_0 = 12°$, a plausible value after proto-Moon disk resonances (Ward and Canup, 2000) or the eviction resonance (Touma and Wisdom, 1998). To test a late inclination, $i_0 = 0°$. To get the Earth approximately to its present-day state, the Earth's initial day is 5.6 hr, and its obliquity with respect to the Laplace plane is $I_0 = 8°$. For a 1000 km magma ocean after Moon formation, a flotation crust does not form until the ocean solidifies

to 200 km, so we set the initial ocean thickness as $h_0 = 200$ km and the initial crustal thickness as $d_0 = 1$ km. Tidal heating in the magma ocean is shut off at $h = 10$ km to account for non-uniform solidification of the global magma ocean.

3.3 Results

We tested three inclination excitation scenarios in the context of our thermal-orbital model and determined which configurations matched the present-day observations for the lunar inclination and degree-2 gravity field.

The first scenario that we tested is that the Moon acquired an inclination of 12° soon after Moon formation either through resonances between the proto-Moon and accretion disk (Ward and Canup, 2000) or from passage through the evection and eviction resonances (Touma and Wisdom, 1998).

The second scenario from Ćuk et al. (2016b) is that post-Moon-forming giant impact, the Earth-Moon system had a much higher angular momentum and obliquity ($60 - 80°$) than it has now. The high angular momentum would allow for mixing of the proto-Earth and impactor material and explain the isotopic similarities between the Earth and Moon. Tremaine et al. (2009) found that for planets with high obliquity, a satellite's LPT, where the Sun's gravitational effect on the precession of the lunar orbit outweighs that from the planet's oblateness, can destabilize its orbit and add significant inclination and eccentricity. In Ćuk et al. (2016b, 2021), solar perturbations and resonances during the Moon's LPT drain excess angular momentum, diminish the

Earth's large obliquity, and excite the lunar inclination to $> 30°$.

The third scenario taken from Pahlevan and Morbidelli (2015) is that planetesimals from the inner solar system would have swept by the Earth-Moon system. A few bodies totalling 0.015 Earth mass would have collided with the Earth, being part of its late accretion. As the planetesimals swept through, collisionless encounters with the Moon imparted momentum and stochastically increased the Moon's inclination and eccentricity until the population died out around 140 Myr after Moon formation.

Fig. 3.2 shows example semi-major axis and inclination evolutions for a general early excitation (< 1 Myr) and the two late excitation scenarios (> 1 Myr). We varied the early migration rate of the Moon which is set by $(k_{2,E}\Delta t)_0$. To match the present-day degree-2 gravity field, each simulation has a different semi-major axis where the fossil figure freezes in, a^*. Fig. 3.2a shows the evolution for an early inclination excitation with an initial inclination to the Laplace plane of $i_0 = 12°$. In no cases does the inclination survive to the present day. Fig. 3.2b approximates a 30° inclination excitation at the LPT, which for the angular momentum of the Earth-Moon system in our simulations happens at $a \sim 16R_E$. In this case the inclination survives if the outwards motion is sufficiently slow ($(k_{2,E}\Delta t)_0 \leq 0.1$ s) that the LPT occurs after the magma ocean has solidified. Fig. 3.2c approximates perturbations to the lunar orbit from close encounters with planetesimals by having a set of four inclination kicks of 4° at 35, 70, 105, and 140 Myr. In this case an inclination can survive if outwards motion is sufficiently rapid that the CST occurs prior to the disappearance of the planetesimals. While Figs. 3.2b, c represent severe simplifications compared to the original works, they allow us to focus on

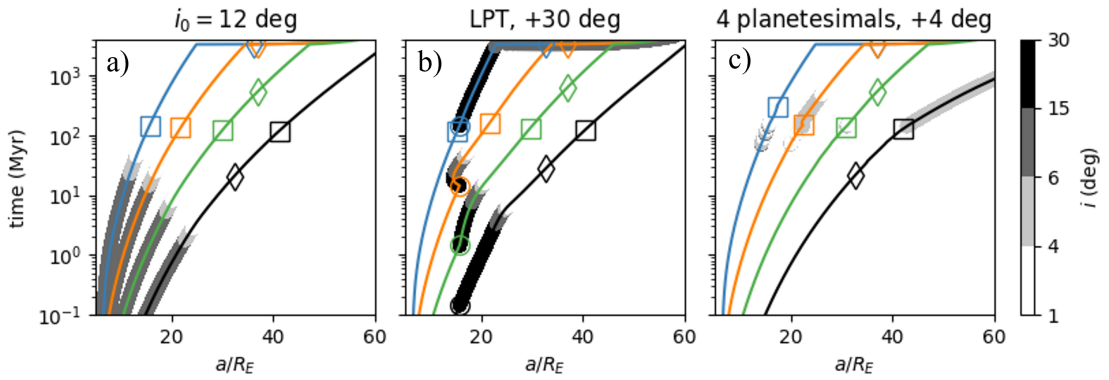

Figure 3.2: Three example inclination excitation scenarios. a) an early excitation with $i_0 = 12°$ b) a 30° excitation at the LPT c) four planetesimals adding 4° of inclination at 35, 70, 105, and 140 Myr. The inclination evolution is shown in the greyscale contours, and the different lines are for four $(k_{2,E}\Delta t)_0$, 0.1 s (blue), 1 s (orange), 10 s (green), 100 s (black). Squares mark the lunar magma ocean solidification, diamonds the CST, and circles the LPT. The thermal diffusivity of the magma ocean is $\kappa = 5 \times 10^{-7} m^2 s^{-1}$, and it solidifies in 100-200 Myr. Once the magma ocean is solidified, the solid-body tidal dissipation is calculated using $k_2/Q = 6 \times 10^{-4}$, the present value. The knee in the graphs at 3.25 Gyr is when $k_{2,E}\Delta t$ steps to the present value of 180 s. Under no condition does an early inclination survive. In panel (b), for $(k_{2,E}\Delta t)_0 \leq 0.1$ s, the magma ocean solidifies prior to the LPT, limiting ocean obliquity tidal heating and leaving a lasting inclination. In panel (c), for $(k_{2,E}\Delta t)_0 \geq 40$ s, the CST occurs and the magma ocean solidifies prior to 140 Myr when the planetesimal population dies down, allowing planetesimal perturbations to leave a lasting inclination.

the magnitude of the inclination excitation and whether it could survive tidal dissipation. As discussed more in-depth below, obliquity tidal dissipation is so strong that any early inclination damps, and the only way for a late inclination to survive is if the excitation occurs after strong ocean obliquity tidal heating ends.

3.3.1 Early inclination excitation

Fig. 3.2a shows that an early inclination cannot survive inclination damping due to obliquity tidal heating in the magma ocean and solid-body. Obliquity tidal

dissipation in the magma ocean could be weaker for several reasons. The first is that the magma ocean could have been short-lived, although there is little evidence of this and would be contradictory to the lunar chronology data (e.g., Maurice et al., 2020). The second is that thickness variations in the overlying flotation crust could disrupt the resonance between the obliquity tide and the Rossby-Haurwitz wave (Rovira-Navarro et al., 2020). The final reason is that the strength of the tidal heating depends on the bottom drag coefficient, which for Earth is $c_D = 0.002$ and follows a scaling law relationship with the Reynolds number (Fan et al., 2019). The Reynolds number of the lunar magma ocean is calculated using the flow speed from Chen et al. (2014) to be self-consistent with our tidal heating model and the viscosity of basalt, $\eta = 1000$ Pa s. The scaling law in Fan et al. (2019) produces values of c_D in the lunar magma ocean in the range of 0.001-0.004, so we use $c_D = 0.002$ for our baseline model.

Even if there were no ocean obliquity tidal heating, solid-body dissipation would still have to be weaker on average than at present to not damp an early inclination. Fig. 3.3 shows the a^* and average k_2/Q over the past needed to allow an early inclination of 12° to survive and the present-day degree-2 gravity field to be reproduced. In this case, there are no ocean obliquity tides and the solid-body tides follow the visco-elastic model in Sec.3.2.3.1 until solidification is complete in 100-200 Myr. The average k_2/Q in the past would have to be $10^{-5} - 10^{-4}$ for an early inclination of 12° to survive to the present-day while simultaneously satisfying the gravity constraints, which implies that the early Moon would have to be less dissipative than it is now. This is an upper bound on the needed average k_2/Q because if there were any ocean obliquity tidal heating, the

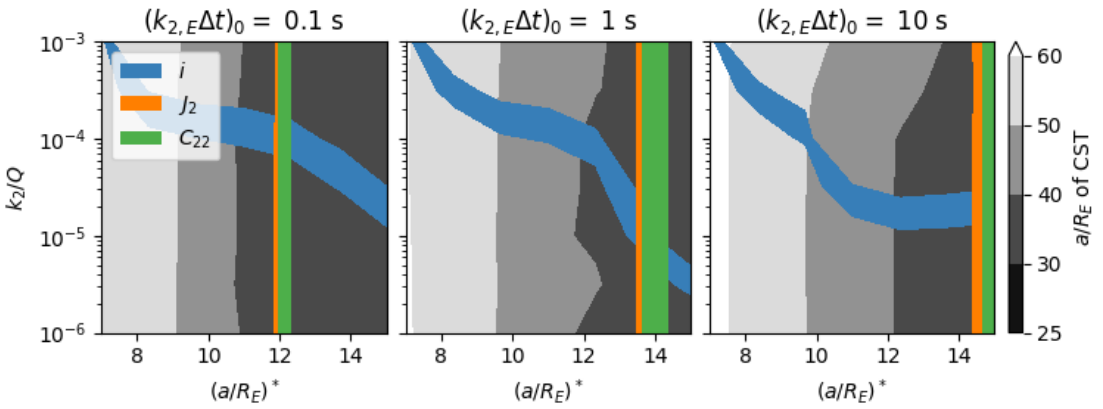

Figure 3.3: Parameters for which an early inclination survives. Including only solid-body and no ocean obliquity tides, for three different initial migration rates set by $(k_{2,E}\Delta t)_0$, the colored bands are the set of k_2/Q and a^* that match the present-day inclination (blue), J_2 (orange), and C_{22} (green) to within 10 per cent. The J_2 and C_{22} observations come from Matsuyama et al. (2021) and include the tidal-rotational and fossil figure components (excludes contributions from the South Pole-Aitken basin). The gray contours in the background show where the CST occurred in the model runs. To match the present-day J_2 and C_{22} observations, the CST happened between 32 and 38 Earth radii. On average in the past, k_2/Q would have to be at least one to two orders of magnitude lower than at present ($k_2/Q = 6 \times 10^{-4}$) for an early inclination to survive to the present-day.

solid-body component would have to be weaker. A warmer, less rigid Moon is expected to be more dissipative, so we conclude that there are no conditions under which tidal dissipation can be weak enough to allow an early inclination of 12° to survive.

3.3.2 Late inclination excitation

Obliquity tidal heating in the magma ocean and solid-body will damp an early inclination, so the only explanation for the present-day inclination is a late excitation mechanism that takes place after the period of strong ocean heating is over. Fig. 3.4 shows the relative timings of the LPT, CST, and the solidification of the lunar magma

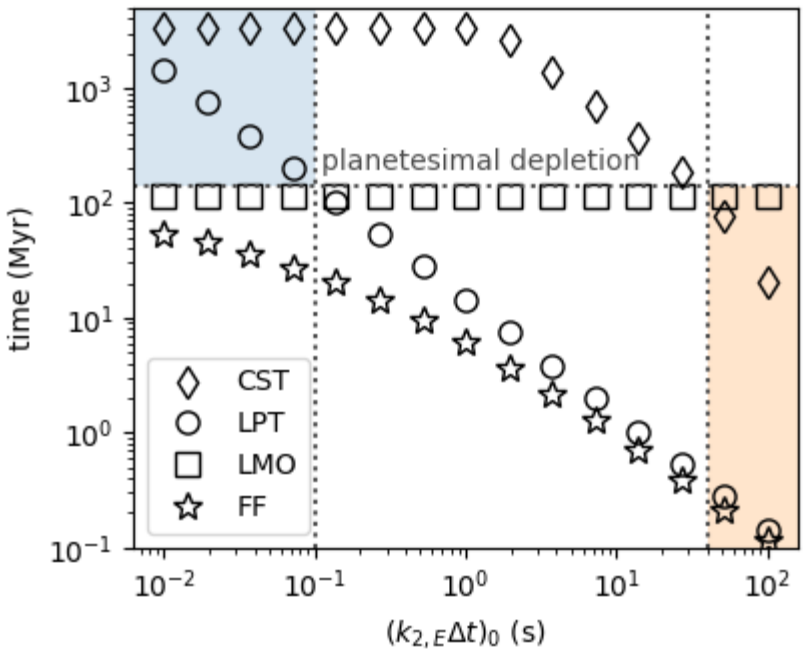

Figure 3.4: The timings of the fossil figure freeze-in (FF, star), the lunar magma ocean solidification (LMO, square), the LPT (circle), and the CST (diamond) as a function of $(k_{2,E}\Delta t)_0$. Each fossil figure semi-major axis is chosen for that run to match the J_2 and C_{22} observations. If the LPT at $a \sim 16R_E$ is responsible for exciting the lunar inclination, then $(k_{2,E}\Delta t)_0 \leq 0.1$ s to reach this point after the magma ocean solidifies in 100-200 Myr (represented by the blue shaded region in the upper left). If the planetesimal population is responsible, then $(k_{2,E}\Delta t)_0 \geq 40$ s to pass the CST and to solidify the magma ocean prior to the depletion of the planetesimals by 140 Myr (represented by the orange shaded region in the lower right).

ocean as a function of $(k_{2,E}\Delta t)_0$ in order to determine what migration rates are needed for each of the late excitation mechanisms to be viable. For each $(k_{2,E}\Delta t)_0$, the fossil figure is established at a different semi-major axis so that the present-day degree-2 gravity field is reproduced. The blue shaded region in the upper left shows when the LPT postdates solidification of the magma ocean. The orange shaded region in the lower right shows when both the CST and the magma ocean solidification precede depletion of the planetesimal population at 140 Myr. From Fig. 3.4, there is a maximum speed limit for instabilities at the LPT and a minimum speed limit for perturbations from plantesimals to be the source of the lunar inclination.

Instabilities at the LPT can only leave a lasting inclination if it occurs after the magma ocean solidifies otherwise ocean obliquity tidal heating damps the excitation in a span of 10's Myr (see Fig. 3.2b). The LPT occurs when solar effects on the precession of the Moon's longitude of the ascending node outweigh effects from the Earth's oblateness. Quantitatively, this is when the second term in Eq. 3.2 surpasses the first in magnitude. In our simulations, the LPT occurs consistently at $a \sim 16R_E$ because we do not vary the initial angular momentum of the Earth-Moon system set by the initial lunar semi-major axis and spin rate of the Earth. The Earth's spin frequency evolution affects the Earth's oblateness quantified by the degree-2 gravity coefficient $J_{2,E}$. For the Moon to take at least 100 Myr to get to the LPT at $a \sim 16R_E$, there is a maximum speed limit, which translates to $(k_{2,E}\Delta t)_0 \leq 0.1$ s (see Fig. 3.4). Then to match the present-day degree-2 gravity observations in Matsuyama et al. (2021), a fossil figure freezes in at $a^* \leq 12R_E$ (see Fig. 3.3). In reality, for the LPT to be destabilizing, the initial angular momentum

of the Earth-Moon system would have to be higher than in our simulations (Ćuk et al., 2016b). This would push the LPT out to 17-22 R_E (Ćuk et al., 2021), raising the upper bound on the Moon's initial migration rate.

Collisionless encounters with planetesimals can only leave a lasting mark on the inclination if the magma ocean solidifies and the CST occurs before the depletion of the planetesimal population at $\sim$ 140 Myr after Moon formation (Pahlevan and Morbidelli, 2015). The CST marks when the obliquity flips from negative to positive in the simulation (see Section 3.2.2). Fig. 3.2c shows that because the planetesimal kicks are smaller than that from the LPT, even solid-body obliquity tides during the CST could damp out any planetesimal inclination excitation. Counterintuitively, planetesimal kicks too large early on make it harder for later kicks to survive because the tidal heating from the increased inclination and obliquity delays the magma ocean solidification and prolongs strong inclination damping. There is a minimum speed limit for the Moon to pass the CST before 140 Myr, which places the constraint $(k_{2,E}\Delta t)_0 \geq 40$ s (see Fig. 3.4). A fossil figure freezes in at $a^* \sim 15R_E$ to match the present-day gravity field observations (see Fig. 3.3).

Predicting which scenario is responsible for the lunar inclination depends largely on the $(k_{2,E}\Delta t)_0$ of the early Earth. Zahnle et al. (2015) found that after the Moon-forming giant impact, the Earth's atmosphere cooled slowly enough to limit dissipation in the interior for the first 2-10 Myr. They predict $Q \gtrsim 10^4$, which by the tidal relation $1/Q \sim 2\Omega\Delta t$, corresponds to $(\Delta t)_0 \lesssim 0.2$ s assuming the 5.6 hr initial Earth length of day used in this work. For a warmer young Earth, $k_{2,E}$ would be of order unity yielding

$(k_{2,E}\Delta t)_0 \lesssim 0.2$ s. This constraint is consistent with the LPT excitation mechanism. Collisionless encounters with planetesimals could only impart inclination to a slowly receding Moon if it were less dissipative in the past than at present (see Sec. 3.3.1 for a discussion on the ways to decrease tidal dissipation in the Moon). A further difficulty is that collisionless encounters have a stronger effect at greater Earth-Moon distances, so slow lunar recession keeps the Moon at shorter distances while the planetesimal population depletes, exciting the inclination less (Pahlevan and Morbidelli, 2015). On the whole, therefore, we favour an early slow outwards migration and inclination excitation via instabilities at the LPT.

An example evolution of the LPT exciting the lunar inclination is shown in Fig. 3.5 for $(k_{2,E}\Delta t)_0 = 0.1$ s. The LPT occurs at $a \sim 16R_E$ (140 Myr into the simulation) at which point the inclination is instantaneously increased to 30° to approximate the results of Ćuk et al. (2016b, 2021). Because the magma ocean solidifies earlier at 115 Myr, only solid-body obliquity tidal heating damps the inclination. We use a constant $k_2/Q = 7.5 \times 10^{-4}$ that is meant to be an average over the past since the present value is lower and the past value would have been higher. A fossil figure freezes in at $a^* = 12R_E$ (23 Myr into the simulation), which pushes the CST out to $33R_E$ (3.3 Gyr into the simulation) compared to $\sim 28R_E$ had there been no fossil component. The degree-2 gravity coefficients decay as the Moon migrates away from the Earth because the rotation slows and the tidal pull from the Earth weakens. At 3.25 Gyr (1.25 Ga) $k_{2,E}\Delta t$ steps from the initial to the present value to account for the resonant tidal dissipation in the Earth's oceans at the present-day while also getting the Moon to 60 R_E

by the end of the simulation. This causes a qualitative change in the semi-major axis evolution at $\sim 23R_E$ which has a ripple effect on the inclination, obliquity, and tidal heating evolution as well. The knee that this produces in the inclination evolution is by no means critical to the survival of the inclination; it simply reflects the fact that it takes the Moon 3 Gyr in this simulation to go from the LPT at $16R_E$ to $23R_E$ and ~ 1 Gyr to go from $23R_E$ to $60R_E$. Solid-body tidal heating decreases with distance and increases with obliquity at the CST, but the net effect is that more inclination will damp in the first 3 Gyr than in the last 1 Gyr.

3.4 Discussion

The goal of this work is to build on past thermal-orbital models to constrain the evolution of the lunar inclination. We highlight how solid-body tides affect inclination damping, what problems remain for the eccentricity evolution, and how the lunar figure model from Matsuyama et al. (2021) allows us to pinpoint when the fossil figure was established and when the CST occurred.

3.4.1 Solid-body tides

A main difference between this work and Chen and Nimmo (2016) is that we include solid-body tidal heating for both inclination and eccentricity damping. In Sec. 3.3.1 we show that without ocean tidal heating, solid-body tides can damp away an early inclination of 12°, and in Sec. 3.3.2 we show that solid-body tidal heating during the CST could damp away excitations from plantesimals. This is even despite

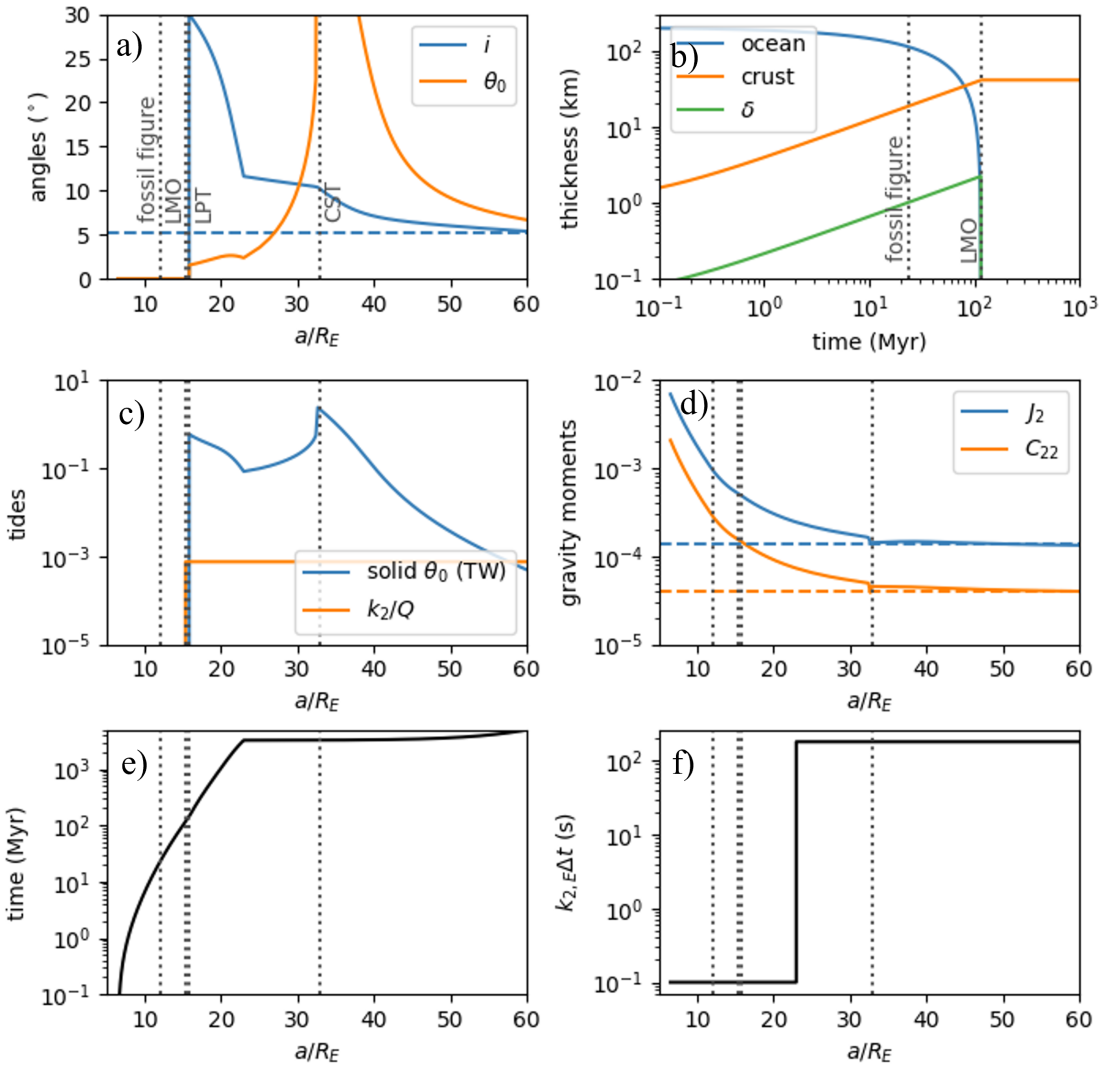

Figure 3.5: Different aspects of an example thermal-orbital evolution. The LPT excites the inclination to 30° and the degree-2 gravity observations (Matsuyama et al., 2021) are reproduced, including a) the inclination and magnitude of the obliquity (negative before the CST and positive after) b) the magma ocean solidification c) solid-body obliquity tidal heating and k_2/Q d) the degree-2 gravity coefficients e) the semi-major axis and f) $k_{2,E}\Delta t$. The magma ocean crystallizes within 115 Myr ($\kappa = 5 \times 10^{-7}$ m^2/s) at $a = 15$ R_E for $(k_{2,E}\Delta t)_0 = 0.1$ s. A fossil figure freezes in at $a^* = 12R_E$, which pushes the CST out to $\sim 33R_E$ at 3.3 Gyr. The bottom drag coefficient is the value for oceans on Earth, $c_D = 0.002$. Vertical dotted lines mark the fossil figure freezing, magma ocean solidification (LMO), LPT, and CST. The horizontal dashed lines are the observed present-day values for comparison with their solid-color model counterparts.

the fact that obliquity tides are stronger in the oceans of synchronous satellites than in the solid-body (e.g., Chen et al., 2014). The results are in line with Ćuk et al. (2016b) who found that the initial inclination of the Moon had to be $> 50^\circ$ to decay to its present value assuming the Moon's current solid-body dissipative properties. The lunar evolution adage that the Moon had to begin with twice the inclination it has now (e.g., Goldreich, 1966) neglected the importance of solid-body obliquity tides during the Moon's CST.

The opposite is true for eccentricity tides, which are typically stronger in the solid-body of synchronous satellites than in global oceans (e.g., Chen et al., 2014), so solid-body tidal heating is the main driver of eccentricity damping. What we find is that given $k_2/Q = 6 \times 10^{-4}$ and the fact that solid-body tidal heating is stronger at smaller semi-major axis, slow lunar recession causes any initial eccentricity or excitation at the LPT to damp away completely. With fast recession and arbitrary eccentricity kicks from planetesimals, an eccentricity can survive damping and even increase due to tides on the Earth. Future work on the Moon's orbital evolution will have to focus on simultaneously recovering the Moon's inclination and eccentricity since they may require different explanations. In particular, while we favour the LPT for the Moon's inclination, collisionless planetesimal encounters may well provide an explanation for its eccentricity.

3.4.2 Fossil figure

The size of the fossil figure observed at the present-day depends on two factors, the strength of the elastic lithosphere and the strength of the tidal-rotational potential when it was established (see Eqs. 3.7 and 3.8). Striking a balance between the two means considering the relative timing of the solidification of the magma ocean with respect to the semi-major axis migration. Fig. 3.6 shows the theoretical relationship between the elastic lithosphere thickness, T_e^*, and the semi-major axis, a^*, when the fossil figure is established in order to produce the fossil figure size in Matsuyama et al. (2021). The more resistant the lithosphere is to deformation, the stronger the tidal-rotational potential has to be (large T_e^*, small a^*). The more easily the lithosphere deforms, the weaker the tidal-rotational potential can be (small T_e^*, larger a^*). To achieve a thick elastic lithosphere at a small distance, the Moon must recede slowly due to a small $(k_{2,E}\Delta t)_0$. To achieve a thin elastic lithosphere at a larger distance, the Moon must receded quickly due to a large $(k_{2,E}\Delta t)_0$.

Fig. 3.6 shows that there is a theoretical upper bound of $16R_E$ for freezing in the fossil figure, which coincides with an elastic lithosphere thickness of 1 km. For $(k_{2,E}\Delta t)_0 \leq 0.1$ s consistent with the LPT exciting the lunar inclination (blue dot), the fossil figure freezes in at $\leq 12R_E$. These predictions are noteworthy because it would mean that the fossil figure predates both the LPT at $\sim 16R_E$ and the CST at $\sim 33R_E$. Thus, an important conclusion from our work is that neither event could have heated the Moon strongly enough to reset the lunar figure. More sophisticated coupled thermal-

orbital models could test this conclusion. Furthermore, for the $(k_{2,E}\Delta t)_0$ sampled in Fig. 3.4, the fossil figure always freezes in prior to 100 Myr after Moon formation. With more consensus on the ages of the Moon and the South Pole-Aitken Basin (SPA), more could be said about the relative timing between the fossil figure and SPA.

There are a few effects that we have ignored for simplicity that could lead to over- and under-estimating the fossil figure contributions to the degree-2 gravity field. In this work, we approximate the elastic lithosphere thickness as being the total crustal thickness when in reality it is smaller. The consequence is that our simulations potentially freeze in the fossil figure before the elastic lithosphere has reached its optimal strength, and so the curve in Fig. 3.6 should be pushed to the right to larger semi-major axes to correct for this. Another factor that could lead to overestimating the fossil figure is that we neglect strengthening of the elastic lithosphere after the magma ocean has completely solidified. For reference, our simulations have a maximum of $T_e = 45$ km, which corresponds to $k_2^\infty = 0.993$ which becomes fixed once the magma ocean solidifies. Strengthening the elastic lithosphere lowers the long-term Love numbers and causes the fossil figure contribution to grow with time. A way that our model underestimates the fossil figure contribution is that it freezes in the fossil component instantaneously and does not account for later viscous relaxation (c.f., Qin et al., 2018). For a long-term formation of the fossil figure as in Qin et al. (2018), as long as the bulk of the fossil figure is established prior to the CST, the effects on our results would be limited. To freeze in a larger fossil figure than that observed today in order for the stresses to viscously relax over time would push the black curve in Fig. 3.6 to the lower left, meaning that the fossil

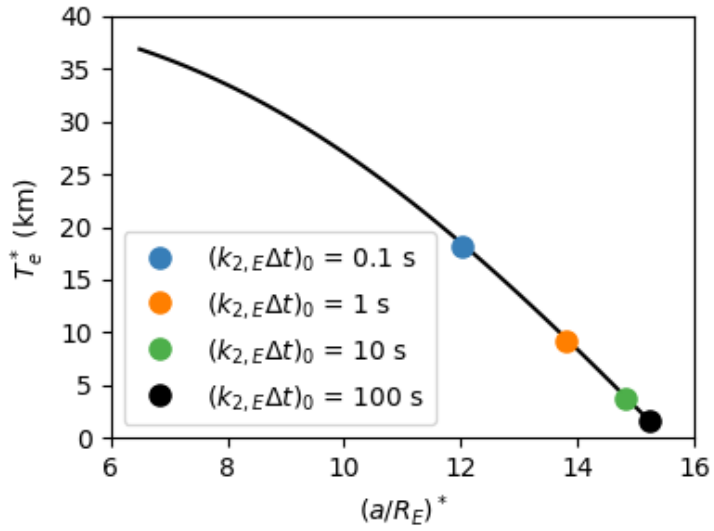

Figure 3.6: The theoretical relationship between the elastic lithosphere thickness, T_e^*, and the semi-major axis, a^*, when the fossil figure is established to reproduce the present-day lunar fossil figure (Matsuyama et al., 2021). Successful simulations with different $(k_{2,E}\Delta t)_0$ are plotted as circles; the blue circle is the model run shown in Fig. 3.5. There is a balance between the strength of the elastic lithosphere (depends on $k_2^{\infty *}$ or T_e^* by proxy) and the tidal-rotational potential (depends on a^* and assumes negligible obliquity and eccentricity). If the Moon recedes slowly, a thick lithosphere coincides with a short distance, and if the Moon recedes quickly, a thin lithosphere coincides with a large distance. There is an upper bound of $a^* = 16R_E$, which corresponds to an elastic lithosphere thickness of 1 km ($k_2^{\infty *} = 1.359$). The results assume that the magma ocean did not form a permanent flotation crust until 6.5 R_E.

figure would have to be established at smaller semi-major axis and elastic lithosphere thickness.

In all of the simulations that reproduce the degree-2 gravity observations, the CST happens in the range of $\sim 32 - 38R_E$, which is consistent with the $34R_E$ found in Matsuyama et al. (2021). We show in Sec. 3.3.2 that without a fossil figure, the CST would happen at $\sim 28R_E$. The observation that a fossil bulge affects where the CST occurs was also observed by Siegler et al. (2011) in addition to Matsuyama et al.

(2021). In Siegler et al. (2011), the lunar figure has a combination of hydrostatic and fossil components, although in what proportion is not stated. Their CST happens at $\sim 30R_E$. This is compared to $\sim 28R_E$ for the absent fossil figure case in this work and to $33R_E$ with a fossil figure. Ward (1975a) also calculated a CST at $\sim 34R_E$ but that was assuming the present-day lunar figure and orbit. In reality, the figure and orbit evolved significantly enough in the past to affect the location of the CST, so it is a coincidence that Ward (1975a) is consistent with our results.

3.5 Conclusion and Future Work

We conclude that the most likely source of the lunar inclination is the LPT at $a = 16R_E$ (Ćuk et al., 2016b, 2021), and for this point to be reached after the solidification of the magma ocean in > 100 Myr, the Moon recedes slowly from an early Earth with $(k_{2,E}\Delta t)_0 \leq 0.1$ s. The other possibility is that collisionless encounters with planetesimals in the first 140 Myr after Moon formation (Pahlevan and Morbidelli, 2015) excite the lunar inclination, which requires quickly passing the CST and solidfying the magma ocean before this time with $(k_{2,E}\Delta t)_0 \geq 40$ s. A large $(k_{2,E}\Delta t)_0$ is inconsistent with a weakly dissipative Earth soon after Moon formation (Zahnle et al., 2015). For slow initial recession from the Earth, the lunar fossil figure was established at $\lesssim 12R_E$. The eccentricity and obliquity during this time are small compared to other fossil figure solutions that require a large eccentricity or non-synchronous rotation. Our fossil figure range is consistent with that found in Matsuyama et al. (2021).

Future work on the question of how the Moon got its inclination and where the fossil figure was established will entail including the conditions necessary for the LPT to excite the lunar inclination as in Ćuk et al. (2016b, 2021), the effect of topographic variations on ocean tidal heating, and the early tidal state of the Earth. Since the location of the LPT is dependent on the angular momentum of the early Earth-Moon system, future work should explore the effects of a high angular momentum starting point on the predicted tidal-orbital lunar evolution. Our ocean tides model assumes a uniform ocean thickness with no crustal variations. To account for some non-uniform ocean solidification, we turn off tidal heating in the ocean when the thickness reaches 10 km. Rovira-Navarro et al. (2020) showed that the effects of ocean thickness variations on tidal heating are much more complicated and have the potential to limit tidal heating considerably. In future work, we will see how potential variations in the ocean thickness can affect the obliquity tide flow.

Modelling the thermal-orbital evolution of the Moon would be improved with a better understanding of the tidal state of the early Earth. Our simple parameterization of $k_{2,E}\Delta t$ recovers the correct present-day lunar semi-major axis and Earth Q but is *ad hoc* and could in principle be improved if we had sufficient understanding of ocean dynamics throughout Earth history. The early tidal state of the Earth is key to ruling out different lunar evolution scenarios in our coupled thermal-orbital model.

Table 3.1: Physical parameters used in the thermal-orbital model

Symbol	Parameter	Value
G	Gravitational constant	6.674×10^{-11} m^3 s^{-2} kg^{-1}
M_S	Mass of the Sun	2×10^{30} kg
M_E	Mass of the Earth	5.9723×10^{24} kg
R_E	Radius of the Earth	6378 km
a_E	Semi-major axis of the Earth	1.496×10^{11} m
$k_{2,E}$	k_2 Love number of the Earth	0.97
α	Normalized moment of inertia of the Earth	0.33
m	Mass of the Moon	7.25×10^{22} kg
R	Radius of the Moon	1737 km
ρ_o	Density of the magma ocean	3000 kg m^{-3}
C_p	Specific heat capacity of magma ocean	1256 J kg^{-1} K^{-1}
T_m	Temperature of magma ocean	1200 K
T_0	Temperature of the surface	280 K
T_a	Temperature of layer interface in crust	1150 K
L	Latent heat of fusion	5×10^5 J kg^{-1}
c_D	Bottom drag coefficient	0.002
η_o	Viscosity of magma ocean	1000 Pa s
μ	Rigidity of the crust	30 GPa
η	Viscosity of the crust	10^{19} Pa s
f	Spatial variable	1

Acknowledgements

We thank two anonymous reviewers for their thorough comments and suggestions which have significantly improved this manuscript. I. M. was supported by the National Aeronautics and Space Administration (NASA) under grant No. 80NSSC20K0334 issued through the NASA Emerging Worlds program. This material is based upon work supported by the National Science Foundation Graduate Research Fellowship under Grant No. DGE-1842400.

Chapter 4

Titan's spin state as a constraint on tidal dissipation

A slightly modified version of this chapter has been submitted to the journal Science Advances.

Abstract

Tidal dissipation in satellites affects their orbital and rotational evolution and their ability to maintain subsurface oceans. However, the rate of dissipation, as parameterized by the quantity k_2/Q, is hard to measure and, among satellites, is only known for the Moon and Io. Here we show that the measured departure of Saturn's largest moon Titan from its expected rotation state can be used to infer Titan's k_2/Q. Under the assumption that torques at the ice shell-ocean interface are negligible, we infer a k_2/Q for Titan of 0.12 ± 0.027, two orders of magnitude larger than the Moon, and a

dissipation factor $Q \approx 5$. This surprisingly high dissipation rate implies that Titan's orbital eccentricity is damping rapidly, consistent with an excitation within the last ~ 100 Myr. It also suggests an interior with a low effective viscosity and an ice shell that is either convective or thinner than the canonical ~ 100 km. The predicted phase lag of Titan's tidal response could be measured by the forthcoming Dragonfly lander, and the JUICE spacecraft should be able to use our approach to determine Ganymede's k_2/Q.

4.1 Introduction

Satellites experience tides raised by their planets, with the tidal Love number k_2 describing the magnitude of the tidal response (Love, 1927). The tidal quality factor Q quantifies the lag of the tidal response, and the combined quantity k_2/Q determines the rate at which tidal energy is dissipated inside the satellite (MacDonald, 1964; Peale and Cassen, 1978). Tidal dissipation in the satellite controls how rapidly its orbit shrinks, circularizes, and becomes planar (Chyba et al., 1989). Measurements of k_2 and k_2/Q also help with inferences about the satellite's interior structure, such as whether it contains a subsurface ocean (Iess et al., 2012; Bierson and Nimmo, 2016). However, despite its importance in understanding a satellite's orbital evolution and interior, k_2/Q is hard to measure.

The Moon and Io are the only two satellites with a measured k_2/Q. For the Moon, k_2/Q has been determined using a combination of laser ranging and spacecraft

tracking (Williams and Boggs, 2015) and for Io, k_2/Q comes from astrometric observations of the change in semi-major axis and eccentricity (Lainey et al., 2009). The Cassini spacecraft performed over 100 flybys of Titan, collecting data on Titan's gravitational field and rotational state (Stiles et al., 2008; Iess et al., 2010). Notably, Cassini measured Titan's k_2, making it only the second satellite after the Moon whose tidal response has been measured (Iess et al., 2012; Durante et al., 2019). However, existing studies either derived bounds on k_2/Q that were consistent with zero (Durante et al., 2019; Lainey et al., 2020), or did not solve for it (Jacobson, 2022). We use existing measurements of Titan's rotation state to infer the value of k_2/Q, concluding that Titan experiences a high rate of tidal dissipation at the present day.

Our approach uses the measured angular offset in Titan's spin axis to quantify energy dissipation. The equilibrium spin axis of a satellite is called a Cassini state after G.D. Cassini documented characteristics of the spin state of the Moon (Colombo, 1966). In a Cassini state, the spin axis and orbit normal both precess about the normal to the Laplace plane (defined as the average orbital plane) at the same rate and with the same or opposite phase (Colombo, 1966; Peale, 1969). The geometry of this configuration is such that during the precession cycle, all three vectors lie in the same plane, which we refer to as the Cassini plane (see Fig. 4.1). In the presence of dissipative torques, Cassini states are the expected terminus of spin evolution (Goldreich and Peale, 1970; Peale, 1974; Ward, 1975b).

Although dissipation brings the system towards equilibrium, it also causes the end spin state to be offset from the Cassini plane meaning that the planar configuration

is never quite reached (Yoder, 1981; Dickey et al., 1994). The magnitude of a body's Cassini plane offset is connected to the total amount of dissipation in the interior, including tidal dissipation. The only bodies in the solar system that are confirmed to be in a Cassini state are the Moon (Yoder, 1981; Dickey et al., 1994; Williams et al., 2014), Titan (Stiles et al., 2008; Baland et al., 2011), and Mercury (Stark et al., 2015), and all three have non-zero Cassini plane offsets. Fits to the lunar laser ranging data are able to distinguish between two distinct sources of dissipation in the Moon: tides and differential rotation between the solid mantle and fluid core (Williams et al., 2001). We argue that the flattening of Titan's ice shell is sufficiently large that there should be no differential rotation between the ice shell and subsurface ocean, meaning tides are likely the dominant source of dissipation today.

The rest of this manuscript is organized as follows: We present an analytical expression for the Cassini plane offset as a function of tidal and core-mantle boundary dissipation. We corroborate our expression with observations of the Moon's Cassini plane offset. We next apply the theory to determine Titan's k_2/Q, which has not been done before and discuss the implications for its tidal-orbital history. We end with implications for other satellites in our solar system, including Io and Ganymede.

4.2 Methods

In this work, we relate dissipative torques in a body to the magnitude of the Cassini plane offset following the approaches of Gladman et al. (1996) and Williams

et al. (2001). Many other authors have investigated Cassini state dynamics, and a non-comprehensive list of useful references include Peale (1969), Goldreich and Peale (1970), Ward (1975b), Organowski and Dumberry (2020), and Baland et al. (2014).

4.2.1 Spin dynamics without dissipation

A satellite's spin axis precesses about its orbit normal because of torques that the planet exerts on its permanent triaxial figure. At the same time, the satellite's orbit plane precesses due to torques from the planet's oblateness, the Sun, and other perturbing bodies such as neighboring satellites. The average orbit plane, the Laplace plane, lies between the planet's equator and the planet's orbit plane. Assuming uniform precession at one frequency, the orbit normal precesses about the Laplace plane normal at a rate (e.g., Colombo, 1966; Bills and Nimmo, 2011):

$$\frac{d\hat{n}}{dt} = \dot{\Omega}(\hat{n} \times \hat{k}) \tag{4.1}$$

Where $\hat{n}$ is the orbit normal, $\hat{k}$ is the normal to the Laplace plane, and $\dot{\Omega}$ is the precession of the longitude of the ascending node of the orbit plane on the Laplace plane.

In the reference frame of the precessing orbit with $\hat{n}$ along the z-axis, the orbit-averaged rate of change of the spin axis of a triaxial solid body in a circular orbit is (e.g., Colombo, 1966; Bills and Nimmo, 2011):

$$\frac{d\hat{s}}{dt}|_{rot} = \frac{3}{2}\frac{n^2}{c\omega}\left[(J_2 + C_{22})(\hat{s} \cdot \hat{n}) + C_{22}\right](\hat{s} \times \hat{n}) + \dot{\Omega}(\hat{s} \times \hat{k}) \tag{4.2}$$

where $\hat{s}$ is the spin axis unit vector, J_2 and C_{22} are the degree-2 gravity coefficients, c is the normalized polar moment of inertia, n is the orbital mean motion, and ω is the

spin angular velocity.

We define $\hat{n} = (0, 0, 1)$, $\hat{s} = (s_x, s_y, s_z) = (\sin\theta\cos\phi, \sin\theta\sin\phi, \cos\theta)$, and $\hat{k} = (\sin i, 0 \cos i)$. The obliquity, θ, is the angle between the spin axis and orbit normal, ϕ is the longitude of the ascending node of the equator plane on the orbit plane as measured from the y-axis, and i is the inclination of the orbit to the Laplace plane (see Fig. 4.1). Because the orbit precesses about the Laplace plane, the spin axis's net motion is also to precess about the Laplace plane. It is convenient to set up the spin geometry in this way because non-zero values of ϕ are diagnostic of dissipation in the satellite, whereas θ is usually weakly affected and so cannot be used alone to quantify the total amount of dissipation.

The system occupies what is known as a Cassini state (e.g., Colombo, 1966) when the spin axis and orbit normal have the same period of precession about the Laplace plane normal, which can only happen for specific values of the obliquity. In the absence of tidal dissipation, the Cassini state obliquity satisfies the following standard relation (e.g., Peale, 1969; Bills and Nimmo, 2011), which results from the steady-state solution to the y-component of Eq. 4.2:

$$\frac{3}{2}\frac{n^2}{c\omega}\left[(J_2 + C_{22})\cos\theta + C_{22}\right]\sin\theta = \dot{\Omega}\sin(i - \theta) \tag{4.3}$$

Similarly, a requirement for $ds_x/dt = ds_z/dt = 0$ is that $s_y = \phi = 0$, which means that the spin axis has no y-component (i.e., maintains the same phase in the precession cycle as the orbit) and all motion remains in the xz-plane.

4.2.2 Spin dynamics with tidal dissipation

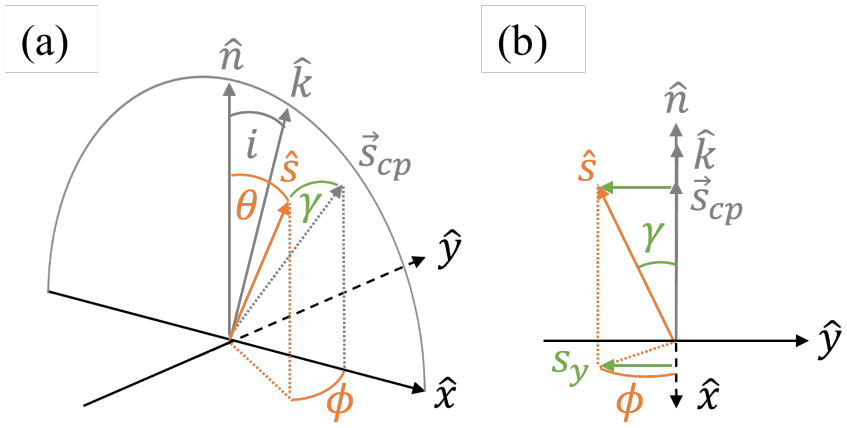

Figure 4.1: A non-zero Cassini plane offset γ is indicative of dissipation. (a) skewed perspective of the Cassini plane offset geometry (b) side-on view of the Cassini plane so that $\hat{x}$ comes out of the page. The component of the spin vector $\hat{s}$ in the reference frame of the precessing Cassini plane (the xz-plane formed by the orbit normal $\hat{n}$ and the Laplace plane normal $\hat{k}$) is $\vec{s}_{cp}$, which is separated from $\hat{s}$ by a distance s_y and an angle γ. Everything in grey lies in the Cassini plane.

Tidal torques drive the satellite to an equilibrium endpoint, which is usually a Cassini state and a spin angular velocity commensurate with the orbital mean motion. Past works have developed various ways to include tidal torques on the spin axis evolution (Goldreich and Peale, 1970; Peale, 1974; Ward, 1975b; Organowski and Dumberry, 2020; Gladman et al., 1996; Correia and Laskar, 2001). The tidal torque averaged over one orbit period is (Goldreich and Peale, 1970; Ward, 1975b; Gladman et al., 1996):

$$\vec{\tau_T} = C\omega T \left[-\frac{1}{2}\hat{s} + \left(\frac{n}{\omega} - \frac{1}{2}\cos\theta \right) \hat{n} \right] \tag{4.4}$$

Where $C = cMR^2$ is the satellite's polar moment of inertia and T is a parameter defined

as (Ward, 1975b; Gladman et al., 1996):

$$T = 3\frac{k_2}{Q}\frac{n}{c}\left(\frac{M_p}{M}\right)\left(\frac{R}{a}\right)^3 \tag{4.5}$$

where M and R are the satellite's mass and radius, and k_2/Q is the tidal dissipation parameter. From here on out we deal only with synchronous satellites (i.e., $\omega = n$), which allows us to approximate the time lag between when the planet is overhead and when the satellite's tidal bulge responds as $\Delta t = 1/nQ$.

The tidal torque has two components, one along $\hat{s}$ that drives the spin rate to synchronous and one along $\hat{e}$ that changes the obliquity. The unit vector $\hat{e}$ lies in the equator plane, perpendicular to both $\hat{s}$ and the line of nodes, such that $\hat{n} = \cos\theta\hat{s} + \sin\theta\hat{e}$. Taking the spin rate as a constant (i.e., $d\omega/dt = 0$), the tidal torque changes the spin angular momentum by changing only the spin axis unit vector along $\hat{e}$:

$$\begin{aligned}
\frac{d\hat{s}}{dt}|_{tid} &= \frac{1}{C\omega}(\vec{\tau}_T \cdot \hat{e})\hat{e} \\
\frac{d\hat{s}}{dt}|_{tid} &= T\left(1 - \frac{1}{2}\cos\theta\right)(\hat{n} - \cos\theta\hat{s})
\end{aligned} \tag{4.6}$$

From Eq. 4.6, tidal dissipation drives the spin axis towards the orbit normal, which would ultimately result in zero obliquity. With precessional torques (Eq. 4.2), the equilibrium Cassini state obliquity is non-zero. All sources of dissipation drive the spin axis to an equilibrium state. The above analysis has focused on solid-body tides, and a treatment of torques at the core-mantle boundary is included in Section 4.2.3. In the case of Titan, we conclude that the latter is likely negligible, but we include it for completeness.

4.2.3 Spin dynamics with dissipation at the core-mantle boundary

In the case of a body with an internal fluid layer, when the fluid core and overlying mantle have different spin vectors, the differential rotation induces a torque on the mantle and leads to friction at the core-mantle boundary (CMB) (Goldreich and Peale, 1970; Yoder, 1981; Goldreich, 1967; Correia and Laskar, 2001; Toomre, 1966; Rochester, 1976; Correia, 2006). This friction helps drive the spin evolution of the mantle, so it is important to take it into account. Our terminology here is based on the situation for the Moon. The analogous situation for an icy ocean world is that the ice shell (mantle) is torqued by the ocean (fluid outer core) beneath. To avoid duplication, we will generally refer to "core" and "mantle" with the adjustment for the case of icy moons being implicit.

Here we present a first-order derivation of how torques at the core-mantle boundary affect the spin angular momentum of the mantle. The rate of change of the mantle's spin angular momentum is given by:

$$\frac{d(C_m\vec{\omega})}{dt} = \vec{\tau}_{\rm cmb} \tag{4.7}$$

where C_m is now the moment of inertia of the mantle. The torque on the mantle is $\vec{\tau}_{\rm cmb} = K(\vec{\omega}_c - \vec{\omega})$, where K is a dissipation parameter, $\vec{\omega}_c$ is the rotation vector of the fluid layer, and $\vec{\omega}$ is still the rotation vector of the mantle (e.g., Goldreich and Peale, 1970; Yoder, 1981; Williams et al., 2001). The rate of change of the mantle spin orientation due to core-mantle boundary torques is:

$$\frac{d\hat{s}}{dt}|_{\rm cmb} = \frac{1}{C_m n}K(\vec{\omega}_c - \vec{\omega}) \tag{4.8}$$

If the core spin vector is aligned with the mantle spin vector, then the torque will vanish. Otherwise, we assume that the mantle and core spin axes have the same azimuth and only differ in their obliquities such that $\vec{\omega}_c = n(\cos\Delta\epsilon\hat{s} + \sin\Delta\epsilon\hat{e})$ where $\Delta\epsilon$ is the angular separation between the two vectors. Therefore, in Eq. 4.8, $\vec{\omega}_c - \vec{\omega} = n(\cos\Delta\epsilon\hat{s} + \sin\Delta\epsilon\hat{e} - \hat{s})$. Neglecting 2nd-order terms in $\Delta\epsilon$:

$$\vec{\omega}_c - \vec{\omega} \approx n\sin\Delta\epsilon\hat{e} \tag{4.9}$$

which indeed tends to zero when there is no angular separation. For weak coupling, the core spin vector will lie close to the Laplace plane pole and $\Delta\epsilon = \theta - i$ (Yoder, 1981; Dickey et al., 1994; Williams et al., 2001). Plugging this into our spin equations of motion:

$$\begin{aligned}\frac{d\hat{s}}{dt}|_{\text{cmb}} &= \frac{1}{C_m n}Kn\sin\Delta\epsilon\hat{e} \\ \frac{d\hat{s}}{dt}|_{\text{cmb}} &= \frac{K}{C_m}\frac{\sin\Delta\epsilon}{\sin\theta}(\hat{n} - \cos\theta\hat{s})\end{aligned} \tag{4.10}$$

From Eq. 4.10, torques at the core-mantle boundary will act to align the core and mantle spin axes and to bring the spin axis towards the orbit normal. The parameter K has different functional forms for laminar and turbulent flow (Yoder, 1981; Williams et al., 2001; Correia, 2006).

For simplicity, in Eq. 4.10 we ignore a correction factor for coupling between the fluid layer and the overlying mantle, which affects the angular separation between the core and mantle spin axes. We either assume that there is weak coupling, in which case Eq. 4.10 applies, or that there is strong coupling, in which case Eq. 4.10 vanishes. This is compared to (Organowski and Dumberry, 2020) who use a pressure coupling

correction factor on their expression for the offset due to CMB friction. For the rest of this section, we summarize past conclusions that the Moon experiences weak coupling at the CMB, and we make the case that Titan experiences strong coupling at the ice shell-ocean interface.

4.2.4 Pressure coupling

Pressure coupling causes the core to precess about the mantle spin axis at a rate which depends on the ellipticity of the core-mantle boundary (e.g., Meyer and Wisdom, 2011). If this precession, also known as the free core nutation (or analogously for an icy satellite, the free ocean nutation, (Baland et al., 2019)) is faster than the mantle's precession, the core can follow the mantle and will align with it, otherwise the core is too slow and will instead align with the Laplace pole. The condition for negligible pressure coupling and a core aligned with the Laplace pole is:

$$n f_{\mathrm{cmb}} \frac{C}{C_m} < \dot{\Omega} \tag{4.11}$$

where f_{cmb} is the polar flattening of the core-mantle boundary (Goldreich and Peale, 1970; Meyer and Wisdom, 2011).

In accordance with Goldreich (1967) and Meyer and Wisdom (2011), we find that pressure coupling between the lunar core and mantle is negligible. Because the Moon's core is so small, C_m is very close to C. The Moon's core oblateness from lunar laser ranging analyses is $f_c = 2.2 \times 10^{-4}$ (28), which is less than $\dot{\Omega}/n = 4.0 \times 10^{-3}$. Application of Eq. 4.11 shows that the flattening of the core-mantle boundary is too low

by an order of magnitude for pressure coupling to align the lunar core and mantle. The core's spin axis is aligned with the Laplace pole, and the angular separation between the core and mantle spin axes is $\theta - i = 1.5°$.

We argue that the opposite is true for Titan, that given predicted ranges for its ice shell thickness and ice shell-ocean boundary flattening, its ocean layer should precess fast enough to be aligned with the ice shell. The main effect of the ice shell thickness is on the ice shell's moment of inertia, C_m. Titan's C_m, can be calculated from the polar flattenings of its surface and ice shell-ocean boundary, f_s and f_{cmb} respectively (e.g., Viswanathan et al., 2019):

$$C_m = \frac{8\pi}{15}\rho_m \left[R^5\left(1+\frac{2}{3}f_s\right) - R_{\mathrm{cmb}}^5\left(1+\frac{2}{3}f_{\mathrm{cmb}}\right)\right] \tag{4.12}$$

Here ρ_m is the uniform density of the ice shell and $R_{\mathrm{cmb}} = R - d$ where d is the ice shell thickness. Titan's surface polar flattening is $f_s = 19.22 \times 10^{-5}$ (Baland et al., 2014; Zebker et al., 2009). Neither d nor f_{cmb} has been directly measured, but there are estimated ranges for both. Titan's C_m is 21 per cent of C for an ice shell thickness of 200 km and would be an even smaller fraction for thinner ice shells.

Using Titan's gravity field, shape, and rotation, the oblateness of Titan's shell-ocean interface, f_{cmb}, has been inferred. While Titan's degree-2 gravity coefficients are consistent with hydrostatic equilibrium (Iess et al., 2012; Durante et al., 2019) the shape of the triaxial ellipsoid suggests non-hydrostatic contributions (Zebker et al., 2009). The non-hydrostatic surface flattening means that other layers in the interior will not be hydrostatic either. The non-hydrostatic oblateness of Titan's shell-ocean interface in

(Baland et al., 2014) can range from $\geq -2 \times 10^{-4}$ to -4.4×10^{-3} depending on the density profile and the ice shell thickness. A similar range is found in (Coyette et al., 2018). The ocean flattenings are negative to compensate for the excess non-hydrostatic flattening at the surface (Coyette et al., 2018).

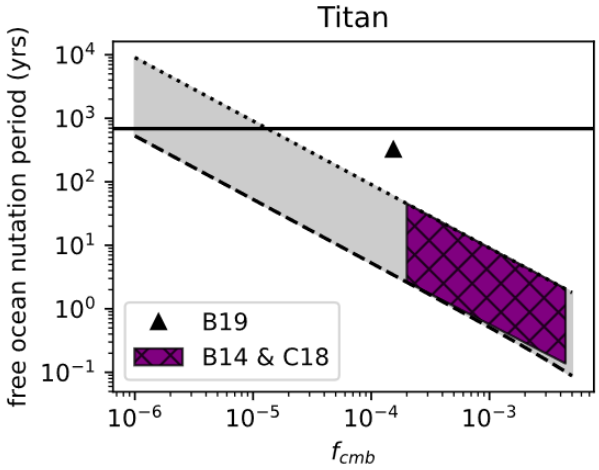

Figure 4.2: Titan's free ocean nutation period as a function of the flattening of the ice shell-ocean interface, $f_{\rm cmb}$. The grey shaded region encompasses ice shell thicknesses ranging from 10-200 km. The purple dotted region is the range of $f_{\rm cmb}$ reported by Baland et al. (2014) (B14) and Coyette et al. (2018) (C18). The triangle marks the assumed $f_{\rm cmb}$ and modelled free ocean nutation period from Baland et al. (2019). The axial precession period of the ice shell (solid black line) is 687 years (JPL Horizons). The ocean's expected precession (purple and triangle) is faster than the ice shell's, so we predict that the ocean will be aligned with the ice shell spin axis resulting in no differential rotation at the ice shell-ocean interface.

To determine whether the spin axis of Titan's ocean is aligned with the ice shell, we find the range of free ocean nutation periods as a function of ice shell thickness and the polar flattening of the ice shell-ocean boundary, shown in Fig. 4.11. Larger flattenings cause the core to precess faster as does a larger core moment of inertia, which can be accomplished through a smaller ice shell thickness. The grey shaded

region represents possible core precession periods encompassing the range of ice shell thicknesses, 10-200 km, explored in Baland et al. (2011, 2014); Coyette et al. (2018). The purple dotted region is bounded by the $|f_{\mathrm{cmb}}|$ values from Baland et al. (2014); Coyette et al. (2018), -2×10^{-4} to -4.4×10^{-3}. The borders of this area do not exactly line up with the grey area because negative f_{cmb} values increase C_m slightly, which decreases the core precession frequency. The triangle represents the assumed f_{cmb} for the rotational model in Baland et al. (2019) of 1.54×10^{-4}, which finds a free ocean nutation period of 324 years. The order of magnitude difference between the calculated period and that found in the model can be explained by the strong effect that the solid interior of Titan has on the ocean above it (Baland et al., 2019).

The key takeaway is that the spin axis of Titan's ocean should be aligned with the spin axis of the ice shell. For a 200 km-thick ice shell, Titan's f_{cmb} would have to be $< 10^{-5}$ for pressure coupling to be negligible and for the core to precess about the Laplace pole. For a 10 km-thick ice shell, the constraint is even stricter at $f_{\mathrm{cmb}} < 10^{-6}$. Instead, the estimated f_{cmb} of 2×10^{-4} to 4.4×10^{-3} is one to three orders of magnitude larger than the cutoff, so we predict that Titan's ocean is aligned with the ice shell spin axis. The free ocean nutation period of 324 years from Baland et al. (2019) is still shorter than the 687-year spin axis precession period, which corroborates that the ocean and ice shell should be aligned. With no differential rotation at the ice shell-ocean interface, there are negligible core-mantle boundary torques and associated dissipation. Because of this, we assume below that all of Titan's Cassini plane offset is due to tidal dissipation.

4.2.5 Equilibrium spin state with tidal and core-mantle boundary dissipation

The complete equations of motion for the mantle spin axis including torques from tides and differential rotation at the core-mantle boundary are:

$$\frac{d\hat{s}}{dt} = \frac{d\hat{s}}{dt}|_{rot} + \frac{d\hat{s}}{dt}|_{tid} + \frac{d\hat{s}}{dt}|_{cmb} \tag{4.13}$$

Solving for the steady-state spin axis from $d\hat{s}/dt = 0$ yields

$$s_x = \sin\theta\cos\phi = \left\{\frac{3}{2}\frac{n}{c}\left[(J_2 + C_{22})\cos\theta + C_{22}\right] + \dot{\Omega}\cos i\right\}\frac{\sin\theta\tan\theta}{\dot{\Omega}\sin i} \tag{4.14}$$

$$s_y = \sin\theta\sin\phi = \left[T\left(1 - \frac{1}{2}\cos\theta\right)\sin\theta + \frac{K}{C}\sin\Delta\epsilon\right]\frac{\sin\theta}{\dot{\Omega}\sin i} \tag{4.15}$$

$$s_z = \cos\theta \tag{4.16}$$

Torques on the satellite's permanent figure dictate the magnitude of s_x compared to s_z, reinforcing the idea that the obliquity is a forced value so that the precessional periods match. Dissipation is the only mechanism driving the spin axis off the Cassini plane.

We derive the new Cassini state relation (a non-linear relationship between the obliquity and known parameters) by starting with the equation $ds_y/dt = 0$, but it can also be done with the identity $1 = \cos^2\phi + \sin^2\phi$. We derive the spin axis azimuth by starting with the equation $ds_x/dt = 0$:

$$\begin{aligned}(\dot{\Omega}\sin i)^2 = &\left\{\frac{3}{2}\frac{n}{c}\left[(J_2 + C_{22})\cos\theta + C_{22}\right] + \dot{\Omega}\cos i\right\}^2\tan^2\theta \\ &+ \left[T\left(1 - \frac{1}{2}\cos\theta\right)\sin\theta + \frac{K}{C}\sin\Delta\epsilon\right]^2\end{aligned} \tag{4.17}$$

$$\tan\phi = \frac{\left[T\left(1 - \frac{1}{2}\cos\theta\right) + \frac{K}{C}\frac{\sin\Delta\epsilon}{\sin\theta}\right]\cos\theta}{\frac{3}{2}\frac{n}{c}\left[(J_2 + C_{22})\cos\theta + C_{22}\right] + \dot{\Omega}\cos i} \tag{4.18}$$

Another expression can be formed assuming ϕ is small so that $\tan\phi \approx \sin\phi$ and using $\sin\gamma = \sin\theta\sin\phi$.

$$\sin\gamma \approx \frac{\left[T\left(1-\frac{1}{2}\cos\theta\right)\sin\theta + \frac{K}{C}\sin\Delta\epsilon\right]\cos\theta}{\frac{3}{2}\frac{n}{c}\left[(J_2+C_{22})\cos\theta + C_{22}\right] + \dot{\Omega}\cos i} \tag{4.19}$$

Our expression Eq. 4.19 is similar to Eq. 63 of Organowski and Dumberry (2020), differing only by the denominator and by the fact that they include a pressure coupling factor on the core-mantle boundary term. Eq. 4.19 can only be used for the Moon and not Titan, however, because it assumes that ϕ is small ($\phi = 6.5\times10^{-4}$ ° for the Moon), whereas for Titan $\phi = 22°$ (Table 4.2). Furthermore, there is a mismatch between the $(J_2+2C_{22})/c$ derived from Titan's gravity measurements ($\sim 1.6\times10^{-4}$) and that derived from its obliquity ($\sim 7.9\times10^{-5}$), so we use Eq. 4.24 in Section 4.3.1 over Eq. 4.19 and take the obliquity as given rather than solving for it.

4.2.6 Uncertainty analysis for k_2/Q

In the case where CMB dissipation can be neglected, Titan's Cassini plane offset, γ, is related to k_2/Q by:

$$\sin\gamma = 3\frac{k_2}{Q}\frac{n}{c}\left(\frac{M_p}{M}\right)\left(\frac{R}{a}\right)^3\left(1-\frac{1}{2}\cos\theta\right)\frac{\sin^2\theta}{\dot{\Omega}\sin i} \tag{4.20}$$

Rearranging to solve for Titan's solid-body k_2/Q, we get:

$$\frac{k_2}{Q} = \frac{\sin\gamma}{3\frac{n}{c}\left(\frac{M_p}{M}\right)\left(\frac{R}{a}\right)^3\left(1-\frac{1}{2}\cos\theta\right)}\frac{\dot{\Omega}\sin i}{\sin^2\theta} \tag{4.21}$$

The uncertainty in k_2/Q, $\Delta(k_2/Q)$ is related to the uncertainties in the Cassini plane offset, obliquity, and normalized polar moment of inertia, $\Delta\gamma$, $\Delta\theta$, Δc by:

$$\left[\Delta\left(\frac{k_2}{Q}\right)\right]^2 = \left[\frac{\partial}{\partial\gamma}\left(\frac{k_2}{Q}\right)\Delta\gamma\right]^2 + \left[\frac{\partial}{\partial\theta}\left(\frac{k_2}{Q}\right)\Delta\theta\right]^2 + \left[\frac{\partial}{\partial c}\left(\frac{k_2}{Q}\right)\Delta c\right]^2 \tag{4.22}$$

where the uncertainties in k_2/Q with respect to the two main angles, γ and θ, add in quadrature. The partial derivatives are:

$$\begin{aligned}
\frac{\partial}{\partial\gamma}\left(\frac{k_2}{Q}\right) &= \frac{k_2}{Q}\cot\gamma \\
\frac{\partial}{\partial\theta}\left(\frac{k_2}{Q}\right) &= -\frac{k_2}{Q}\left(\frac{\sin\theta}{2-\cos\theta} + 2\cot\theta\right) \\
\frac{\partial}{\partial c}\left(\frac{k_2}{Q}\right) &= \frac{k_2}{Q}\frac{1}{c}
\end{aligned} \tag{4.23}$$

Assuming Titan is in hydrostatic equilibrium as supported by the degree-2 gravity coefficients, J_2 and C_{22}, $c = 0.341$ (Durante et al., 2019). Relaxing the hydrostatic requirement allows for a lower bound of 0.31 from the obliquity and tidal k_2 measurements (Baland et al., 2014) and an upper bound of 0.36 from the fluid Love number from non-hydrostatic topography (Hemingway et al., 2013). As such, we use an uncertainty in the normalized polar moment of inertia of 0.03.

Using Eqs. 4.23 and the uncertainty values of $\Delta\gamma = 0.02°$, $\Delta\theta = 0.02°$ (Baland et al., 2011), and $\Delta c = 0.03$, $\Delta(k_2/Q) = 0.027$.

Table 4.1: Physical and orbital parameters for satellites studied in this paper. Unless specified otherwise, values are from JPL SSD Database. The Moon's J_2 and C_{22} are from GRAIL (Konopliv et al., 2013), the Moon's c is from GRAIL and LLR (Williams et al., 2014), Titan's J_2, C_{22}, and c are from Cassini (Durante et al., 2019), Io's J_2, C_{22} and c are from Galileo (Anderson et al., 2001b), and Ganymede's J_2, C_{22} and c are from Galileo and Juno (Gomez Casajus et al., 2022) The nodal precessions for Io and Ganymede are from Noyelles (2009)

	M_p (kg)	M (kg)	R (km)	a (km)	e	i (°)	$2\pi/\dot{\Omega}$ (yr)	J_2	C_{22}	c
Moon	5.97×10^{24}	7.3×10^{22}	1738.0	0.38×10^6	0.055	5.16	18.6	203.3×10^{-6}	22.4×10^{-6}	0.393
Titan	5.68×10^{26}	13.5×10^{22}	2575.5	1.22×10^6	0.029	0.28	687.4	33.1×10^{-6}	10.4×10^{-6}	0.341
Io	1.90×10^{27}	8.9×10^{22}	1821.5	0.42×10^6	0.005	0.04	7.4	1845.9×10^{-6}	553.7×10^{-6}	0.377
Ganymede	1.90×10^{27}	14.8×10^{22}	2631.2	1.07×10^6	0.001	0.21	136.1	133.0×10^{-6}	39.6×10^{-6}	0.316

4.3 Results

4.3.1 Equilibrium Cassini plane offset with tidal and CMB dissipation

In equilibrium, the spin axis of a synchronous satellite is configured so as to balance the torques acting on its outermost layer, which we refer to generally as the mantle even for icy satellites with an ice shell. We consider three torques on the mantle: the gravitational torque exerted by the planet on the satellite's permanent triaxial figure, the torque on its tidal bulge, and the torque resulting from differential rotation at the core-mantle boundary (CMB). Tidal dissipation depends on the factor, k_2/Q, where k_2 is the tidal Love number that measures how deformable the body is to tides and $1/Q$ is related to the lag in the body's tidal response (a greater lag means more friction). Dissipation at the CMB depends on the factor K/C, where K is the coupling constant between the solid and liquid layers and C is the polar moment of inertia of the mantle.

In the reference frame of a uniformly precessing orbit, the spin axis unit vector is $\hat{s} = (s_x, s_y, s_z) = (\sin\theta\cos\phi, \sin\theta\sin\phi, \cos\theta)$. The obliquity θ is the angle between the spin axis and orbit normal, and ϕ is the azimuth in the orbit plane or longitude of the ascending node of the equator plane on the orbit plane (see Fig. 4.1). In this geometry, the Cassini plane formed by the orbit normal and the Laplace plane normal is the xz-plane. The angle between the spin axis and the Cassini plane is γ such that $s_y = \sin\gamma$ (Yseboodt and Margot, 2006).

We derive the equilibrium Cassini plane offset γ (see Section 4.2) as a function of the tidal dissipation factor k_2/Q and the CMB dissipation factor K/C under the as-

sumption that only a single forcing frequency (that of the orbit precession) is operating. Eq. 4.24 comes from $s_y = \sin\gamma$ (Eq. 4.15):

$$\sin\gamma = \left[3\frac{k_2}{Q}\frac{n}{c}\frac{M_p}{M}\left(\frac{R}{a}\right)^3\left(1-\frac{1}{2}\cos\theta\right)\sin\theta + \frac{K}{C}\sin\Delta\epsilon\right]\frac{\sin\theta}{\dot{\Omega}\sin i} \tag{4.24}$$

where M_p is the mass of the planet and $R, M, c, n, a, i, \dot{\Omega}$ are respectively the satellite's radius, mass, normalized polar moment of inertia, orbital mean motion, semi-major axis, inclination between the orbit and Laplace plane, and precession frequency of the orbit about the Laplace plane. The angle between the mantle's spin axis and the core's spin axis is $\Delta\epsilon$. Our Eq. 4.24 can be related to the expression for the Cassini plane offset in Organowski and Dumberry (2020) (see Section 4.2).

In the absence of dissipation (i.e., $k_2/Q = K/C = 0$), the spin axis lies in the Cassini plane and precesses in phase with the orbit normal ($\phi = \gamma = 0$). With dissipation, the steady-state spin axis lies off the Cassini plane with a non-zero ϕ and γ. The physical significance of this is that any dissipation will cause a lag in the body's precession, so to compensate, the permanent figure (i.e., the spin axis) is oriented ahead in the rotation cycle (Organowski and Dumberry, 2020). Eq. 4.24 is the key expression for this paper, because it relates the observable quantity γ to dissipation factors that are otherwise hard to measure.

4.3.2 Verifying our approach with the Moon

Lunar laser ranging (LLR) data have detected a Cassini plane offset of γ = -7.5 $\times 10^{-5}$ ° for the Moon (Yoder, 1981; Williams et al., 2014, 2001). In addition to tidal

heating, the Moon experiences CMB friction because its core is expected to align with the ecliptic normal rather than rotating with the mantle (Yoder, 1981; Goldreich, 1967). This is confirmed by estimates of the lunar free core nutation, which is the precession of the oblate fluid core about the mantle symmetry axis. From LLR data, the lunar free core nutation period is calculated to be 367 ± 100 years (Viswanathan et al., 2019), which is much longer than the mantle axial precession of 18.6 years, so the core cannot follow the mantle and instead should align with the ecliptic normal.

The lunar Cassini plane offset can be connected to both tides and CMB friction via Eq. 4.24. Because there is a degeneracy in attributing the offset to the two sources of dissipation, we solve for two end-member scenarios: one in which tides account for the total dissipation in the Moon, yielding $k_2/Q = 1.2 \times 10^{-3}$ and one in which friction at the CMB does, yielding $K/C = 4.1 \times 10^{-13} s^{-1}$. The end-member scenarios place upper bounds on k_2/Q and K/C, so Fig. 4.3 shows the curve for the intermediate solutions.

Luckily, LLR data are able to break the degeneracy because tidal and CMB dissipation damp the free libration modes and the orbital elements differently (Williams et al., 2001). From LLR data, $k2/Q = (6.4 \pm 1.5) \times 10^{-4}$ and $K/C = (1.63 \pm 0.39) \times 10^{-13} s^{-1}$ (Williams and Boggs, 2015), so about half of the lunar Cassini plane offset can be attributed to solid-body tides and half to core-mantle boundary friction. Our solution curve in Fig. 4.3 matches very well with the LLR parameters.

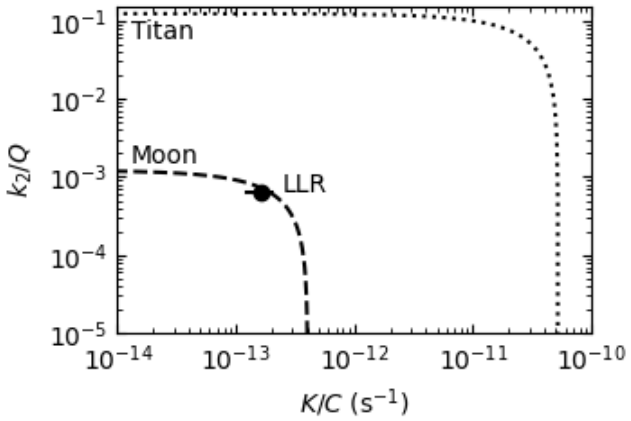

Figure 4.3: Titan's dissipative parameters are orders of magnitude larger than the Moon's. The curves are the dissipation solutions that produce the Cassini plane offsets of the Moon (solid) and Titan (dotted), using Eq. 4.24 Tidal dissipation is parameterized by k_2/Q and friction at the CMB is parameterized by K/C. The parameters fit to the LLR data including error bars from Williams and Boggs (2015) (dot) places constraints on the Moon that our solution curve passes through.

4.3.3 Application to Titan

Analyses of Cassini radar images found Titan's spin state, consisting of $\theta = -0.323°$ and $\gamma = 0.091°$ (Stiles et al., 2008) and more recently $\theta = -0.31°$ (Meriggiola et al., 2016). Factoring in uncertainties in the IAU orbit determination, Baland et al. (2011) obtained $\theta = -0.32 \pm 0.02°$ and $\gamma = 0.12 \pm 0.02°$, which we will use here (see discussion in Baland et al. (2014). Unlike for the Moon, we calculate that Titan's solid layer (ice shell) and underlying liquid layer (ocean) should have aligned spin axes, so there will be negligible torques and dissipation induced by differential rotation at the CMB (see Section 4.2.4).

We find the two end-member scenarios for Titan in the same way as we did

for the Moon. We include a solution assuming differential rotation at the CMB for completeness. As shown in Fig. 4.3, the tidal upper bound is $k_2/Q = 0.12 \pm 0.027$, and the differential rotation upper bound is $K/C = 5.1 \times 10^{-11} s^{-1}$. The uncertainty on the upper limit for k_2/Q comes from the uncertainty in the obliquity and Cassini plane offset (Baland et al., 2011) as well as the normalized polar moment of inertia (see Section 4.2.6).

Our results are consistent with some interior models and with the upper bounds from data. Adding dissipation to their tidal analysis, Durante et al. (2019) found that Titan's time-variable gravity coefficients are compatible with $k_2/Q < 0.2$ (including zero). Interior models for Titan with low viscosities can also produce $k_2 = 1.0$ and $k_2/Q < 0.1$ (Iess et al., 2012).

Our k_2/Q value assumes that all of the offset is from solid-body tides. We neglect differential rotation between the ocean and the inner ice-rock core as well as atmospheric effects (cf. Baland et al. (2019)). We also neglect tidal dissipation in the subsurface ocean (Sagan and Dermott, 1982; Sohl et al., 1995; Chen et al., 2014; Hay and Matsuyama, 2019; Idini and Nimmo, 2024) because this represents work done by the tidal potential (Chen et al., 2014; Hay and Matsuyama, 2017) rather than a torque that can change the spin angular momentum of the ice shell. If there is a net torque that the ocean flow exerts on the ice shell on the other hand, then this would contribute to the Cassini plane offset. In any event, the large k_2/Q that we have derived here indicates a large source of dissipation located somewhere on Titan.

4.3.4 Dynamical implications for Titan

The upper bound on our inferred k_2/Q of 0.12±0.027 would produce significant tidal heating in Titan. The standard rate of solid-body tidal heating in a synchronous satellite for small eccentricity, e, and obliquity, θ is (e.g., Peale and Cassen, 1978; Wisdom, 2004):

$$\dot{E} = \frac{3}{2}\frac{k_2}{Q}\frac{n^5 R^5}{G}(7e^2 + \sin^2\theta) \tag{4.25}$$

Fig. 4.4a shows the heating from solid-body eccentricity and obliquity tides as a function of k_2/Q. For comparison, the heating from ocean obliquity tides is 1.4×10^{-6} Wm^{-2} using the scaling laws in Hay and Matsuyama (2019) and a bottom drag coefficient of 2.4×10^{-6} from the scaling law in Fan et al. (2019). The present-day radiogenic heat estimate for Titan is 3 mW m^{-2} (Kirk and Stevenson, 1987; Mitri and Showman, 2008). Our baseline k_2/Q of 0.12 would produce a surface heat flux of 40 mW m^{-2}, primarily due to solid-body eccentricity tides, which is an order of magnitude higher than the present-day radiogenic heating.

Our inferred k_2/Q would contribute a semi-major axis shrinking rate of 6 cm/yr. For reference, Titan's observed net outwards migration rate from astrometry without including dissipation in Titan is +11 cm/yr (Lainey et al., 2020), although this is fit-dependent (Jacobson, 2022). If the Q of Titan is as low as we suspect, that in turn implies that the Q of Saturn at Titan's frequency is lower than is currently thought.

A natural question is whether Titan's orbital elements could survive damping due to tidal heating over the lifetime of the solar system (Sagan and Dermott, 1982; Sohl

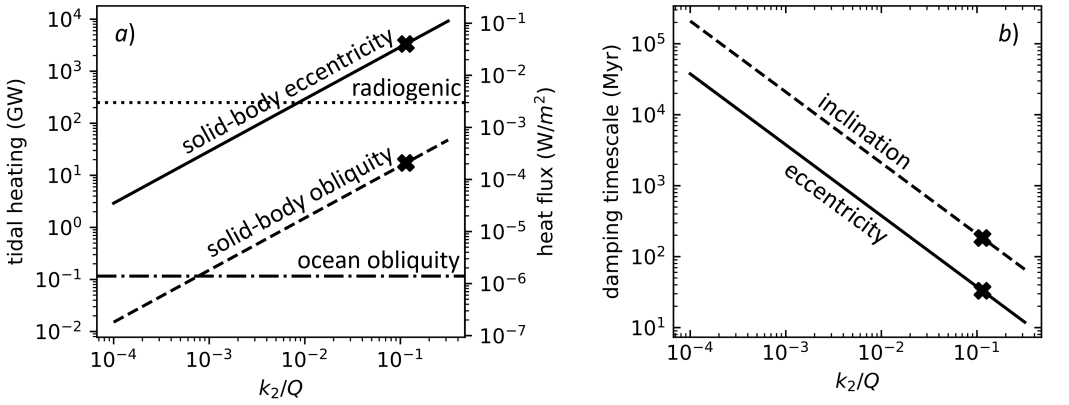

Figure 4.4: Titan's strong solid-body tidal heating suggests a recent source of its eccentricity and inclination. a) Titan's heating as a function of k_2/Q for solid-body eccentricity tides (solid), solid-body obliquity tides (dashed), ocean obliquity tides (dash-dot, Hay and Matsuyama (2019), and radiogenic heating (dotted, Kirk and Stevenson (1987); Mitri and Showman (2008) Our tidal end-member of $k_2/Q = 0.12$ (cross) corresponds to a surface heat flux of ~ 40 mW m^{-2}. b) How Titan's eccentricity and inclination damping timescales depend on k_2/Q. For $k_2/Q = 0.12$, the damping timescales are $\tau_e \sim 30$ Myr and $\tau_i \sim 170$ Myr, much shorter than the age of the solar system.

et al., 1995; Peale et al., 1980; Sears, 1995; Tobie et al., 2005b). The rate of eccentricity and inclination decay due to energy extracted from the orbit, e.g., satellite eccentricity and obliquity tides, is (e.g., Chyba et al., 1989):

$$\frac{di}{dt} = \frac{a}{GM_pM}\frac{1}{\tan i}\dot{E}_\theta \tag{4.26}$$

$$\frac{de}{dt} = \frac{a}{GM_pM}\frac{1-e^2}{e}\dot{E}_e \tag{4.27}$$

Using Eqs. 4.26 and 4.27, we calculate an order of magnitude damping timescale for the eccentricity $\tau_e = e/de/dt$ and inclination $\tau_i = \tan i/di/dt$. For $k_2/Q = 0.12$, $\tau_e \sim 30$ Myr and $\tau_i \sim 170$ Myr. CMB dissipation lowers the inclination and shrinks the semimajor axis but is an order of magnitude less effective at doing so than tides (Williams et al., 2001). CMB dissipation does not affect the eccentricity. Fig. 4.4b shows the eccentricity

and inclination damping timescales as a function of k_2/Q. The solid-body k_2/Q would have to be $\leq 10^{-3}$ ($Q \geq 600$) for the eccentricity damping timescale to be the age of the solar system and $\leq 6 \times 10^{-3}$ ($Q \geq 100$) for the inclination damping timescale to be the age of the solar system. The tidal damping timescales of Titan's orbital elements are much shorter than the age of the solar system, potentially requiring a recent excitation (see Discussion).

4.3.5 Interior implications for Titan

If Titan's ice shell is conductive, our inferred surface heat flux of 40 mW m^{-2} (about 3 TW) suggests a relatively low equilibrium ice shell thickness, $d \approx 20$ km if heating occurs below the ice shell, or somewhat thicker if the heating is in the ice shell (Nimmo and Bills, 2010). Such a thickness is lower than the 55-80 km inferred from a detection of a Schumann-like resonance in Titan's atmosphere (Béghin et al., 2012) and the 100 km from topography analyses (Nimmo and Bills, 2010). For a convecting ice shell, a heat flux of 40 mWm^{-2} is at the high end of existing model estimates (Mitri and Showman, 2008; Tobie et al., 2006) but would permit a thicker ice shell.

Titan's degree-2 potential Love number from Cassini data is $k_2 = 0.616 \pm 0.067$ (Iess et al., 2012; Durante et al., 2019), so taking an upper bound on $k_2/Q < 0.147$, the tidal quality factor, Q, has a lower bound of $Q \geq 3.7$. Another analysis of Cassini radiometric tracking data found k2 in the range 0.3 - 0.4 (Goossens et al., 2023), implying a lower bound on Q of 2.0 – 2.7.

We can ask what solid-body viscosity would be required to yield the inferred lag

in Titan's tidal response k_2/Q. Using the expression in Iess et al. (2012), $k_2/Q = 0.12$ would require an effective viscosity of the whole body of 3×10^{13} Pa s, which is on the lower end of the range of estimates for high-pressure ice, 10^{12} – 10^{23} Pa s (Journaux et al., 2020). In a simple Titan model, in which we reduce the viscosities of the two inner layers of Hemingway et al. (2013) to an ice-like value of 10^{15} Pa s, we obtain a Q of 10. Neither of these calculations is meant to be a realistic model but simply to emphasize that our understanding of Titan's internal structure is not currently good enough to be able to rule out $Q \approx 5$ on theoretical grounds.

The low Q value of 5 is lower than previous assumptions but comparable to other solar system bodies. From astrometry, Io's k_2/Q is 0.015 (Lainey et al., 2009). Assuming Io has partial melting but no magma ocean, $k_2 \sim 0.1$ (Bierson and Nimmo, 2016), in which case $Q \sim 7$. The Earth's Q is ~ 13 (MacDonald, 1964; Lambeck, 1975), mostly due to dissipation in the shallow surface ocean. Primarily solid-body Q's are larger: that for Mars is ~ 90 (Jacobson and Lainey, 2014) and for the Moon which has $k_2/Q = 6.4 \times 10^{-4}$ and $k_2 = 0.024$, $Q = 38$ at monthly periods (Williams and Boggs, 2015).

4.3.6 Application to Io, Europa, Ganymede, and Callisto

Io's spin state has never been observed, but heat flow measurements and astrometry indicate that it has a solid-body k_2/Q of 0.015 (Lainey et al., 2009). Doing the reverse analysis as for the Moon and Titan, we predict the Cassini plane offset to be at least 2×10^{-5} ° (Table 4.2).

The upcoming Europa Clipper mission aims to determine Europa's rotation state, including its obliquity and librations. As yet, the precision with which the spin state will be determined from imaging and a rotational ephemeris is unavailable. To get a 0.004 accuracy in the moment of inertia, Mazarico et al. (2023) state a desire to have 0.05 arcmin (8.3×10^{-4} °) accuracy in the obliquity. If this accuracy were to apply to the Cassini plane offset as well, a $k_2/Q > 0.02$ would be detectable.

Ganymede's spin state has been observed (Margot et al., 2013), but its obliquity has not been determined nor are there any direct measurements of its k_2/Q. The upcoming ESA JUICE mission will have the capability to measure the orientation of Ganymede's spin axis (Cappuccio et al., 2020), and thus derive k_2/Q independent of time-variable gravity measurements. The obliquity is projected to have an uncertainty of 1μrad or 5.7×10^{-5} ° (Cappuccio et al., 2020), which if applicable to the whole spin axis, means a signature of $k_2/Q > 1.6 \times 10^{-3}$ should be detectable in the Cassini plane offset. The tidal heat flux for $k_2/Q = 1.6 \times 10^{-3}$ would be a negligible ~ 0.1 mW m^{-2}.

JUICE is also expected to retrieve the spin state of Callisto from 21 flybys, although with an accuracy of only 5.5 mrad for the obliquity (Cappuccio et al., 2022). Callisto's obliquity, let alone Cassini plane offset, will not be well-constrained since the predicted obliquity from Eq. 4.3 is 0.13° while the accuracy is 0.32°. The obliquity may be larger than expected either due to a subsurface ocean or due to resonant perturbations as may be the case for Titan (Baland et al., 2011).

Table 4.2 contains the observed spin angles for the Moon and Titan, their end-member k_2/Q and K/C, and the predicted spin angles for Io and Ganymede from

Table 4.2: Spin angles and endmember dissipative parameters for several satellites. All values that have been measured directly are denoted with an asterisk (*), and the rest are predicted. The cross (+) indicates the minimum value that could be detected by the JUICE mission, assuming a 1-μrad precision.

	$\theta(^\circ)$	$\phi(^\circ)$	$\gamma(^\circ)$	k_2/Q endmember	$K/C(s^{-1})$ endmember
Moon	6.67*	6.5×10^{-4}	7.5×10^{-5}*	0.0012	4.1×10^{-13}
Titan	0.32*	22*	0.12*	0.12	5.1×10^{-11}
Io	0.0022	0.53	2.0×10^{-5}	0.015*	-
Ganymede	0.035	0.096+	5.8×10^{-5}+	0.0016+	-

either measured or detectable k_2/Q. We assume that, like Titan, Ganymede's ice shell will be aligned with the spin axis of its subsurface ocean, so we only predict the tidal endmember. For Io, we neglect the effect of a possible magma ocean on the spin state of the crust.

4.4 Discussion

We have argued that a sufficiently precise measurement of a satellite's offset from a Cassini state can be used to infer the rate of tidal dissipation from Eq. 4.24. Any torque would contribute to the Cassini plane offset, but here we only consider tidal and core-mantle boundary torques. Other works incorporate more sources, for example, Organowski and Dumberry (2020) also explore viscoelastic deformation of the possible lunar solid inner core and Zhang and Dumberry (2021) viscous dissipation at the lunar inner core boundary. Atmospheric torques are another potential complicating factor at Titan that we have neglected (Tokano et al., 2011; Coyette et al., 2018).

We have also neglected any net torque from ocean tides. If tidal dissipation in Titan's subsurface ocean does exert a net torque on the ice shell, then it could account

for some of the Cassini plane offset. For example, if Titan's ocean happens to be resonantly stratified, up to about 1 TW of the total tidal dissipation of ~ 3 TW could be due to ocean eccentricity tidal dissipation (Idini and Nimmo, 2024). Only $\sim 10^8$ W could be from non-resonant ocean obliquity tides. Given the number of potential sources of deformation and torques, further analysis to disentangle their effects on the Cassini plane offset would be desirable.

A limitation of our rotational model is that we can only explain Titan's Cassini plane offset and not its obliquity. Titan's obliquity from Cassini radar images ($-0.32°$) is $\sim$ 3x larger than expected ($-0.10°$) from the Cassini state relation (Eq. 4.3 & 4.17). Put another way, the spin axis precesses about the Laplace plane normal twice as slowly as it should (687 yrs given that it is in a Cassini state vs. 346 yrs calculated from its obliquity and gravity measurements). It was suggested by Bills and Nimmo (2008, 2011) that Titan's larger obliquity is from the ice shell being mechanically decoupled from the interior by a subsurface ocean. An alternative explanation is that the presence of an ocean introduces free modes in the system that resonantly amplify Titan's obliquity (Baland et al., 2011, 2014). The models in Baland et al. (2011, 2014) can explain Titan's obliquity but not its Cassini plane offset. Contrariwise, we attempt to explain Titan's Cassini plane offset, while taking the obliquity as a given.

With $k_2/Q < 0.12$, Titan has a minimum eccentricity and inclination damping timescale of 30 Myr and 170 Myr, which is consistent with a recent excitation of Titan's present-day orbital elements. Titan's present-day eccentricity of $e = 0.029$ is hard to explain if it is a relic of a larger primordial value that has damped due to tidal heating

over the lifetime of the solar system (Sagan and Dermott, 1982; Sohl et al., 1995; Peale et al., 1980; Sears, 1995; Tobie et al., 2005b). Several mechanisms to increase Titan's eccentricity have been suggested including its formation from several giant impacts (Asphaug and Reufer, 2013), accretion of the mid-sized Saturnian satellites in the last 100 Myr (Ćuk et al., 2016a), a near-resonance between Jupiter and Saturn (Bills and Nimmo, 2005), and recent close encounters with a lost satellite or with collisional debris (Ćuk et al., 2016a; Wisdom et al., 2022; Canup, 2010; Teodoro et al., 2023).

A future orbiter to Titan should be able to measure k_2/Q directly from time-variable gravity (Tortora et al., 2017). Combining this measurement with ours would then allow a direct determination of the magnitude of CMB friction or atmospheric torques (Fig. 4.3) and place constraints on Titan's ocean characteristics. More immediately, the upcoming Dragonfly mission to Titan will be able to detect the tidal deformation of the crust via surface measurements (Barnes et al., 2021). The time lag between when the tidal deformation occurs and when Saturn is directly overhead is related to Q. For a Q of 5 and an orbital period of 15.9 days, the tidal time lag will be $\Delta t = 1/nQ \approx 43,700$ s or about 12 hours. Such a lag should be detectable, providing a future test for the k_2/Q derived here.

Chapter 5

Conclusion

Chapters 1 and 3 show that Callisto's and Titan's orbital eccentricities and inclinations are a few hundred million years old, and Chapter 2 shows that while the Moon's inclination is older, it cannot be primordial.

What can we learn by lumping satellites into two categories, those with old orbital geometries and those with young geometries? The unsurprising answer is that solar system bodies continue to interact well after their formation and after periods of instability and numerous collisions. This has implications for the energy needed for habitability if tidal heating can be sporadically turned on as a satellite's orbit is excited and then shut off once the eccentricity and inclination damp away.

The benefit of this scientific methodology is that it separates creating new theories with testing them. A previously proposed event has a timescale and a magnitude of orbital excitation both of which can be put into a tidal evolution model for testing.

The limitations of this method are in the accounting of tides. For example,

the subfield of ocean tidal heating has made considerable numerical progress in the last decade, but the main takeaway is that in some conditions ocean tidal heating can be significant, and in some conditions not. Another hurdle is that solid-body tidal heating depends on a body's k_2/Q, which is known for only two satellites in the solar system.

To advance theoretical modelling of satellite tidal evolution, more mission data is needed. Astrometry is a way to get the rate of change of the orbital elements of a body, which can inform the ratio of tidal dissipation in the planet to that in the satellite. Radio science during spacecraft flybys can get the gravity field of a satellite, which if precise enough, can also tease out the time-variable component due to tides and the lag due to tidal dissipation. Furthermore, the C_{21} gravity coefficient depends on the obliquity of a satellite and so can potentially place bounds on its value. Otherwise, the rotational state of a satellite can be found with surface imagery to get a network of control points whose orientation changes over time. The obliquity is only the Cassini state value for purely solid bodies like the Moon and will be different if there is an ocean. The spin axis azimuth arises because of dissipative torques and so can place an upper bound on the amount of tidal dissipation.

Appendix A

Appendix for Chapter 3

A.1 Introduction

The following are notes, derivations, and literature reviews related to the spin equations of motion for a synchronous satellite. I show where some of the equations of motion come from, for example, for axial precession, nodal precession, and the tidal torque. I do not discuss torques at the core-mantle boundary here because they were presented in my Titan manuscript. I provide an alternative derivation of the equilibrium spin state of a body under the influence of tidal torques (no CMB torques). I include a literature review of other papers that discuss the Cassini plane offset and other notable works that have spin equations of motion should ever they be needed. The contents of this appendix are:

- Rough derivation of the axial precession of a body due to torques on its rotational bulge

Table A.1: Commonly used parameters. If unspecified, quantity is for the satellite.

Symbol	Parameter	Symbol	Parameter
M_p	Mass of the planet	i	Orbital inclination
M	Mass of the satellite	θ	Spin axis obliquity
R	Radius	ϕ	Spin axis azimuth
k_2	Tidal Love number	γ	Cassini plane offset
Δt	Tidal time lag	$\dot{\Omega}$	Nodal precession frequency
Q	Tidal quality factor	$\hat{n}$	Orbit normal
a	Semi-major axis	$\hat{s}$	Spin axis
n	Mean motion	$\hat{k}$	Laplace plane normal
ω	Spin frequency	$\hat{e}$	Direction of decreasing obliquity
$A < B < C$	Moments of inertia	$\vec{\alpha}$	Angular momentum
J_2, C_{22}	Degree-2 gravity coefficients	$\vec{\tau}$	Torque

- Precessional torques – axial precession
- Precessional torques – orbital precession
- Derivation of how the tidal torque affects the obliquity and spin rate of a satellite
- Using the spherical spin equations of motion to find the equilibrium spin state.
- Comparing our equilibrium spin state to other works
- Other works that have spin equations of motion

A.2 Rough derivation of the axial precession of a body due to torques on its rotational bulge

Here is an order-of-magnitude derivation of the axial precession of a body due to torques acting on its rotational bulge. It was motivated by a Planetary Interiors

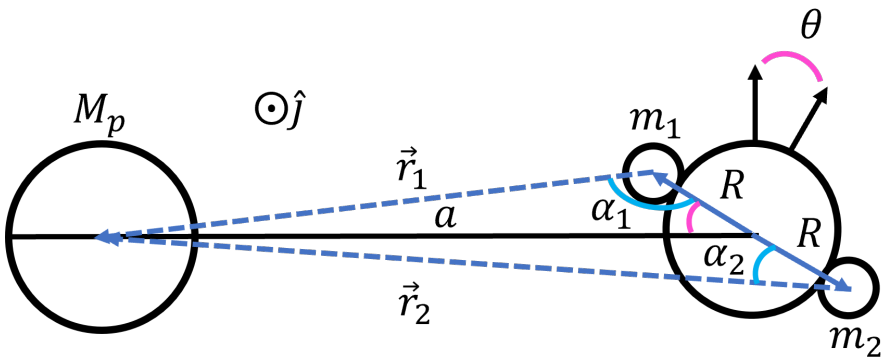

Figure A.1: Geometry of the gravitational force acting on a body's rotational bulge at solstice.

homework question. We will approximate the rotational bulge by the addition of two equal masses on opposite sides of the equator. Defining $m_1 + m_2 = m$ allows us to relate this to the moments of inertia by $C = A + mR^2$ and $mR^2 = C - A$.

The gravitational force $\vec{F}$ between the primary and each of the additions of mass exerts a torque about the center of mass of the body that leads to precession of the orientation of the body about the orbit normal. The torque depends on the angle α between the direction from the center of mass to the additional mass and the direction of the gravitational force:

$$\begin{aligned} \vec{F}_1 &= \frac{GM_p m_1}{r_1^2}\hat{r}_1 \rightarrow \vec{\tau}_1 = R|\vec{F}_1|\sin\alpha_1\hat{j} \\ \vec{F}_2 &= \frac{GM_p m_2}{r_2^2}\hat{r}_2 \rightarrow \vec{\tau}_2 = -R|\vec{F}_2|\sin\alpha_2\hat{j} \end{aligned} \tag{A.1}$$

Since we are doing this exercise when the secondary is at solstice, the rotational bulges

are tilted away from the orbit plane by the obliquity θ. From the law of sines:

$$\begin{aligned}\frac{\sin\alpha_1}{a} &= \frac{\sin\theta}{r_1}\\ \frac{\sin\alpha_2}{a} &= \frac{\sin(\pi-\theta)}{r_2} = \frac{\sin\theta}{r_2}\end{aligned} \tag{A.2}$$

where we have used the fact that $\sin(\pi-\theta) = \sin\theta$. We now have:

$$\begin{aligned}\vec{\tau}_1 &= \frac{GM_p m_1}{r_1^2} R\frac{a}{r_1}\sin\theta\hat{\jmath}\\ \vec{\tau}_2 &= -\frac{GM_p m_2}{r_2^2} R\frac{a}{r_2}\sin\theta\hat{\jmath}\end{aligned} \tag{A.3}$$

Using the law of cosines we get:

$$\begin{aligned}r_1^2 &= a^2 + R^2 - 2aR\cos\theta = a^2\left[1 + \left(\frac{R}{a}\right)^2 - 2\frac{R}{a}\cos\theta\right]\\ r_2^2 &= a^2 + R^2 - 2aR\cos(\pi-\theta) = a^2\left[1 + \left(\frac{R}{a}\right)^2 + 2\frac{R}{a}\cos\theta\right]\end{aligned} \tag{A.4}$$

where we have used the fact that $\cos(\pi-\theta) = -\cos\theta$. Plugging these expressions in:

$$\begin{aligned}\vec{\tau}_1 &= \frac{GM_p m_1 Ra\sin\theta}{a^3\left[1 + \left(\frac{R}{a}\right)^2 - 2\frac{R}{a}\cos\theta\right]^{3/2}}\hat{\jmath}\\ \vec{\tau}_2 &= -\frac{GM_p m_2 Ra\sin\theta}{a^3\left[1 + \left(\frac{R}{a}\right)^2 + 2\frac{R}{a}\cos\theta\right]^{3/2}}\hat{\jmath}\end{aligned} \tag{A.5}$$

In the limit that $R \ll a$, we can use the following approximations:

$$\begin{aligned}f(x) &= \left(1 + x^2 + ax\right)^{-3/2}; f(0) = 1\\ f'(x) &= -\frac{3}{2}\left(1 + x^2 + ax\right)^{-5/2}(2x + a); f'(0) = -\frac{3}{2}a\\ f(x) &\approx 1 - \frac{3}{2}ax\end{aligned} \tag{A.6}$$

which leads to:

$$\begin{aligned}
\vec{\tau}_1 &= \frac{GM_p}{a^3} m_1 Ra \sin\theta \left[1 - \frac{3}{2}\left(-2\cos\theta\right)\frac{R}{a}\right]\hat{\jmath} \\
&= n^2 m_1 Ra \sin\theta \left(1 + 3\cos\theta\frac{R}{a}\right)\hat{\jmath} \\
\vec{\tau}_2 &= -\frac{GM_p}{a^3} m_2 Ra \sin\theta \left[1 - \frac{3}{2}\left(2\cos\theta\right)\frac{R}{a}\right]\hat{\jmath} \\
&= n^2 m_2 Ra \sin\theta \left(1 - 3\cos\theta\frac{R}{a}\right)\hat{\jmath}
\end{aligned} \tag{A.7}$$

Remembering that $(m_1 + m_2)R^2 = C - A$, the net torque $\vec{\tau} = \vec{\tau}_1 + \vec{\tau}_2$ is:

$$\vec{\tau} = 3n^2\left(m_1 + m_2\right)R^2 \sin\theta\cos\theta\hat{\jmath}$$

$$\vec{\tau} = 3n^2\left(C - A\right)\sin\theta\cos\theta\hat{\jmath} \tag{A.8}$$

The torque changes the direction of the spin angular momentum vector:

$$\begin{aligned}
\frac{d\vec{\alpha}}{dt} &= \vec{\tau} = 3n^2\left(C - A\right)\sin\theta\cos\theta\hat{\jmath} \\
C\omega\frac{d\hat{s}}{dt} &= 3n^2\left(C - A\right)\sin\theta\cos\theta\hat{\jmath} \\
\frac{d\hat{s}}{dt} &= 3\frac{n^2}{\omega}\frac{C - A}{C}\sin\theta\cos\theta\hat{\jmath}
\end{aligned} \tag{A.9}$$

The precession rate is $\omega_p = 2\pi/P$ where P is the precession period. The spin axis traces a circle of radius $2\pi\sin\theta$ in time $P = 2\pi\sin\theta/|\frac{d\hat{s}}{dt}|$ (Harris and Ward, 1982). Therefore

$$\omega_p = \frac{2\pi|\frac{d\hat{s}}{dt}|}{2\pi\sin\theta} = 3\frac{n^2}{\omega}\frac{C - A}{C}\cos\theta \tag{A.10}$$

This is very close to the actual expressions:

$$\frac{d\hat{s}}{dt} = \frac{3}{2}\frac{n^2}{\omega}\frac{C - A}{C}\left(\hat{n}\cdot\hat{s}\right)\left(\hat{n}\times\hat{s}\right) \tag{A.11}$$

$$\omega_p = \frac{3}{2}\frac{n^2}{\omega}\frac{C - A}{C}\cos\theta \tag{A.12}$$

See the next section for more details on where the actual axial precession equations come from.

A.3 Precessional torques – axial precession

Whenever the spin axis of a body is misaligned from the orbit normal, there will be rigid body precession about the orbit normal. The part of a body that responds rigidly to forces is called the permanent deformation or permanent figure. This is opposed to the tidal deformation that generates friction when it is torqued because it is responding to the changing tidal potential but with a lag. Here is a description of how ten different works present axial precession due to torques on the permanent figure. There are broadly two routes: 1) start with a Hamiltonian with the rotational kinetic and potential energies or the disturbing function 2) start with the instantaneous torque on the body. I've included derivations for axially symmetric planets ($B = A, C - A = J_2 M R^2$) and for triaxial synchronous satellites ($B - A \neq 0, C - A = (J_2 + 2C_{22}) M R^2$). I've included a paper if it a) shows a different method for deriving the precession rate b) has a useful graphic c) includes an effect that is often ignored. I have not included the effect of equatorial satellites on the spin precession of a planet, and I refer the reader to Ward (1975b) and Ward and Hamilton (2004) for a discussion of how to treat that problem.

Colombo (1966): This work takes the instantaneous torque on an axially symmetric planet ($B = A$) and averages it over one orbit period to get the canonical

expression, their Eq. (8'):

$$\vec{\tau} = \frac{3}{2}\frac{n^2}{(1-e^2)^{3/2}}(C-A)(\hat{s}\cdot\hat{n})(\hat{s}\times\hat{n})$$

In the reference frame of the precessing orbit, the spin angular momentum changes by

$$C\omega\left(\frac{d\hat{s}}{dt} + \dot{\Omega}\hat{k}\times\hat{s}\right) = \vec{\tau}$$

Which becomes their Eq. (12), how the spin axis changes because of torques on the figure in the precessing reference frame:

$$\frac{d\hat{s}}{dt} = -\dot{\Omega}\hat{k}\times\hat{s} + \frac{3}{2}\frac{n^2}{\omega}\frac{1}{(1-e^2)^{3/2}}\frac{C-A}{C}(\hat{s}\cdot\hat{n})(\hat{s}\times\hat{n})$$

Note that this expression is not appropriate for triaxial satellites.

Goldreich (1966): Section 2 of this paper derives the precessional torques among the Earth, Sun, and Moon starting with the disturbing potential for each interaction. For example, the time-averaged potential energy per unit mass for the effect of the Sun on the Earth's figure is (their Eq. 14):

$$\tilde{R_3} = \frac{2}{3}\frac{GM}{a^3}J_2R^2\left(\frac{1}{2} - \frac{3}{4}\sin^2\gamma\right)$$

To get the torque, differentiate the potential per unit mass by the angle of interest (which in this case is the Earth's obliquity γ) and multiply by the other mass (the Sun's mass M_s). The direction of the torque is perpendicular to the two vectors that form the angle, $\hat{a}$ the Earth's spin axis and $\hat{c}$ the ecliptic normal:

$$L_3 = -\frac{GM_SM}{a^3}J_2R^2\sin\gamma\cos\gamma\frac{\hat{a}\times\hat{c}}{|\hat{a}\times\hat{c}|}$$

Since $\sin\gamma = |\hat{a} \times \hat{c}|$,

$$L_3 = -\frac{GM_S M}{a^3} J_2 R^2 (\hat{a} \cdot \hat{c})(\hat{a} \times \hat{c})$$

which is their Eq. 17. Because all of the disturbing potentials have a term with sine-squared, the resulting derivatives and functional forms of the torque have a dot product and cross product of the vectors involved.

Peale (1969): Builds on Colombo (1966) by including axial asymmetry and arbitrary spin-orbit resonances "from a more easily understood point of view." The Cassini state relation in their Eq. (18) is found by using a time-averaged Hamiltonian to get the path the spin axis would trace on the unit sphere. Equilibrium is reached when the constant of the motion is tangential to the unit sphere, at which point the spin axis will remain fixed.

Harris & Ward (1982): The instantaneous rate of change of the spin axis, their Eq. (3.5) is:

$$\frac{d\hat{s}}{dt} = -\alpha \sin 2\phi \frac{\hat{r} \times \hat{s}}{|\hat{r} \times \hat{s}|}$$

where $\hat{r}$ is the unit vector connecting the centers of mass, ϕ is the angle between $\hat{s}$ and $\hat{r}$, and $\alpha = \frac{J_2}{c}\frac{n^2}{\omega}$. They say that ϕ has a maximum of θ at solstice and a minimum of 0 at equinox, which I have difficulty seeing. For $\phi = \theta$ at solstice, this functional form is very similar to the rough derivation in the previous section of this document. Averaging over an orbit yields their Eq. (3.7):

$$\frac{d\hat{s}}{dt} = -\alpha(\hat{n} \cdot \hat{s})(\hat{n} \times \hat{s})$$

Problems:

- They may be missing a factor of 3/2 in their definition of α.
- They predict clockwise precession about the orbit normal, although their Fig. 2 shows counterclockwise precession.

Jankowski et al. (1989): This is a companion paper to Chyba et al. (1989), and like Peale (1969) and Ward (1975b), they only provide the Cassini state relation. They take the approach of finding the intersection of the Hamiltonian in the form of a parabolic cylinder with the unit sphere to find the path the spin axis would take. What is useful for satellites with large obliquity is that they include obliquity corrections for J_2 and C_{22}.

Gladman et al. (1996): Their Appendix A derives the equations of motion for the spin vector of a body with torques on the permanent figure, tidal torques, and the effect of the precessing reference frame. Their section 7.1 works through the solid-body torque starting with MacCullagh's formula and averaging it over an orbital and a rotational period. The averaged torque in the direction $(\hat{n} \times \hat{s})/\sin\theta$ neglecting terms associated with non-synchronous rotation is (a modified version of their Eq. 40):

$$\vec{\tau} \cdot \hat{y} = -\frac{3}{8} n^2 (B - A) \sin\theta (1 + \cos\theta) - \frac{3}{2} n^2 \left(C - \frac{A + B}{2} \right) \sin\theta \cos\theta$$

This term is negative because the spin axis precesses clockwise about the orbit normal. The equations of motion are then:

$$\frac{d\hat{s}}{dt} = -\frac{3}{2} n^2 \left[(J_2 + C_{22}) \cos\theta + C_{22} \right] (\hat{n} \times \hat{s})$$

which is a modified version of their Eq. (42).

Ward and Hamilton (2004): This paper presents the same equation of motion of the spin vector (their Eq. 6) as in Colombo (1966) along with the Cassini state relation (their Eq. 8) all for an axially symmetric planet. Their Figure 1 shows a useful cartoon of the spin axis and orbit precessions for Cassini states 1 and 2.

Bills (2005): This paper has a good discussion on the different averaging procedures to get the precession of the spin axis for fast rotators and synchronous rotators. For a rapidly rotating body, their Eq. (1) is the same as in Colombo (1966):

$$\frac{d\hat{s}}{dt} = \frac{3}{2}\frac{J_2}{c}\frac{n^2}{\omega}\frac{1}{(1-e^2)^{3/2}}(\hat{n}\cdot\hat{s})(\hat{s}\times\hat{n})$$

For a synchronous rotator, neglecting the eccentricity terms, their Eqs. (5), (22), and (23) become:

$$\frac{d\hat{s}}{dt} = \frac{3}{2}\frac{n^2}{\omega}\left[(J_2 + C_{22})(\hat{n}\cdot\hat{s}) - C_{22}\right](\hat{s}\times\hat{n})$$

Problems:

- The second C_{22} term is supposed to be the same sign as the first term and positive. The same problem appears in Bills & Comstock (2005). This is corrected in Siegler et al. (2011).

Bills & Nimmo (2011): This work lays out the Cartesian equations of motion for the spin vector. *Problems:*

- Typo in their Eq. (7): to make their Eq. (6) work out, $\beta = \frac{3}{2}\frac{n}{c}C_{22}$, so their β is too small by a factor of 1/2.

- Typo in their Eqs. (6) and (8): It should be $(\hat{s} \times \hat{n})$ not $(\hat{n} \times \hat{s})$. This leads to being off by a minus sign.

Siegler et al. (2011): Their Figure 4 is particularly helpful for visualizing the motion of the spin axis about the orbit normal as the orbit normal precesses about the Laplace plane normal both in and not in a Cassini state. *Problems:*

- Their Fig. 4 shows counterclockwise nodal precession when it should be clockwise.
- The spin axis precession terms are off by a minus sign. Either their Eq. (1) should be $(\hat{n} \times \hat{s})$ not $(\hat{s} \times \hat{n})$ or α and β in their Eq. (2) should be positive not negative.

A.4 Precessional torques – orbital precession

The orbit plane of a satellite will precess like a wobbling plate if it is inclined with respect to a reference plane. This reference plane is the Laplace plane, which has little definition other than the average orbital plane, the zero-inclination plane, or the plane in which no orbital precession would occur. Here I will share some equations and derivations for calculating the precession of the ascending node or nodal precession. I will consider torques that the planet's oblateness and the Sun exert on the satellite's orbit, but there are also satellite-satellite interactions that are described in Noyelles (2009) for example. While the planet and Sun exert torques, they do not change the z-component of the angular momentum, just a steady change in the planar angular momentum hence the precession.

A.4.1 Orbital precession due to the planet

Eq. 34 in Chen and Nimmo (2016) and Eq. 6 in Ward (1975a) contain the equation for how a planet's oblateness, quantified by $J_{2,p}$, causes precession of the node. Murray and Dermott (1999) derive the equation Eq. 6.250 from the disturbing function due to an oblate central planet and include terms with $J_{2,p}^2$ and J_4 as well. I will not show this derivation, just the equation itself in the form that it is used.

$$\frac{d\Omega}{dt} = -\frac{3}{2} n J_{2,p} \left(\frac{R_p}{a} \right)^2$$

A.4.2 Orbital precession due to the Sun

In Section 6.8 of Murray and Dermott (1999), Lagrange's planetary equations are given, which are the variations in the elements of a perturbed body. These equations depend on partial derivatives of the disturbing function R, which is described in Section 6.7. The equation for how the longitude of the ascending node varies is Eq. 6.148:

$$\frac{d\Omega}{dt} = \frac{1}{na^2\sqrt{1-e^2}\sin I} \frac{\partial R}{\partial I}$$

Note that I is the inclination. Here I will focus on the effect of an external body on an inner body so that at the end we can show how the Sun contributes to the Moon's nodal precession. The disturbing potential acting on an inner body due to an external body is (Eq. 6.44 & 6.134):

$$R = \frac{\mu'}{a'} \left(R_D + \alpha R_E \right)$$

where α is now the ratio of the outer body's semi-major axis to the inner body's. We first need to time-average the disturbing potential which amounts to ignoring all terms

that are rapidly varying. The arguments in the cosines of R include a combination of $\lambda, \lambda', \varpi, \varpi', \Omega,$ and Ω'. The mean longitudes λ and λ' increase with n, so they are rapidly varying. Therefore, the long period or secular terms do not involve λ or λ', and eliminating them can be achieved by setting $j = 0$ for $\cos(...j\lambda - j\lambda' + \cdots)$. There are no terms without λ or λ' in R_E, so $\langle R_E \rangle = 0$.

$$\langle R \rangle = \frac{\mu'}{a'} \langle R_D \rangle$$

Setting $j = 0$ in Eq. 6.107:

$$\langle R_D \rangle = c_0 + c_1(e^2 + e'^2) + c_2(s^2 + s'^2) + c_3 ee' \cos(\varpi' - \varpi) + c_4 ss' \cos(\Omega' - \Omega)$$

where $s = \sin \frac{I}{2}$ and $s' = \sin \frac{I'}{2}$ and the constants are:

$$\begin{aligned}
c_0 &= \frac{1}{2} b_{1/2}^{(0)}(\alpha) \\
c_1 &= \frac{1}{8} \left[2aD + \alpha^2 D^2 \right] b_{1/2}^{(0)}(\alpha) \\
c_2 &= -\frac{1}{2} \alpha b_{3/2}^{(1)}(\alpha) \\
c_3 &= \frac{1}{4} \left[2 - 2aD - \alpha^2 D^2 \right] b_{1/2}^{(1)}(\alpha) \\
c_4 &= \alpha b_{3/2}^{(1)}(\alpha)
\end{aligned}$$

where $b_s^{(j)}(\alpha)$ are Laplace coefficients defined in Eq. 6.67 and D is the derivative operator $d/d\alpha$ defined in Eq. 6.70. Taking the partial derivative of $\langle R_D \rangle$ with respect to I

$$\frac{\partial \langle R_D \rangle}{\partial I} = 2c_2 \frac{1}{2} \sin \frac{I}{2} \cos \frac{I}{2} + \frac{1}{2} c_4 \cos \frac{I}{2} \sin \frac{I'}{2} \cos(\Omega' - \Omega)$$

Using the identity $\sin I = 2 \sin \frac{I}{2} \cos \frac{I}{2}$

$$\frac{\partial \langle R_D \rangle}{\partial I} = \frac{1}{2} c_2 \sin I + \frac{1}{4} c_4 \sin I \frac{s'}{s} \cos(\Omega' - \Omega)$$

We'll now circle back to the Lagrange planetary equation for the node:

$$\frac{d\Omega}{dt} = \frac{1}{na^2\sqrt{1-e^2}\sin I}\frac{\partial\langle R\rangle}{\partial I}$$
$$\frac{d\Omega}{dt} = \frac{1}{na^2\sqrt{1-e^2}\sin I}\frac{\mu'}{a'}\frac{\partial\langle R_D\rangle}{\partial I}$$
$$\frac{d\Omega}{dt} = \frac{1}{na^2\sqrt{1-e^2}\sin I}\frac{\mu'}{a'}\left[\frac{1}{2}c_2\sin I + \frac{1}{4}c_4\sin I\frac{s'}{s}\cos(\Omega'-\Omega)\right]$$

We can substitute $\mu' = Gm' = \frac{n^2a^3}{M_c}m'$, M_c being the central mass:

$$\frac{d\Omega}{dt} = \frac{n^2a^3m'}{na^2a'M_c\sqrt{1-e^2}\sin I}\left[\frac{1}{2}c_2\sin I + \frac{1}{4}c_4\sin I\frac{s'}{s}\cos(\Omega'-\Omega)\right]$$

Simplifying the terms with inclination:

$$\frac{d\Omega}{dt} = n\frac{a}{a'}\frac{m'}{M_c}\frac{1}{\sqrt{1-e^2}}\left[\frac{1}{2}c_2 + \frac{1}{4}c_4\frac{s'}{s}\cos(\Omega'-\Omega)\right]$$

Expanding out the constants:

$$\frac{d\Omega}{dt} = n\alpha\frac{m'}{M_c}\frac{1}{\sqrt{1-e^2}}\left[-\frac{1}{4}\alpha b^{(1)}_{3/2}(\alpha) + \frac{1}{4}\alpha b^{(1)}_{3/2}(\alpha)\frac{s'}{s}\cos(\Omega'-\Omega)\right]$$

Here it appears that the second term must average to zero, either because Ω' is fixed while Ω varies or because Ω' varies as well non-resonantly. We're left with:

$$\frac{d\Omega}{dt} = -\frac{1}{4}n\alpha^2\frac{m'}{M_c}\frac{1}{\sqrt{1-e^2}}b^{(1)}_{3/2}(\alpha)$$

Neglecting 2nd-order terms in eccentricity:

$$\frac{d\Omega}{dt} = -\frac{1}{4}n\alpha^2\frac{m'}{M_c}b^{(1)}_{3/2}(\alpha)$$

We'll look at this equation in the context of the Sun perturbing the orbit of the Moon. In this case, $\alpha \ll 1$, so we can take a Taylor expansion of the Laplace coefficient (e.g.,

Burns et al., 1979).

$$b_{3/2}^{(1)}(\alpha) \approx b_{3/2}^{(1)}(0) + Db_{3/2}^{(1)}(0)\alpha$$
$$\approx b_{3/2}^{(1)}(0) + \frac{3}{2}\left[b_{5/2}^{(0)}(0) - 2\alpha b_{5/2}^{(1)}(0) + b_{5/2}^{(2)}(0)\right]\alpha$$

We can evaluate the Laplace coefficients at $\alpha = 0$.

$$b_s^{(j)}(\alpha) = \frac{2}{\pi}\int_0^\pi \frac{\cos(j\theta)d\theta}{(1+\alpha^2 - 2\alpha\cos\theta)^s}$$
$$b_s^{(j)}(0) = \frac{2}{\pi}\int_0^\pi \cos(j\theta)d\theta$$

This integral is zero except for when $j = 0$.

$$b_s^{(0)}(0) = \frac{2}{\pi}\int_0^\pi d\theta = \frac{2}{\pi}\pi = 2$$

This is a surprisingly simple result.

$$b_{3/2}^{(1)}(\alpha) \approx 0 + \frac{3}{2}(2 - 0 - 0)\alpha = 3\alpha$$

Going back to the equation derived from the disturbing function, the Sun causes the Moon's node to regress at a rate:

$$\dot{\Omega}_S = -\frac{1}{4}n\alpha^2\frac{M_S}{M_E}(3\alpha)$$
$$\dot{\Omega}_S = -\frac{3}{4}n\frac{M_S}{M_E}\left(\frac{a}{a_E}\right)^3$$

This is a much simpler equation to use when possible because it avoids having to calculate the Laplace coefficients.

Both equations for the nodal precession can be found in the literature. Examples for the first include Burns et al. (1979), Yseboodt and Margot (2006), and Noyelles (2009). Examples for the second include Ward (1975a) and Chen and Nimmo (2016).

There are three deviations from these equations that include $\cos\beta$. For Murray and Dermott (1999) at the end of Section 6, β is the angle between the satellite's orbit and the planet's orbit. In Goldreich (1966), it is presumably the same angle, the angle between the Moon's orbit and the Sun (the Earth's orbit plane). In Ćuk et al. (2016b) it is the Moon's orbital inclination.

A.5 Derivation of how the tidal torque affects the obliquity and spin rate of a satellite

Key references: Goldreich and Peale (1970); Ward (1975b); Gladman et al. (1996).

The spin angular momentum $\alpha\hat{s} = nC\hat{s}$ changes because of torques on the satellite, $\vec{\tau}$, e.g., Eq. 15 of Goldreich and Peale (1970), which will be referred to as GP70 from here on out:

$$\frac{d(\alpha\hat{s})}{dt} + \dot{\Omega}\alpha(\hat{k}\times\hat{s}) = \vec{\tau} \tag{A.13}$$

The first term is the rate of change of the direction and magnitude of the spin angular momentum, and the second term is the precessing reference frame, the precessional motion of the spin axis about the Laplace plane normal $\hat{k}$ at a frequency $\dot{\Omega}$.

Here we will focus on the torque exerted on the tidal bulge as opposed to the torque on the permanent figure in the previous section. Gladman et al. (1996) (G+96) derive the orbit-averaged tidal torque in Eq. 48:

$$\vec{\tau}_{\rm tid} = -\frac{CT}{2}\left[(\omega\cos\theta - 2n)\hat{n} + \omega\hat{s}\right] \tag{A.14}$$

GP70 and Ward (1975b) (W75) do not give the expression for the tidal torque $\vec{\tau}_{\rm tid}$ but allude to its functional form. The factor T is very common and is defined as (Eq. 49 of G+96):

$$T = 3n\frac{k_2}{Q}\left(\frac{R}{a}\right)^3 \frac{M_p R^2}{C}$$

I assumed that for synchronous satellites $\Delta t = 1/(nQ)$. To relate the factor in Eq. 11 of W75, $T = 1/\tau$. Mind the typo in W75; there is a missing extra factor of M_p in the definition for $1/\tau$. W75 include an extra factor of $\frac{1}{2}$ in $1/\tau$ presumably because of the tidal model to relate Δt to $1/Q$. To relate the factor in GP70, $T = F$.

A common methodology in all of these papers is to find two equations of motion related to the change in the spin angular momentum $\alpha\hat{s}$:

1) Changes in magnitude from $\vec{\tau}_{\rm tid} \cdot \hat{s}$: affects the spin rate ω.

2) Changes in direction from $\vec{\tau}_{\rm tid} \cdot \hat{n}$: affects the spin axis $\hat{s}$.

Note that the precessional term is always zero when taking the dot product of it with $\hat{s}$ and $\hat{n}$.

Finding $d\omega/dt$ from the torque aligned with the spin axis

Changing the rotation rate of a body requires a torque along its rotation axis, so to find $d\omega/dt$, take the component of $\vec{\tau}_{\rm tid}$ along $\hat{s}$.

$$\begin{aligned}
\frac{d(\alpha\hat{s})}{dt} \cdot \hat{s} &= \vec{\tau}_{\rm tid} \cdot \hat{s} \\
\frac{d\alpha}{dt} &= -\frac{CT}{2}[(\omega\cos\theta - 2n)\cos\theta + \omega] \\
\frac{d\omega}{dt} &= -\frac{T}{2}[(\omega\cos\theta - 2n)\cos\theta + \omega] \qquad \text{(A.15)}
\end{aligned}$$

Eq. A.15 is the same as Eq. 10 in W75. The expression for $d\alpha/dt$ matches Eq. 50 of G+96. Furthermore, Eq. A.15 matches the tidal term for $d\omega/dt$ in Eq. 52 of G+96.

Finding $d\theta/dt$ from the torque aligned with the orbit normal

One way to think about changes in the obliquity is to start with your spin axis pointed in one direction and then to add or subtract a component along $\hat{n}$. Positive torque along $\hat{n}$ means the spin axis will be aligned more with the orbit normal (smaller obliquity), and a negative torque along $\hat{n}$ means the spin axis will be driven away from the orbit normal (larger obliquity). Historically, GP70 and G+96 found their equations of motion for the obliquity by taking the dot product of Eq. A.13 with respect to $\hat{n}$.

$$\begin{aligned}
\frac{d(\alpha\hat{s})}{dt} \cdot \hat{n} &= \vec{\tau}_{\rm tid} \cdot \hat{n} \\
\frac{d(\alpha\cos\theta)}{dt} &= \alpha\frac{d\cos\theta}{dt} + \cos\theta\frac{d\alpha}{dt} = \vec{\tau}_{\rm tid} \cdot \hat{n} \\
\frac{d\cos\theta}{dt} &= \frac{1}{\alpha}\vec{\tau}_{\rm tid} \cdot \hat{n} - \frac{\cos\theta}{\alpha}\frac{d\alpha}{dt}
\end{aligned}$$

In GP70, they recognize that $d\alpha/dt = \vec{\tau}_{\rm tid} \cdot \hat{s}$:

$$\frac{d\cos\theta}{dt} = \frac{1}{\alpha}\vec{\tau}_{\rm tid} \cdot \hat{n} - \frac{\cos\theta}{\alpha}\vec{\tau}_{\rm tid} \cdot \hat{s}$$

This is where Eq. 17 of GP70 comes from, which is the following:

$$\frac{d\cos\theta}{dt} = (\hat{n} - \cos\theta\hat{s}) \cdot \frac{\vec{\tau}_{\rm tid}}{\alpha}$$

The vector $\hat{n} - \cos\theta\hat{s} = \sin\theta\hat{e}$ is perpendicular to $\hat{s}$, such that the vector $\hat{e}$ points from $\hat{s}$ to $\hat{n}$ (see Figure A.2). Together they form a right triangle with $\hat{n}$ along the hypotenuse. Therefore, we can see that the component of the tidal torque along $\hat{e}$ is what is responsible for decreasing the obliquity and driving the spin axis towards the orbit normal. GP70 call this perpendicular component of the torque $\tau_\perp$ such that $d\cos\theta/dt = \sin\theta\tau_\perp/\alpha$ (Eq. 17).

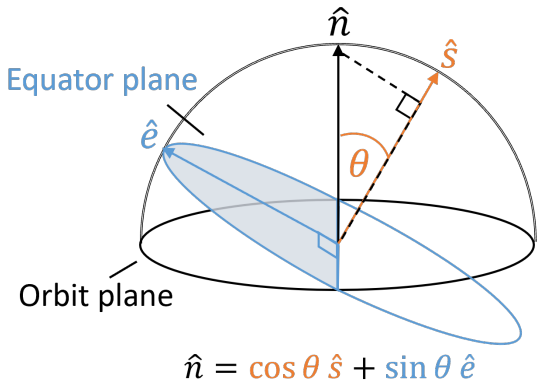

Figure A.2: The geometry of the spin axis, orbit normal, and vector in the equator plane perpendicular to the spin axis.

Another way to go about this is to find $\vec{\tau}_{\rm tid} \cdot \hat{n}$ from Eq. A.14, which is Eq. 51 in G+96:

$$\vec{\tau}_{\rm tid} \cdot \hat{n} = -\frac{CT}{\alpha}(\omega\cos\theta - n)$$

Starting with our equation of motion for the obliquity

$$\frac{d\cos\theta}{dt} = -\frac{\cos\theta}{\alpha}\frac{d\alpha}{dt} + \frac{1}{\alpha}\vec{\tau}_{\rm tid}\cdot\hat{n}$$

we get

$$\begin{aligned}
\frac{d\cos\theta}{dt} &= \frac{\cos\theta}{\alpha}\frac{CT}{2}[(\omega\cos\theta - 2n)\cos\theta + \omega] - \frac{CT}{\alpha}(\omega\cos\theta - n) \\
\frac{d\cos\theta}{dt} &= \frac{T}{\omega}\left(\frac{1}{2}\omega\cos^3\theta - n\cos^2\theta - \frac{1}{2}\omega\cos\theta + n\right) \\
\frac{d\cos\theta}{dt} &= \frac{T}{\omega}\left[\frac{1}{2}\omega\cos\theta(\cos^2\theta - 1) - n(\cos^2\theta - 1)\right] \\
\frac{d\cos\theta}{dt} &= \sin^2\theta T\left(\frac{n}{\omega} - \frac{1}{2}\cos\theta\right)
\end{aligned} \tag{A.16}$$

This equation of motion for the obliquity, Eq. A.16 matches Eq. 19 in GP70. The following expression for $d\theta/dt$ matches W75 Eq. 13 and the tidal component of G+96 Eq. 53:

$$\begin{aligned}
-\sin\theta\frac{d\theta}{dt} &= \sin^2\theta\, T\left(\frac{n}{\omega} - \frac{1}{2}\cos\theta\right) \\
\frac{d\theta}{dt} &= -\sin\theta\, T\left(\frac{n}{\omega} - \frac{1}{2}\cos\theta\right)
\end{aligned} \tag{A.17}$$

Finding $d\hat{s}/dt$

This is a very similar derivation as the one for $d\theta/dt$ but shows explicitly that $d\hat{s}/dt$ is along $\hat{e}$. Assuming that only the tidal torque changes the spin angular

momentum and not torques on the permanent figure:

$$\begin{aligned}\frac{d(\alpha\hat{s})}{dt} &= \vec{\tau}_{\rm tid} \\ \alpha\frac{d\hat{s}}{dt} + \hat{s}\frac{d\alpha}{dt} &= \vec{\tau}_{\rm tid} \\ \frac{d\hat{s}}{dt} &= -\frac{1}{\alpha}\frac{d\alpha}{dt}\hat{s} + \frac{1}{\alpha}\vec{\tau}_{\rm tid}\end{aligned}$$

Substituting in $d\alpha/dt$:

$$\begin{aligned}\frac{d\hat{s}}{dt} &= \frac{1}{\alpha}\frac{CT}{2}[(\omega\cos\theta - 2n)\cos\theta + \omega]\hat{s} - \frac{1}{\alpha}\frac{CT}{2}[(\omega\cos\theta - 2n)\hat{n} + \omega\hat{s}] \\ \frac{d\hat{s}}{dt} &= -\frac{1}{\alpha}\frac{CT}{2}(\omega\cos\theta - 2n)(\hat{n} - \cos\theta\hat{s}) \\ \frac{d\hat{s}}{dt} &= T\left(\frac{n}{\omega} - \frac{1}{2}\cos\theta\right)(\hat{n} - \cos\theta\hat{s}) \\ \frac{d\hat{s}}{dt} &= T\left(\frac{n}{\omega} - \frac{1}{2}\cos\theta\right)\sin\theta\hat{e}\end{aligned} \tag{A.18}$$

Eq. A.18 corroborates that the direction of the rate of change of the spin axis is along $\hat{e}$. The expression matches Eq. 9 of W75. We could have also gotten Eq. A.18 by taking the component of $\vec{\tau}_{\rm tid}$ along $\hat{e}$ to begin with.

$$\begin{aligned}\frac{d\hat{s}}{dt} &= \frac{1}{\alpha}(\vec{\tau}_{\rm tid}\cdot\hat{e})\hat{e} \\ \frac{d\hat{s}}{dt} &= \frac{1}{C\omega}\left\{-\frac{CT}{2}\left[(\omega\cos\theta - 2n)\hat{n} + \omega\hat{s}\right]\cdot\hat{e}\right\}\hat{e} \\ \frac{d\hat{s}}{dt} &= T\left(\frac{n}{\omega} - \frac{1}{2}\cos\theta\right)\sin\theta\hat{e}\end{aligned}$$

This simpler route is the one taken in my Titan manuscript.

A.6 Using the spherical spin equations of motion to find the equilibrium spin state.

The equilibrium spin state can be found by finding the steady-state solution to the equations of motion. A derivation using Cartesian coordinates is in my Titan manuscript, so here I will present an alternative which is to use spherical coordinates.

Appendix A of Gladman et al. (1996) derives the full spin equations of motion for a body due to torques on the permanent deformation and the tidal bulge. The previous section only derived two spin equations of motion due to the tidal torque for ω and θ. Gladman et al. (1996) includes torques on the permanent figure and the orbit precession, which introduces a third variable, the azimuth ϕ of the spin axis projected onto the orbit plane. Because of how they define their coordinate system (the Cassini plane is the $\hat{J} - \hat{K}$ plane) and the fact that a positive azimuth corresponds to Cassini state 1, their azimuth is the angle away from the $-\hat{J}$ axis going towards the $\hat{I}$ axis. However, to be consistent with my preference for having the Cassini plane be the $\hat{Z} - \hat{X}$ plane and having ϕ be the angle off the $\hat{X}$ axis towards $\hat{Y}$, this means that Gladman et al. (1996)'s azimuth is really $\phi + \pi = \phi_\pi$. This means that all sinusoids with ϕ_π become negative when changing to ϕ. They also do not assume synchronous rotation, which introduces the angle ψ_0, a measure of how closely the A-axis of the satellite is pointing towards the planet. The orbit-averaged equations of motion are equations

(52-54) in Appendix A of Gladman et al. (1996):

$$\frac{d\omega}{dt} = -T\left[\omega\left(1 - \frac{1}{2}\sin^2\theta\right) - n\cos\theta\right] - R(1+\cos\theta)^2\sin 2\psi_0$$
$$\frac{d\theta}{dt} = -\dot{\Omega}\sin i\sin\phi_\pi + T\sin\theta\left(\frac{1}{2}\cos\theta - \frac{n}{\omega}\right) + \frac{R}{\omega}\sin\theta\,(1+\cos\theta)\sin 2\psi_0$$
$$\frac{d\phi_\pi}{dt} = -\dot{\Omega}\left[(\sin i\cot\theta\cos\phi_\pi + \cos i) - \frac{S}{\omega}\cos\theta - \frac{R}{\omega}\,(1+\cos\theta)\cos 2\psi_0\right.$$

The angular accelerations due to the body's triaxiality and oblateness are R and S, and the tidal deceleration rate is ωT:

$$R = \frac{3GM_p}{8a^3}\frac{B-A}{C} = \frac{3}{2}n^2\frac{C_{22}}{c}$$
$$S = \frac{3GM_p}{2a^3}\frac{C-(B+A)/2}{C} = \frac{3}{2}n^2\frac{J_2}{c}$$
$$T = \frac{3k_2GM_p^2R^5}{Ca^6}\Delta t = 3n\left(\frac{M_p}{M}\right)\left(\frac{R}{a}\right)^3\frac{k_2}{Q}\frac{1}{c}$$

Some interesting observations:

- $d\phi_\pi/dt$ contains no tidal torque term, which means that the azimuth changes solely because of the orbit precession and torques on the figure (S and R). In fact, for $\psi_0 \approx 0$, figure torques appear in only this equation of motion. Steady state is reached when the orbit and figure precession terms balance.

- The obliquity has a tidal torque term and an orbit precession term. Without the orbit precession term, $d\theta/dt$ would always be negative and would stop at $\theta = 0$. With the orbit precession term, the obliquity is balanced at non-zero obliquity.

- Non-synchronous rotation (i.e., $\psi_0 \neq 0$) is always part of the R ($B - A$ torque) term which makes sense since this torque vanishes for purely synchronous rotation and the A-axis pointing towards the planet.

Steady-state solution for ω, θ, and ϕ

We assume synchronous rotation in the following derivations, so $\psi_0 \approx 0$, $\sin 2\psi_0 \approx 0$ and $\cos 2\psi_0 \approx 1$. We'll simplify to $\omega = n$ at the end.

(1) $d\omega/dt = 0$

$$
\begin{aligned}
-T\left[\omega\left(1-\frac{1}{2}\sin^2\theta\right)-n\cos\theta\right] &= R(1+\cos\theta)^2\sin 2\psi_0 \\
\omega\left(1-\frac{1}{2}\sin^2\theta\right) &= n\cos\theta - \frac{R}{T}(1+\cos\theta)^2\sin 2\psi_0 \\
\frac{\omega}{n} &= \frac{2\cos\theta}{1+\cos^2\theta} - \frac{2R}{nT}\frac{(1+\cos\theta)^2}{1+\cos^2\theta}\sin 2\psi_0
\end{aligned}
$$

If the satellite is close enough to synchronous rotation where $\frac{2R}{nT}\sin 2\psi_0 \ll 1$, then

$$\frac{\omega}{n} \approx \frac{2\cos\theta}{1+\cos^2\theta} \tag{A.19}$$

For small θ, $\cos\theta \sim 1-\theta^2/2$ and $\cos^2\theta \sim \left(1-\frac{\theta^2}{2}\right)^2 \sim 1-\theta^2$, so

$$\frac{\omega}{n} \approx \frac{2-\theta^2}{1+1-\theta^2} \approx 1 \tag{A.20}$$

(2) $d\theta/dt = 0$

$$
\begin{aligned}
-\dot{\Omega}\sin i\sin\phi_\pi &= -T\sin\theta\left(\frac{1}{2}\cos\theta-\frac{n}{\omega}\right)-\frac{R}{\omega}\sin\theta(1+\cos\theta)\sin 2\psi_0 \\
-\dot{\Omega}\sin i\sin\phi_\pi &= T\sin\theta\left(\frac{n}{\omega}-\frac{1}{2}\cos\theta\right) \\
\sin\phi_\pi &= -T\frac{\sin\theta}{\dot{\Omega}\sin i}\left(\frac{n}{\omega}-\frac{1}{2}\cos\theta\right) \\
\sin\phi &= T\frac{\sin\theta}{\dot{\Omega}\sin i}\left(\frac{n}{\omega}-\frac{1}{2}\cos\theta\right)
\end{aligned} \tag{A.21}
$$

(3) $d\phi_\pi/dt = 0$

$$
\begin{aligned}
-\dot{\Omega}(\sin i \cot\theta \cos\phi_\pi + \cos i) &= \frac{S}{\omega}\cos\theta + \frac{R}{\omega}(1+\cos\theta)\cos 2\psi_0 \\
-\dot{\Omega}\sin i \cot\theta \cos\phi_\pi &\approx \dot{\Omega}\cos i + \frac{1}{\omega}[(S+R)\cos\theta + R] \\
-\dot{\Omega}\sin i \cos\phi_\pi &\approx \tan\theta\left\{\dot{\Omega}\cos i + \frac{1}{\omega}[(S+R)\cos\theta + R]\right\} \\
\cos\phi_\pi &\approx -\frac{\tan\theta}{\dot{\Omega}\sin i}\left\{\dot{\Omega}\cos i + \frac{1}{\omega}[(S+R)\cos\theta + R]\right\} \\
\cos\phi &\approx \frac{\tan\theta}{\dot{\Omega}\sin i}\left\{\dot{\Omega}\cos i + \frac{1}{\omega}[(S+R)\cos\theta + R]\right\} \qquad \text{(A.22)}
\end{aligned}
$$

Equilibrium obliquity (nonlinear Cassini state relation) and azimuth

Putting Eqns. A.21 and A.22 together and setting $\omega = n$, we can solve for the new Cassini state relation and derive an expression for the azimuth. The Cassini state relation follows the pattern $c^2 = a^2 + b^2$, and the Cassini plane offsets follow the pattern, $\tan\phi = b/a$.

$$
\begin{aligned}
&\dot{\Omega}^2\sin^2 i = \dot{\Omega}^2\sin^2 i\sin^2\phi + \dot{\Omega}^2\sin^2 i\cos^2\phi \\
&\left(\dot{\Omega}\sin i\right)^2 = \left[T\sin\theta\left(1-\frac{1}{2}\cos\theta\right)\right]^2 + \tan^2\theta\left\{\dot{\Omega}\cos i + \frac{3}{2}\frac{n}{c}[(J_2+C_{22})\cos\theta + C_{22}]\right\}^2
\end{aligned}
\qquad \text{(A.23)}
$$

$$
\begin{aligned}
\frac{\dot{\Omega}\sin i\sin\phi}{\dot{\Omega}\sin i\cos\phi} &= \frac{T\sin\theta\left(\frac{n}{\omega}-\frac{1}{2}\cos\theta\right)}{\tan\theta\left\{\dot{\Omega}\cos i + \frac{1}{\omega}[(S+R)\cos\theta + R]\right\}} \\
\tan\phi &= \frac{T\cos\theta\left(\frac{n}{\omega}-\frac{1}{2}\cos\theta\right)}{\frac{3}{2}\frac{n^2}{\omega c}[(J_2+C_{22})\cos\theta + C_{22}] + \dot{\Omega}\cos i} \\
\tan\phi &= \frac{T\cos\theta\left(1-\frac{1}{2}\cos\theta\right)}{\frac{3}{2}\frac{n}{c}[(J_2+C_{22})\cos\theta + C_{22}] + \dot{\Omega}\cos i} \qquad \text{(A.24)}
\end{aligned}
$$

In the limit that dissipation is negligible, $k_2/Q = 0$ ($T = 0$), so $\tan\phi \approx \phi \approx 0$. The Cassini state relation simplifies to the standard expression (e.g., Bills & Nimmo 2011, Chen & Nimmo 2016):

$$\begin{aligned}
(\mu \sin i)^2 &\approx \left\{ \frac{3}{2}\frac{n}{c}[(J_2 + C_{22})\cos\theta + C_{22}] + \dot{\Omega}\cos i \right\}^2 \tan^2\theta \\
\dot{\Omega}\sin i\cos\theta &\approx \frac{3}{2}\frac{n}{c}[(J_2 + C_{22})\cos\theta + C_{22}]\sin\theta + \dot{\Omega}\cos i\sin\theta \\
\dot{\Omega}(\sin i\cos\theta - \cos i\sin\theta) &\approx \frac{3}{2}\frac{n}{c}[(J_2 + C_{22})\cos\theta + C_{22}]\sin\theta \\
\dot{\Omega}\sin(i-\theta) &\approx \frac{3}{2}\frac{n}{c}[(J_2 + C_{22})\cos\theta + C_{22}]\sin\theta
\end{aligned} \tag{A.25}$$

A.7 Comparing our equilibrium spin state to other works

While finding the Cassini plane offset has been attempted before, it has led to inconsistent or non-generalizable results. For the Moon, Yoder (1981) provides a numerical relationship which is not generalizable to other bodies. Fabrycky et al. (2007) and Baland et al. (2017) find different functional forms than we do, although focusing on exoplanets and Mercury respectively may have led to different assumptions. Organowski and Dumberry (2020) and similar subsequent papers (Zhang and Dumberry, 2021; MacPherson and Dumberry, 2022) use a rotational model to approximate an expression for the offset. Their simplified analytical expression is very similar to ours. Finally, Bills and Brown (2022) assume that any energy dissipation comes from the change in potential energy due to a reorientation of the triaxial figure and not from tides; their expressions differ substantially from ours.

Yoder (1981): This work provides a review of lunar laser ranging and the

detection of the Cassini plane offset. On page 115, he preesents the following equation without any derivation from which he finds that $k_2/Q = 1.0 \times 10^{-3}$ for the Moon:

$$\sin 1.5^\circ \Delta\phi = -223" \frac{k_2}{Q}$$

Problems:

- This result is ungeneralizable, and so we cannot use it for Titan.

Fabrycky et al. (2007): This paper addresses exoplanets in a Cassini state and whether it is possible for them to maintain large obliquities. It is a response to Levrard et al. (2007) that proposed the idea. They conclude that the azimuth becomes so large for the tidal dissipations needed that the planet would leave Cassini state 2 and enter state 1, lowering the obliquity. Their azimuthal phase angle due to dissipation is (their Eq. 33):

$$\phi_s \approx (\xi \cos\theta)^{-1} (\tan\theta \cot I - 1)$$

With the variables (their Eqs. 30 & 21):

$$\xi = 2k_p \Omega_p t_{FP} \frac{M}{M_p} \left(\frac{R_p}{a}\right)^5 = \frac{2}{3} Q_p \frac{\Omega_p}{n} \frac{M_p}{\mu}$$

$$Q' = Q \left[\frac{3}{4k}\right]$$

$$t_{FP} = \frac{4}{9} Q' \left(\frac{a}{R_p}\right)^5 \frac{M_i^2}{\mu M n}$$

where $\mu = M_* M_p / M$. Plugging everything in:

$$\phi_s \approx \frac{(\tan\theta \cot I - 1)}{\frac{2}{3} Q_p \frac{\Omega_p}{n} \frac{M_p}{\mu} \cos\theta}$$

$$\phi_s \approx \frac{3}{2} \frac{n}{\Omega_p} \frac{1}{Q_p} \frac{\mu}{M_p} \frac{\tan\theta \cot I - 1}{\cos\theta}$$

$$\phi_s \approx \frac{3}{2} \frac{n}{\Omega_p} \frac{1}{Q_p} \frac{\mu}{M_p} \frac{\sin\theta \cos I - cos\theta \sin I}{\cos^2\theta \sin I}$$

$$\phi_s \approx \frac{3}{2} \frac{n}{\Omega_p} \frac{1}{Q_p} \frac{\mu}{M_p} \frac{\sin(\theta - I)}{\cos^2\theta \sin I}$$

Problems:

- The expression for their azimuth contains no k_p despite containing Q_p.
- There are no terms for orbit or figure precession. The tidal torque should balance these precession terms which is what leads to a non-zero azimuth.

Baland et al. (2017): This work focuses on Mercury's Cassini state dynamics. They make use of Mercury's Cassini plane offset and acknowledge that it is affected by the tidal deformation and viscous coupling at the core-mantle boundary. They do not provide an analytical solution for the Cassini plane offset, only how to calculate its time series from their rotational model.

Organowski & Duberry (2020): This work aims to explain the 0.27 arcsecond lunar offset observed from lunar laser ranging through tidal deformation and viscous friction at the core-mantle boundary. They solve a set of differential equations and check that against a truncated analytical approximation. Equation (63) in Organowski & Duberry (2020) is an analytical expression for ϕ_p, their Cassini plane offset, in terms of k_2/Q and K/C. Here I expand out the first term in their Eq. 63,

which is ϕ_p due to tidal dissipation and simplify so that we can compare it to other formulations.

$$\phi_p = \left(\frac{1}{\delta\omega - \beta\Phi_2}\right)\left(\frac{k_2}{Q}\right)\left(\frac{R^5 n^2 \Phi_t}{3G\bar{A}}\right)$$

With the following variables:

$$\begin{aligned}
\Phi_t &= 9\mathcal{M}^2\left(\frac{n}{\Omega_0}\right)^4 \sin(I+\theta_p)\left[f_1 - \frac{f_2}{2}\frac{\Omega_0}{n}\cos(I+\theta_p)\right] \\
\Phi_2 &= \frac{3}{2}\frac{\mathcal{M}n^2}{\Omega_0^2}\frac{(\cos^2 I - \sin^2 I)}{(1-e^2)^{3/2}} \\
\bar{A} &= \frac{1}{2}(A+B) \\
\beta &= \frac{C-A}{B} \\
\delta\omega &= \eta/n \\
f_1 &= \frac{1}{(1-e^2)^6}\left(1 + \frac{15}{2}e^2 + \frac{45}{8}e^4\right) \\
f_2 &= \frac{1}{(1-e^2)^{9/2}}\left(1 + 3e^2 + \frac{3}{8}e^4\right) \\
\mathcal{M} &= \frac{M}{M_p + M}
\end{aligned}$$

The nodal precession rate is η. In the limit that $e \ll 1 \rightarrow f_1 = f_2 \approx 1$. For synchronous rotation, $\Omega_0 = n$, $\frac{\mathcal{M}n^2}{\Omega_0^2} \approx 1$ (from $M_p \gg M$). The obliquity with respect to the orbit normal is, $\theta = I + \theta_p$. We simplify to:

$$\begin{aligned}
\Phi_t &\approx 9\sin\theta\left(1 - \frac{1}{2}\cos\theta\right) \\
\Phi_2 &\approx \frac{3}{2}(\cos^2 I - \sin^2 I) \\
\phi_p &\approx 3\frac{k_2}{Q}\left(\frac{R^5 M_p}{a^3}\right)\frac{1}{\bar{A}}\left(\frac{1}{\eta/n - \frac{3}{2}\beta\cos 2I}\right)\sin\theta\left(1 - \frac{1}{2}\cos\theta\right)
\end{aligned}$$

The denominator contains terms that depend on the moments of inertia, A, B, C:

$$A = C - (J_2 + 2C_{22})MR^2$$

$$\bar{A} = C - J_2 MR^2$$

$$B = 4C_{22}MR^2 + A$$

$$B = MR^2(2C_{22} + c - J_2)$$

$$\beta = \frac{C - A}{B} = \frac{(J_2 + 2C_{22})}{c - J_2 + 2C_{22}}$$

$$\phi_p \approx 3\frac{k_2}{Q}\left(\frac{R^5 M_p}{a^3}\right)\sin\theta\left(1 - \frac{1}{2}\cos\theta\right)\frac{1}{MR^2(c - J_2)}\left[\frac{1}{\eta/n - \frac{3}{2}\frac{(J_2+2C_{22})}{c-J_2+2C_{22}}\cos 2i}\right]$$

For $c \gg J_2, C_{22}$:

$$\phi_{p|OD2020} \approx 3\frac{k_2}{Q}\left(\frac{R}{a}\right)^3\left(\frac{M_p}{M}\right)\sin\theta\left(1 - \frac{1}{2}\cos\theta\right)\left[\frac{1}{\frac{\eta}{n}c - \frac{3}{2}(J_2 + 2C_{22})\cos 2i}\right]$$

Compared to Gladman et al. (1996) where we assume small θ and $\mu = -\eta$:

$$\sin\gamma|_{G96} \approx \frac{3\left(\frac{M_p}{M}\right)\left(\frac{R}{a}\right)^3\frac{k_2}{Q}\cos\theta\sin\theta\left(1 - \frac{1}{2}\cos\theta\right)}{\frac{\eta}{n}c\cos i + \frac{3}{2}(J_2 + 2C_{22})}$$

Saying that $D = 3\frac{k_2}{Q}\left(\frac{R}{a}\right)^3\left(\frac{M_p}{M}\right)\left(1 - \frac{1}{2}\cos\theta\right)$:

$$\phi_{p|OD2020} = D\left[\frac{\sin\theta}{\frac{\eta}{n}c - \frac{3}{2}(J_2 + 2C_{22})\cos 2i}\right]$$

$$\sin\gamma|_{G96} = D\left[\frac{\sin\theta\cos\theta}{\frac{\eta}{n}c\cos i + \frac{3}{2}(J_2 + 2C_{22})}\right]$$

Differences:

- In OD2020, the i term is with precession due to the oblateness and triaxial figure (J_2, C_{22}) whereas in G96, it goes with the nodal precession frequency, η. The change in the spin axis due to precession of the orbit about the Laplace pole is:

$d\hat{s} = \eta(\hat{k} \times \hat{s}) = \eta \sin(i - \theta)$. This is why the i term belongs with the orbit precession term, η, and it's unclear to me how to justify the OD2020 version.

- For small i and θ, the only real difference is the sign of the second term in the denominator, which for $c \gg J_2, C_{22}$, does not make a real difference. This is probably why our results are so similar.

A.8 Other works that have spin equations of motion

Levrard et al. (2007): This work focuses on finding whether obliquity tides can explain the inflated nature of Hot Jupiters. They provide the equations of motion for the spin rate and obliquity and include a tidal dissipation term.

Ward (1973): This work focuses on the Martian obliquity and includes precessional equations of motion with added terms for the change in the inclination.

Peale (1974): This work is interested in the past spin evolution of Mercury and how it came to occupy the 3:2 spin-orbit resonance and Cassini state 1. Section III provides analytical equations of motion that when rearranged to find the rate of change in the obliquity and azimuth, are the same as in Gladman et al. (1996) but without the tidal torque terms and maybe with some sign errors.

Peale (2005): This work is also interested in Mercury and includes tidal and viscous CMB torques in a way that is reminiscent of Goldreich and Peale (1970) but leaving less out.

Bibliography

J. Anderson, R. Jacobson, T. McElrath, W. Moore, G. Schubert, and P. Thomas. Shape, mean radius, gravity field, and interior structure of callisto. *Icarus*, 153(1):157–161, 2001a.

J. D. Anderson, R. A. Jacobson, E. L. Lau, W. B. Moore, and G. Schubert. Io's gravity field and interior structure. *Journal of Geophysical Research: Planets*, 106(E12): 32963–32969, 2001b.

E. Asphaug and A. Reufer. Late origin of the saturn system. *Icarus*, 223(1):544–565, 2013.

R.-M. Baland, T. Van Hoolst, M. Yseboodt, and Ö. Karatekin. Titan's obliquity as evidence of a subsurface ocean? *Astronomy & Astrophysics*, 530:A141, 2011.

R.-M. Baland, M. Yseboodt, and T. Van Hoolst. Obliquity of the galilean satellites: The influence of a global internal liquid layer. *Icarus*, 220(2):435–448, 2012.

R.-M. Baland, G. Tobie, A. Lefèvre, and T. Van Hoolst. Titan's internal structure inferred from its gravity field, shape, and rotation state. *Icarus*, 237:29–41, 2014.

R.-M. Baland, M. Yseboodt, A. Rivoldini, and T. Van Hoolst. Obliquity of mercury: Influence of the precession of the pericenter and of tides. *Icarus*, 291:136–159, 2017.

R.-M. Baland, A. Coyette, and T. Van Hoolst. Coupling between the spin precession and polar motion of a synchronously rotating satellite: application to titan. *Celestial Mechanics and Dynamical Astronomy*, 131:1–50, 2019.

J. W. Barnes, E. P. Turtle, M. G. Trainer, R. D. Lorenz, S. M. MacKenzie, W. B. Brinckerhoff, M. L. Cable, C. M. Ernst, C. Freissinet, K. P. Hand, et al. Science goals and objectives for the dragonfly titan rotorcraft relocatable lander. *The Planetary Science Journal*, 2(4):130, 2021.

C. Béghin, O. Randriamboarison, M. Hamelin, E. Karkoschka, C. Sotin, R. C. Whitten, J.-J. Berthelier, R. Grard, and F. Simões. Analytic theory of titan's schumann resonance: Constraints on ionospheric conductivity and buried water ocean. *Icarus*, 218(2):1028–1042, 2012.

M. Beuthe. Crustal control of dissipative ocean tides in Enceladus and other icy moons. *Icarus*, 280:278–299, Dec. 2016.

C. Bierson and F. Nimmo. A test for io's magma ocean: Modeling tidal dissipation with a partially molten mantle. *Journal of Geophysical Research: Planets*, 121(11): 2211–2224, 2016.

B. Bills and F. Nimmo. How jupiter helped titan retain a finite orbital eccentricity. *AGUFM*, 2005:P33C–0263, 2005.

B. G. Bills. Free and forced obliquities of the galilean satellites of jupiter. *Icarus*, 175 (1):233–247, 2005.

B. G. Bills and A. J. Brown. Influence of energy dissipation on spin pole precession trajectories for synchronous rotators. *The Planetary Science Journal*, 3(1):18, 2022.

B. G. Bills and F. Nimmo. Forced obliquity and moments of inertia of titan. *Icarus*, 196(1):293–297, 2008.

B. G. Bills and F. Nimmo. Rotational dynamics and internal structure of titan. *Icarus*, 214(1):351–355, 2011.

B. G. Bills and R. D. Ray. Lunar orbital evolution: A synthesis of recent results. *Geophysical Research Letters*, 26(19):3045–3048, 1999.

M. T. Bland, A. P. Showman, and G. Tobie. The orbital–thermal evolution and global expansion of ganymede. *Icarus*, 200(1):207–221, 2009.

M. T. Bland, K. N. Singer, W. B. McKinnon, and P. M. Schenk. Viscous relaxation of ganymede's impact craters: Constraints on heat flux. *Icarus*, 296:275–288, 2017.

L. E. Borg, J. N. Connelly, M. Boyet, and R. W. Carlson. Chronological evidence that the moon is either young or did not have a global magma ocean. *Nature*, 477(7362): 70–72, 2011.

L. E. Borg, A. M. Gaffney, and C. K. Shearer. A review of lunar chronology revealing a preponderance of 4.34–4.37 ga ages. *Meteoritics & Planetary Science*, 50(4):715–732, 2015.

J. Burns, J. Cuzzi, R. Durisen, and P. Hamill. On the'thickness' of saturn's rings caused by satellite and solar perturbations and by planetary precession. *Astronomical Journal, vol. 84, Nov. 1979, p. 1783-1801.*, 84:1783–1801, 1979.

R. M. Canup. Origin of saturn's rings and inner moons by mass removal from a lost titan-sized satellite. *Nature*, 468(7326):943–946, 2010.

R. M. Canup and E. Asphaug. Origin of the moon in a giant impact near the end of the earth's formation. *Nature*, 412(6848):708–712, 2001.

P. Cappuccio, M. Di Benedetto, and L. Iess. Analysis of juice 3gm gravity experiment at callisto and ganymede. In *AGU Fall Meeting Abstracts*, volume 2020, pages P048–0006, 2020.

P. Cappuccio, M. Di Benedetto, D. Durante, and L. Iess. Callisto and europa gravity measurements from juice 3gm experiment simulation. *The Planetary Science Journal*, 3(8):199, 2022.

S. Champenois and A. Vienne. Chaos and secondary resonances in the mimas–tethys system. *Celestial Mechanics and Dynamical Astronomy*, 74(2):111–146, 1999.

E. Chen, F. Nimmo, and G. Glatzmaier. Tidal heating in icy satellite oceans. *Icarus*, 229:11–30, 2014.

E. M. Chen and F. Nimmo. Tidal dissipation in the lunar magma ocean and its effect on the early evolution of the earth–moon system. *Icarus*, 275:132–142, 2016.

C. F. Chyba, D. Jankowski, and P. Nicholson. Tidal evolution in the neptune-triton system. *Astronomy and Astrophysics*, 219:L23–L26, 1989.

G. Colombo. Cassini's second and third laws. *The Astronomical Journal*, 71:891, 1966.

A. C. Correia. The core–mantle friction effect on the secular spin evolution of terrestrial planets. *Earth and Planetary Science Letters*, 252(3-4):398–412, 2006.

A. C. Correia and J. Laskar. The four final rotation states of venus. *Nature*, 411(6839): 767–770, 2001.

A. Coyette, R.-M. Baland, and T. Van Hoolst. Variations in rotation rate and polar motion of a non-hydrostatic titan. *Icarus*, 307:83–105, 2018.

M. Ćuk, L. Dones, and D. Nesvornỳ. Dynamical evidence for a late formation of saturn's moons. *The Astrophysical Journal*, 820(2):97, 2016a.

M. Ćuk, D. P. Hamilton, S. J. Lock, and S. T. Stewart. Tidal evolution of the moon from a high-obliquity, high-angular-momentum earth. *Nature*, 539(7629):402–406, 2016b.

M. Ćuk, S. J. Lock, S. T. Stewart, and D. P. Hamilton. Tidal evolution of the earth–moon system with a high initial obliquity. *The Planetary Science Journal*, 2(4):147, 2021.

H. Daher, B. K. Arbic, J. G. Williams, J. K. Ansong, D. H. Boggs, M. Müller, M. Schindelegger, J. Austermann, B. D. Cornuelle, E. B. Crawford, et al. Long-term earth-moon evolution with high-level orbit and ocean tide models. *Journal of Geophysical Research: Planets*, 126(12):e2021JE006875, 2021.

R. Dbouk and J. Wisdom. The origin of jupiter's obliquity. *The Planetary Science Journal*, 4(10):188, 2023.

S. F. Dermott, R. Malhotra, and C. D. Murray. Dynamics of the uranian and saturnian satelite systems: A chaotic route to melting miranda? *Icarus*, 76(2):295–334, 1988.

J. O. Dickey, P. Bender, J. Faller, X. Newhall, R. Ricklefs, J. Ries, P. Shelus, C. Veillet, A. Whipple, J. Wiant, et al. Lunar laser ranging: A continuing legacy of the apollo program. *Science*, 265(5171):482–490, 1994.

D. Durante, D. Hemingway, P. Racioppa, L. Iess, and D. Stevenson. Titan's gravity field and interior structure after cassini. *Icarus*, 326:123–132, 2019.

L. T. Elkins-Tanton, S. Burgess, and Q.-Z. Yin. The lunar magma ocean: Reconciling the solidification process with lunar petrology and geochronology. *Earth and Planetary Science Letters*, 304(3-4):326–336, 2011.

D. C. Fabrycky, E. T. Johnson, and J. Goodman. Cassini states with dissipation: Why obliquity tides cannot inflate hot jupiters. *The Astrophysical Journal*, 665(1):754, 2007.

R. Fan, L. Zhao, Y. Lu, H. Nie, and H. Wei. Impacts of currents and waves on bottom drag coefficient in the east china shelf seas. *Journal of Geophysical Research: Oceans*, 124(11):7344–7354, 2019.

J. Fuller, J. Luan, and E. Quataert. Resonance locking as the source of rapid tidal

migration in the jupiter and saturn moon systems. *Monthly Notices of the Royal Astronomical Society*, 458(4):3867–3879, 2016.

I. Garrick-Bethell, J. Wisdom, and M. T. Zuber. Evidence for a past high-eccentricity lunar orbit. *Science*, 313(5787):652–655, 2006.

I. Garrick-Bethell, F. Nimmo, and M. A. Wieczorek. Structure and formation of the lunar farside highlands. *science*, 330(6006):949–951, 2010.

I. Garrick-Bethell, V. Perera, F. Nimmo, and M. T. Zuber. The tidal–rotational shape of the moon and evidence for polar wander. *Nature*, 512(7513):181–184, 2014.

B. Gladman, D. D. Quinn, P. Nicholson, and R. Rand. Synchronous locking of tidally evolving satellites. *Icarus*, 122(1):166–192, 1996.

P. Goldreich. History of the lunar orbit. *Reviews of Geophysics*, 4(4):411–439, 1966.

P. Goldreich. Precession of the moon's core. *Journal of Geophysical Research*, 72(12): 3135–3137, 1967.

P. Goldreich and T. Gold. On the eccentricity of satellite orbits in the solar system. *Monthly Notices of the Royal Astronomical Society*, 126(3):257–268, 1963.

P. Goldreich and S. Peale. The obliquity of venus. *Astronomical Journal, Vol. 75, p. 273 (1970)*, 75:273, 1970.

P. Goldreich and S. Soter. Q in the solar system. *Icarus*, 5(1-6):375–389, 1966.

L. Gomez Casajus, A. Ermakov, M. Zannoni, J. Keane, D. Stevenson, D. Buccino, D. Durante, M. Parisi, R. Park, P. Tortora, et al. Gravity field of ganymede after the juno extended mission. *Geophysical Research Letters*, 49(24):e2022GL099475, 2022.

S. Goossens, B. van Noort, A. Mateo Aguaron, E. Mazarico, and W. van der Wal. Enceladus gravity and titan gravity and tides from cassini tracking data. *LPI Contributions*, 2806:1528, 2023.

R. Greeley, J. Klemaszewski, R. Wagner, et al. Galileo views of the geology of callisto. *Planetary and Space Science*, 48(9):829–853, 2000.

A. W. Harris and W. R. Ward. Dynamical constraints on the formation and evolution of planetary bodies. *In: Annual review of earth and planetary sciences. Volume 10.(A82-35776 17-88) Palo Alto, CA, Annual Reviews, Inc., 1982, p. 61-108.*, 10: 61–108, 1982.

O. Hartkorn and J. Saur. Induction signals from callisto's ionosphere and their implications on a possible subsurface ocean. *Journal of Geophysical Research: Space Physics*, 122(11):11–677, 2017.

H. C. Hay and I. Matsuyama. Numerically modelling tidal dissipation with bottom drag in the oceans of titan and enceladus. *Icarus*, 281:342–356, 2017.

H. C. F. C. Hay and I. Matsuyama. Nonlinear tidal dissipation in the subsurface oceans of Enceladus and other icy satellites. *Icarus*, 319:68–85, Feb. 2019.

D. Hemingway, F. Nimmo, H. Zebker, and L. Iess. A rigid and weathered ice shell on titan. *Nature*, 500(7464):550–552, 2013.

H. Hussmann, F. Sohl, and T. Spohn. Subsurface oceans and deep interiors of medium-sized outer planet satellites and large trans-neptunian objects. *Icarus*, 185(1):258–273, 2006.

B. Idini and F. Nimmo. Resonant stratification in titan's global ocean. *The Planetary Science Journal*, 5(1):15, 2024.

L. Iess, N. J. Rappaport, R. A. Jacobson, P. Racioppa, D. J. Stevenson, P. Tortora, J. W. Armstrong, and S. W. Asmar. Gravity field, shape, and moment of inertia of titan. *science*, 327(5971):1367–1369, 2010.

L. Iess, R. A. Jacobson, M. Ducci, D. J. Stevenson, J. I. Lunine, J. W. Armstrong, S. W. Asmar, P. Racioppa, N. J. Rappaport, and P. Tortora. The tides of titan. *Science*, 337(6093):457–459, 2012.

R. Jacobson and V. Lainey. Martian satellite orbits and ephemerides. *Planetary and space science*, 102:35–44, 2014.

R. A. Jacobson. The orbits of the main saturnian satellites, the saturnian system gravity field, and the orientation of saturn's pole. *The Astronomical Journal*, 164(5): 199, 2022.

H. Jeffreys. Certain hypotheses as to the internal structure of the earth and moon. *Memoirs of the Royal Astronomical Society*, 60:187, 1915.

H. Jeffreys. Lxxxiv. the flow of water in an inclined channel of rectangular section. *The London, Edinburgh, and Dublin Philosophical Magazine and Journal of Science*, 49 (293):793–807, 1925.

B. Journaux, K. Kalousová, C. Sotin, G. Tobie, S. Vance, J. Saur, O. Bollengier, L. Noack, T. Rückriemen-Bez, T. Van Hoolst, et al. Large ocean worlds with high-pressure ices. *Space Science Reviews*, 216:1–36, 2020.

W. M. Kaula. Tidal dissipation by solid friction and the resulting orbital evolution. *Reviews of geophysics*, 2(4):661–685, 1964.

J. T. Keane and I. Matsuyama. Evidence for lunar true polar wander and a past low-eccentricity, synchronous lunar orbit. *Geophysical Research Letters*, 41(19):6610–6619, 2014.

R. L. Kirk and D. J. Stevenson. Thermal evolution of a differentiated ganymede and implications for surface features. *Icarus*, 69(1):91–134, 1987.

A. S. Konopliv, R. S. Park, D.-N. Yuan, S. W. Asmar, M. M. Watkins, J. G. Williams, E. Fahnestock, G. Kruizinga, M. Paik, D. Strekalov, et al. The jpl lunar gravity field to spherical harmonic degree 660 from the grail primary mission. *Journal of Geophysical Research: Planets*, 118(7):1415–1434, 2013.

O. Kuskov and V. Kronrod. Internal structure of europa and callisto. *Icarus*, 177(2): 550–569, 2005.

V. Lainey, J.-E. Arlot, Ö. Karatekin, and T. Van Hoolst. Strong tidal dissipation in io and jupiter from astrometric observations. *Nature*, 459(7249):957, 2009.

V. Lainey, R. A. Jacobson, R. Tajeddine, N. J. Cooper, C. Murray, V. Robert, G. Tobie, T. Guillot, S. Mathis, F. Remus, et al. New constraints on saturn's interior from cassini astrometric data. *Icarus*, 281:286–296, 2017.

V. Lainey, L. G. Casajus, J. Fuller, M. Zannoni, P. Tortora, N. Cooper, C. Murray, D. Modenini, R. S. Park, V. Robert, et al. Resonance locking in giant planets indicated by the rapid orbital expansion of titan. *Nature Astronomy*, pages 1–6, 2020.

K. Lambeck. Effects of tidal dissipation in the oceans on the moon's orbit and the earth's rotation. *Journal of Geophysical Research*, 80(20):2917–2925, 1975.

K. Lambeck and S. Pullan. The lunar fossil bulge hypothesis revisited. *Physics of the Earth and Planetary Interiors*, 22(1):29–35, 1980.

G. Lari, M. Saillenfest, and M. Fenucci. Long-term evolution of the galilean satellites: the capture of callisto into resonance. *arXiv preprint arXiv:2001.01106*, 2020.

A. Love. A treaties on the mathematical theory of elasticity. *A treaties on the Mathematical Theory of Elasticity*, 643, 1927.

G. J. MacDonald. Tidal friction. *Reviews of Geophysics*, 2(3):467–541, 1964.

I. MacPherson and M. Dumberry. Deviation of mercury's spin axis from an exact cassini state induced by dissipation. *Journal of Geophysical Research: Planets*, 127 (4):e2022JE007184, 2022.

J.-L. Margot, S. Padovan, D. Campbell, S. Peale, and F. Ghigo. Measurements of the spin states of europa and ganymede. In *American Astronomical Society, DPS Meeting*, volume 45, 2013.

I. Matsuyama. Fossil figure contribution to the lunar figure. *Icarus*, 222(1):411–414, 2013.

I. Matsuyama. Tidal dissipation in the oceans of icy satellites. *Icarus*, 242:11–18, Nov. 2014.

I. Matsuyama, M. Beuthe, H. C. F. C. Hay, F. Nimmo, and S. Kamata. Ocean tidal heating in icy satellites with solid shells. *Icarus*, 312:208–230, Sept. 2018.

I. Matsuyama, A. Trinh, and J. T. Keane. The lunar fossil figure in a cassini state. *The Planetary Science Journal*, 2(6):232, 2021.

M. Maurice, N. Tosi, S. Schwinger, D. Breuer, and T. Kleine. A long-lived magma ocean on a young moon. *Science advances*, 6(28):eaba8949, 2020.

E. Mazarico, D. Buccino, J. Castillo-Rogez, A. J. Dombard, A. Genova, H. Hussmann, W. S. Kiefer, J. I. Lunine, W. B. McKinnon, F. Nimmo, et al. The europa clipper gravity and radio science investigation. *Space Science Reviews*, 219(4):30, 2023.

W. B. McKinnon. On convection in ice i shells of outer solar system bodies, with detailed application to callisto. *Icarus*, 183(2):435–450, 2006.

R. Meriggiola, L. Iess, B. W. Stiles, J. I. Lunine, and G. Mitri. The rotational dynamics of titan from cassini radar images. *Icarus*, 275:183–192, 2016.

J. Meyer and J. Wisdom. Precession of the lunar core. *Icarus*, 211(1):921–924, 2011.

J. Meyer, L. Elkins-Tanton, and J. Wisdom. Coupled thermal–orbital evolution of the early moon. *Icarus*, 208(1):1–10, 2010.

F. Mignard. The evolution of the lunar orbit revisited. i. *The Moon and the planets*, 20 (3):301–315, 1979.

F. Mignard. The evolution of the lunar orbit revisited, ii. *The Moon and the planets*, 23(2):185–201, 1980.

F. Mignard. The lunar orbit revisited, iii. *The Moon and the Planets*, 24(2):189–207, 1981.

G. Mitri and A. P. Showman. Thermal convection in ice-i shells of titan and enceladus. *Icarus*, 193(2):387–396, 2008.

W. B. Moore and G. Schubert. The tidal response of ganymede and callisto with and without liquid water oceans. *Icarus*, 166(1):223–226, 2003.

W. H. Munk and G. J. MacDonald. The rotation of the earth; a geophysical discussion. *Cambridge [Eng.] University Press*, 1960.

C. D. Murray and S. F. Dermott. *Solar system dynamics*. Cambridge university press, 1999.

F. Nimmo and B. Bills. Shell thickness variations and the long-wavelength topography of titan. *Icarus*, 208(2):896–904, 2010.

F. Nimmo and R. Pappalardo. Ocean worlds in the outer solar system. *Journal of Geophysical Research: Planets*, 121(8):1378–1399, 2016.

F. Nimmo, A. C. Barr, M. Behounková, and W. B. McKinnon. The thermal and orbital evolution of enceladus: observational constraints and models. *Enceladus and the Icy Moons of Saturn*, pages 79–94, 2018.

B. Noyelles. Expression of cassini's third law for callisto, and theory of its rotation. *Icarus*, 202(1):225–239, 2009.

G. W. Ojakangas and D. J. Stevenson. Thermal state of an ice shell on europa. *Icarus*, 81(2):220–241, 1989.

O. Organowski and M. Dumberry. Viscoelastic relaxation within the moon and the phase lead of its cassini state. *Journal of Geophysical Research: Planets*, 125(7): e2020JE006386, 2020.

K. Pahlevan and A. Morbidelli. Collisionless encounters and the origin of the lunar inclination. *Nature*, 527(7579):492–494, 2015.

S. Peale. Orbital resonances, unusual configurations and exotic rotation states among planetary satellites. In *Satellites*. 1986.

S. Peale and P. Cassen. Contribution of tidal dissipation to lunar thermal history. *Icarus*, 36(2):245–269, 1978.

S. Peale, P. Cassen, and R. Reynolds. Tidal dissipation, orbital evolution, and the nature of saturn's inner satellites. *Icarus*, 43(1):65–72, 1980.

S. J. Peale. Generalized cassini's laws. *The Astronomical Journal*, 74:483, 1969.

S. J. Peale. Possible histories of the obliquity of mercury. *Astronomical Journal, Vol. 79, p. 722 (1974)*, 79:722, 1974.

S. J. Peale, P. Cassen, and R. T. Reynolds. Melting of io by tidal dissipation. *Science*, 203(4383):892–894, 1979.

C. Qin, S. Zhong, and R. Phillips. Formation of the lunar fossil bulges and its implication for the early earth and moon. *Geophysical Research Letters*, 45(3):1286–1296, 2018.

R. T. Reynolds and P. M. Cassen. On the internal structure of the major satellites of the outer planets. *Geophysical Research Letters*, 6(2):121–124, 1979.

M. Rochester. The secular decrease of obliquity due to dissipative core—mantle coupling. *Geophysical Journal International*, 46(1):109–126, 1976.

M. Ross and G. Schubert. Tidal dissipation in a viscoelastic planet. *Journal of Geophysical Research: Solid Earth*, 91(B4):447–452, 1986.

M. Rovira-Navarro, T. Gerkema, L. R. Maas, W. van der Wal, R. van Ostayen, and B. Vermeersen. Tides in subsurface oceans with meridional varying thickness. *Icarus*, 343:113711, 2020.

R. Sabadini, B. Vermeersen, and G. Cambiotti. *Global Dynamics of the Earth: Applications of Viscoelastic Relaxation Theory to Solid-Earth and Planetary Geophysics*. Springer, 2016.

C. Sagan and S. F. Dermott. The tide in the seas of titan. *Nature*, 300(5894):731, 1982.

P. M. Schenk. Thickness constraints on the icy shells of the galilean satellites from a comparison of crater shapes. *Nature*, 417(6887):419–421, 2002.

W. D. Sears. Tidal dissipation in oceans on titan. *Icarus*, 113(1):39–56, 1995.

A. P. Showman and R. Malhotra. Tidal evolution into the laplace resonance and the resurfacing of ganymede. *Icarus*, 127(1):93–111, 1997.

M. A. Siegler, B. G. Bills, and D. A. Paige. Effects of orbital evolution on lunar ice stability. *Journal of Geophysical Research: Planets*, 116(E3), 2011.

K. N. Singer, M. T. Bland, P. M. Schenk, and W. B. McKinnon. Relaxed impact craters on ganymede: Regional variation and high heat flows. *Icarus*, 306:214–224, 2018.

G. A. Snyder, L. A. Taylor, and C. R. Neal. A chemical model for generating the sources of mare basalts: Combined equilibrium and fractional crystallization of the lunar magmasphere. *Geochimica et Cosmochimica Acta*, 56(10):3809–3823, 1992.

F. Sohl, W. D. Sears, and R. D. Lorenz. Tidal dissipation on titan. *Icarus*, 115(2): 278–294, 1995.

A. Stark, J. Oberst, F. Preusker, S. J. Peale, J.-L. Margot, R. J. Phillips, G. A. Neumann, D. E. Smith, M. T. Zuber, and S. C. Solomon. First messenger orbital observations of mercury's librations. *Geophysical Research Letters*, 42(19):7881–7889, 2015.

B. W. Stiles, R. L. Kirk, R. D. Lorenz, S. Hensley, E. Lee, S. J. Ostro, M. D. Allison, P. S. Callahan, Y. Gim, L. Iess, et al. Determining titan's spin state from cassini radar images. *The Astronomical Journal*, 135(5):1669, 2008.

L. F. Teodoro, J. A. Kegerreis, P. R. Estrada, M. Ćuk, V. R. Eke, J. N. Cuzzi, R. J. Massey, and T. D. Sandnes. A recent impact origin of saturn's rings and mid-sized moons. *The Astrophysical Journal*, 955(2):137, 2023.

Z. Tian, J. Wisdom, and L. Elkins-Tanton. Coupled orbital-thermal evolution of the early earth-moon system with a fast-spinning earth. *Icarus*, 281:90–102, 2017.

G. Tobie, A. Mocquet, and C. Sotin. Tidal dissipation within large icy satellites: Applications to Europa and Titan. *Icarus*, 177:534 – 549, 09 2005a. doi: 10.1016/j.icarus.2005.04.006.

G. Tobie, A. Mocquet, and C. Sotin. Tidal dissipation within large icy satellites: Applications to europa and titan. *Icarus*, 177(2):534–549, 2005b.

G. Tobie, J. Lunine, and C. Sotin. Episodic outgassing as the origin of atmospheric methane on titan. *Nature*, 440(7080):61–64, 2006.

T. Tokano, T. Van Hoolst, and Ö. Karatekin. Polar motion of titan forced by the atmosphere. *Journal of Geophysical Research: Planets*, 116(E5), 2011.

A. Toomre. On the coupling of the earth's core and mantle during the 26,000-year precession. In *The Earth-Moon System: Proceedings of an international conference,*

January 20–21, 1964, sponsored by the Institute for Space Studies of the Goddard Space Flight Center, NASA, pages 33–45. Springer, 1966.

P. Tortora, M. Zannoni, F. Nimmo, E. Mazarico, L. Iess, C. Sotin, A. Hayes, and M. Malaska. Titan gravity investigation with the oceanus mission. In *EGU General Assembly Conference Abstracts*, page 17876, 2017.

J. Touma and J. Wisdom. Evolution of the earth-moon system. *The Astronomical Journal*, 108:1943–1961, 1994.

J. Touma and J. Wisdom. Resonances in the early evolution of the earth-moon system. *The Astronomical Journal*, 115(4):1653, 1998.

S. Tremaine, J. Touma, and F. Namouni. Satellite dynamics on the laplace surface. *The astronomical journal*, 137(3):3706, 2009.

D. Turcotte and G. Schubert. Application of continuum physics to geological problems. *NY: Wiley*, 1982.

R. Tyler. Tidal dynamical considerations constrain the state of an ocean on enceladus. *Icarus*, 211(1):770–779, 2011.

R. H. Tyler. Strong ocean tidal flow and heating on moons of the outer planets. *Nature*, 456(7223):770–772, 2008.

R. H. Tyler. Ocean tides heat enceladus. *Geophysical Research Letters*, 36(15), 2009.

R. H. Tyler. On the tidal history and future of the earth–moon orbital system. *The Planetary Science Journal*, 2(2):70, 2021.

V. Viswanathan, N. Rambaux, A. Fienga, J. Laskar, and M. Gastineau. Observational constraint on the radius and oblateness of the lunar core-mantle boundary. *Geophysical Research Letters*, 46(13):7295–7303, 2019.

W. R. Ward. Past orientation of the lunar spin axis. *Science*, 189(4200):377–379, 1975a.

W. R. Ward. Tidal friction and generalized cassini's laws in the solar system. *Astronomical Journal, vol. 80, Jan. 1975, p. 64-70.*, 80:64–70, 1975b.

W. R. Ward and R. M. Canup. Origin of the moon's orbital inclination from resonant disk interactions. *Nature*, 403(6771):741–743, 2000.

W. R. Ward and D. P. Hamilton. Tilting saturn. i. analytic model. *The Astronomical Journal*, 128(5):2501, 2004.

P. H. Warren. The bulk-moon mgo/feo ratio: A highlands perspective. In *Origin of the Moon*, page 279, 1986.

J. G. Williams and D. H. Boggs. Tides on the moon: Theory and determination of dissipation. *Journal of Geophysical Research: Planets*, 120(4):689–724, 2015.

J. G. Williams, D. H. Boggs, C. F. Yoder, J. T. Ratcliff, and J. O. Dickey. Lunar rotational dissipation in solid body and molten core. *Journal of Geophysical Research: Planets*, 106(E11):27933–27968, 2001.

J. G. Williams, A. S. Konopliv, D. H. Boggs, R. S. Park, D.-N. Yuan, F. G. Lemoine, S. Goossens, E. Mazarico, F. Nimmo, R. C. Weber, et al. Lunar interior properties from the grail mission. *Journal of Geophysical Research: Planets*, 119(7):1546–1578, 2014.

J. Wisdom. Spin-orbit secondary resonance dynamics of enceladus. *The Astronomical Journal*, 128(1):484, 2004.

J. Wisdom. Tidal dissipation at arbitrary eccentricity and obliquity. *Icarus*, 193(2): 637–640, 2008.

J. Wisdom, R. Dbouk, B. Militzer, W. B. Hubbard, F. Nimmo, B. G. Downey, and R. G. French. Loss of a satellite could explain saturn's obliquity and young rings. *Science*, 377(6612):1285–1289, 2022.

C. F. Yoder. The free librations of a dissipative moon. *Philosophical Transactions of the Royal Society of London. Series A, Mathematical and Physical Sciences*, 303(1477): 327–338, 1981.

M. Yseboodt and J.-L. Margot. Evolution of mercury's obliquity. *Icarus*, 181(2):327–337, 2006.

K. J. Zahnle, R. Lupu, A. Dobrovolskis, and N. H. Sleep. The tethered moon. *Earth and Planetary Science Letters*, 427:74–82, 2015.

H. A. Zebker, B. Stiles, S. Hensley, R. Lorenz, R. L. Kirk, and J. Lunine. Size and shape of saturn's moon titan. *Science*, 324(5929):921–923, 2009.

J. Zhang and M. Dumberry. Viscous dissipation in the fluid core of the moon. *Journal of Geophysical Research: Planets*, 126(11):e2021JE006966, 2021.

C. Zimmer, K. K. Khurana, and M. G. Kivelson. Subsurface oceans on europa and callisto: Constraints from galileo magnetometer observations. *Icarus*, 147(2):329–347, 2000.